ON THE INITIATION AND PROPAGATION OF FATIGUE CRACKS IN WC-Co

Ghita Erling

A dissertation submitted to the Faculty of Engineering, University of the Witwatersrand, in fulfilment of the requirements for the degree of Master of Science in Engineering.

Johannesburg, 1998

Errata

	"Vibrophore" **should read** "Vibraphore" **throughout**
Page 49	**Insert at end :** "3.4.4 Fractography The fracture surfaces of the specimen broken in four point bend testing were then examined in a Noran LEO 960A Digital Scanning Electron Microscope to compare the fracture surfaces arising from the different failure modes."
Page 57	**Add before table 3.4**: " The materials properties used in the FEM were those of WC-Co grade T6. The reason for this is that the FEM has been based on the T6 microstructure."
Page 83	**Insert :** "The size of the WC grains on the T6 and G6 fast fracture surfaces, in *Figures 20* and *21* respectively, appear to be very similar. This is consistent with the fatigue growth rate results presented in *Figure 4.18*."
Page 86	**Replace line 4 :** "...without being subjected to fatigue loading..." **with :** "...without being subjected to tensile fatigue loading..."
Page 99	**Replace paragraph 1, 1st line :** "...larger of the principal stresses..." **with :** "...higher of the principal stresses..."
	Replace paragraph 2, 1st line : "...smaller of the principal stresses..." **with:** "...lower of the principal stresses..."
	Replace paragraph 2, 2nd line : "vary from below -1000 and 400 *MPa*..." **with :** "vary from -10 000 and 400 *MPa*..."
Page 100	**Insert at end :** "This in effect means that while the introduction of the notch relieves stresses at the free surface, the relaxation of the surface material introduces new stresses away from the notch. This occurs as the bulk material is constrained and cannot relax with the material at the free surface, thus stresses are introduced between the material that has relaxed and the material that cannot relax."
Page 105	**Insert at the end :** "*Figure 4.50* shows that tensile stresses are generated in directions 1 and 2. This means that microcracks can form in all directions. These microcracks joining together can thus result in 'chunks' of material being dislodged, as was discussed earlier in the chapter".
Page 108	**Add at the end :** . "The deformation generally seems to occur in the cobalt regions that are subject to the highest stresses, shown as the stress range between 2.14 *GPa* and 5.71 *GPa* in *Figures 4.51* and *4.52*. No deformation is shown to develop at the high stresses set up in carbide grains as the carbide phase in this model was not given plastic properties."

I declare that this dissertation is my own, unaided work. It is being submitted for the Degree of Master of Science in Engineering in the University of the Witwatersrand, Johannesburg. It has not been submitted before for any other degree in any other university.

24 day of November, 1998

Abstract

This research examines fatigue in WC-Co, both under compressive and tensile loading conditions. A new macro-mechanism for compression fatigue crack propagation is put forward, which contradicts existing data on compression fatigue cracks as being self-limiting. Evidence of this macro-mechanism is presented in the form of final crack length versus number of cycles data, and micrographs of the compression fatigue cracks. A finite element study of the stress distribution in the WC-Co microstructure during compression fatigue loading has been developed. This model verifies possible methods of compression fatigue crack initiation. Examination of tensile fatigue and fast fracture surfaces is used to show that fatigue is a separate mechanism to fast fracture in WC-Co. Characteristic features of the fatigue fracture surface are presented. A possible fatigue crack propagation mechanism is also presented. Finally, fatigue crack growth rate data in the form of the Paris equation is presented for WC-Co grades T6 and G6.

Acknowledgements

Professor S Luyckx, for her guidance, help and supervision of this project
Dr B Olmstead, for his interest, guidance and supervision of this project

Professor M N James for inspiring this project

Boart Longyear Research Laboratory for the specimens and use of facilities

CSIR, Mattek for sponsoring the finite element model and use of facilities

Zaid Isaacs, for his superb photography

The following for suggestions, technical assistance and/or encouragement:
    Dr L Cornish
    Mr M Franze
    Dr A Human
    Dr S Ng'ang'a
    Mr I Northrop
    Mr I Schwartz

Index

Table of Figures

List of Tables

Nomenclature

P	applied load (N)
P_{max}	maximum applied load
P_{min}	minimum applied load
ΔP	change in applied load during cyclic loading $\Delta P = P_{max} - P_{min}$
P_{ave}	average applied load $P_{ave} = \frac{P_{max} + P_{min}}{2}$
P_{amp}	load amplitude $P_{amp} = P_{max} - P_{ave} = P_{ave} - P_{min}$
σ	applied stress (Pa)
$\Delta\sigma$	change in applied stress during cyclic loading $\Delta\sigma = \sigma_{max} - \sigma_{min}$
σ_{max}	maximum applied stress arising from P_{max}
σ_{min}	minimum applied stress arising from P_{min}
σ_{ave}	mean applied stress arising from P_{ave}
σ_{amp}	stress amplitude arising from P_{amp}
σ_{op}	crack opening stress
k	stress concentration factor
K	stress intensity factor ($MPa\sqrt{m}$)
K_{max}	stress intensity factor arising from σ_{max}, the maximum applied stress
K_{min}	stress intensity factor arising from σ_{min}, the minimum applied stress
K_{ave}	stress intensity factor arising from σ_{ave}, the mean applied stress
K_{amp}	stress intensity factor arising from σ_{amp}, the stress amplitude
ΔK	change in K during cyclic loading $\Delta K = K_{max} - K_{min}$
ΔK_0	threshold stress intensity factor
ΔK_{eff}	effective stress intensity range
K_C	critical stress intensities in plane stress
K_{IC}	fracture toughness
a	crack length
n	of cycles

$\frac{da}{dn}$	crack growth rate
R	stress ratio $R = \frac{\sigma_{\min}}{\sigma_{\max}}$

Abreviations used in the *ABAQUS* Contour Maps

peeq	equivalent plastic strain
sp1	smaller of the principal stresses in the plane of the contour map
sp2	larger of the principal stresses in the plane of the contour map
s11	stresses in the 1,1 direction (as indicated by the direction axes)
s22	stresses in the 2,2 direction (as indicated by the direction axes) all the stresses are presented in *Pa*
vvf	void volume fraction, the value of which varies between 1 (fully voided) and 0 (fully dense)

1. Introduction

Although considerable research into the fast fracture processes in WC-Co has been conducted in order to understand the fracture toughness of the material, very little work has been conducted into understanding stable crack propagation. This may be partly due to the difficulties associated with fatigue testing of brittle materials - mainly with the difficulty of producing a stable crack in a brittle material from which to initiate a fatigue crack. However, in the last decade, a method of compression fatigue has been developed as a means of initiating stable cracks in brittle materials and it has been applied to WC-Co.

This investigation aimed at acquiring a better understanding of stable crack growth under both compressive and tensile loading conditions. This involved firstly, investigating the initiation and propagation of stable cracks in WC-Co produced by the compression fatigue method and secondly, investigating the propagation of stable cracks in WC-Co subjected to tensile loading conditions.

Following the compression fatigue method, the cracks were produced from a notch, by submitting the sample to compressive loading cycles. The propagation of the cracks was monitored by means of replicas and the propagation mechanisms were deduced from scanning electron micrographs of crack outcrops and fracture surfaces.

The initiation of the compression fatigue cracks was modelled by finite element analysis. This technique was used to determine the stress distribution at the root of the notch and crack initiation was assumed to occur at the sites of maximum tensile stress.

Finally, the cracks produced by the fatigue compression method were grown in the four-point bending loading configuration. Here crack lengths were monitored through a travelling microscope to determine crack growth rates. The data obtained in this manner was fitted to the Paris equation. Once again, crack propagation mechanisms were investigated from scanning electron micrographs of the fatigue surfaces.

2 Literature Survey

2.1 Tungsten Carbide-Cobalt

2.1.1 Introduction

WC-Co consists of hard, brittle tungsten carbide grains bonded by a soft, ductile cobalt binder. Typical microstructures are shown in *figures 3.1* and *3.2* in chapter 3. It is the combination of the properties of these two constituents which give WC-Co its excellent properties. At low and medium cobalt contents, the tungsten carbide grains form a skeleton which gives the material extremely high hardness. But the loss in toughness which usually results from such high hardness is prevented by the ductile cobalt binder. The result is a material exhibiting extreme hardness, while retaining reasonable toughness.

WC-Co is used in a number of engineering applications requiring high strength, hardness and abrasion resistance. It makes an excellent cutting tool - being used as the cutting edge in machine tools. Further, it is extensively used for drill bits in mining applications. Its high strength has led to its use in dies and anvils for diamond synthesis.

The cobalt content and tungsten carbide grain size can be varied to produce WC-Co grades with different properties.

2.1.2 The Manufacture of WC-Co

The following schematic, which is adapted from Brookes (1998), shows an outline of the WC-Co manufacturing process. A simplified description of the manufacturing process is also presented here.

The process starts with the refining of tungsten ore to get a metal powder. Typically, the ores used are wolframite or scheelite (Brookes, 1998). Once tungsten metal powder has been obtained, it is mixed with carbon black and fired at a temperature between 1400 and 2650 °*C* in a hydrogen atmosphere. Ball milling is used before firing to ensure satisfactory mixing between the tungsten powder and the carbon black. The tungsten powder is carburised during the firing to form WC (Brookes, 1998).

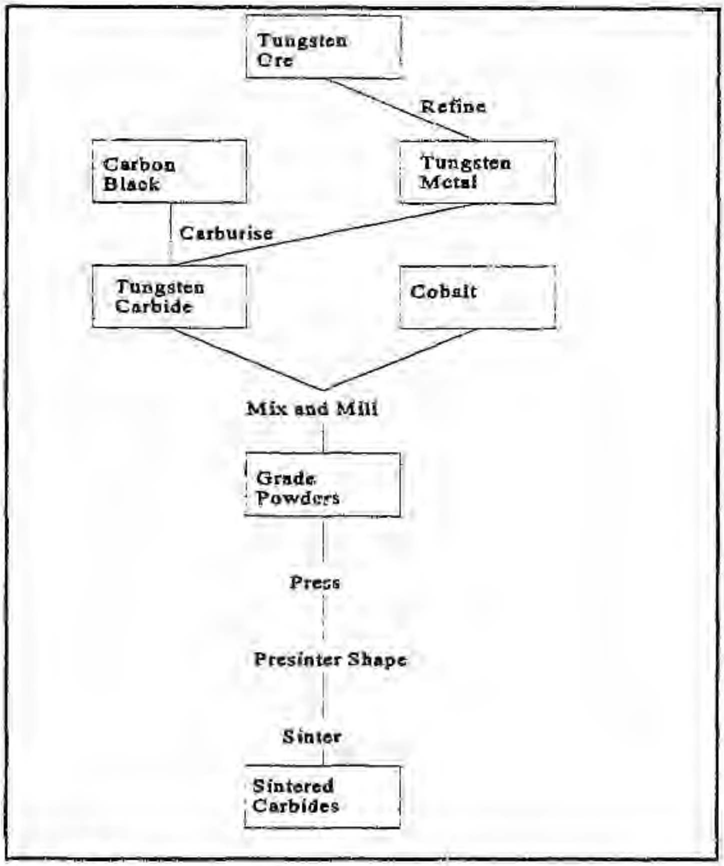

Figure 2.1
WC-Co Manufacturing Schematic
Adapted from Brookes, 1998

At this stage, ball milling is again used, this time for mixing the WC powder and the Co powder. The powders are milled together until the Co completely coats the WC powder. In order to facilitate handling of the mixed powders, the powders are often mixed with a lubricant and then granulated into pellets. The pellets or powders are then pressed into the shape of the final component. A variety of methods exist for forming the component from the powders, but these are beyond the scope of this work. Allowances must be made in the pressed dimensions for shrinkage during sintering (Brookes, 1998).

Before sintering, a pre-sintering stage of lubricant removal may be applied. This preheat can be part of the sintering furnace cycle. During this stage, the lubricant is burned out of the component. Once the lubricant is completely removed, the component is sintered between 1350 and 1650 °C. During sintering, the cobalt melts and wets the WC grains. The component shrinks considerably (between 18 and 26 percent in each linear direction). After sintering, the WC-Co component may be coated before use (Brookes, 1998).

2.2 Fatigue

2.2.1 Introduction

Suresh (1992) defines fatigue as a term which 'applies to changes in properties which can occur in a metallic material due to the repeated application of stresses and strains, although the term applies especially to those changes which lead to cracking or failure'. He states further that the term can be applied in the same way to non-metals. As the majority of engineering materials are subjected to cyclic loading in service, the study of their resistance to cyclic loads is important.

The fatigue process can be broken down into three distinct regions :

Stage 1. Crack initiation

During crack initiation, cyclic loading causes microstructural damage accumulation to initiate a microscopic crack. This microscopic crack grows and joins with other microscopic cracks to form what is known as the 'dominant crack' - the crack which will propagate to cause failure.

Stage 2. Stable crack propagation

This stage consists of stable crack growth - the crack will propagate at a steady rate dictated by the nature and magnitude of the applied loads.

Stage 3. Catastrophic failure

When the load bearing area of the component is sufficiently reduced by the fatigue crack, the component will fail in one final loading cycle.

There are two categories of methods for determining the fatigue properties of a material (Suresh, 1992). *Total-life approaches* involve determining the total fatigue life from initiation to failure as related to the stress amplitude ($\Delta\sigma$). This method is typified by the *S-N* fatigue characterisation discussed below. The *defect-tolerant approach* assumes the crack to already have initiated by means of an existing defect, and attempts to characterise the stable crack growth (stage 2 of the fatigue life). This approach is typified by the ΔK vs $\frac{da}{dn}$ curve determined using fracture mechanics principles. The ΔK vs $\frac{da}{dn}$ method is discussed in section 2.2.2.

As already mentioned, the stress amplitude - cycles to failure (*S-N*) approach attempts to characterise the entire life of the component from crack initiation to final failure. In this approach, the stress amplitude ($\Delta\sigma$) is plotted against the number of cycles to final failure (N). The result is a curve exhibiting the expected fatigue lifetime at a given stress amplitude (shown in *figure 2.2*). The typical *S-N* curve has an *endurance level* below which the fatigue life of the component is considered to be infinite. This is tantamount to a stress below which a crack will not initiate and the component should never fail.

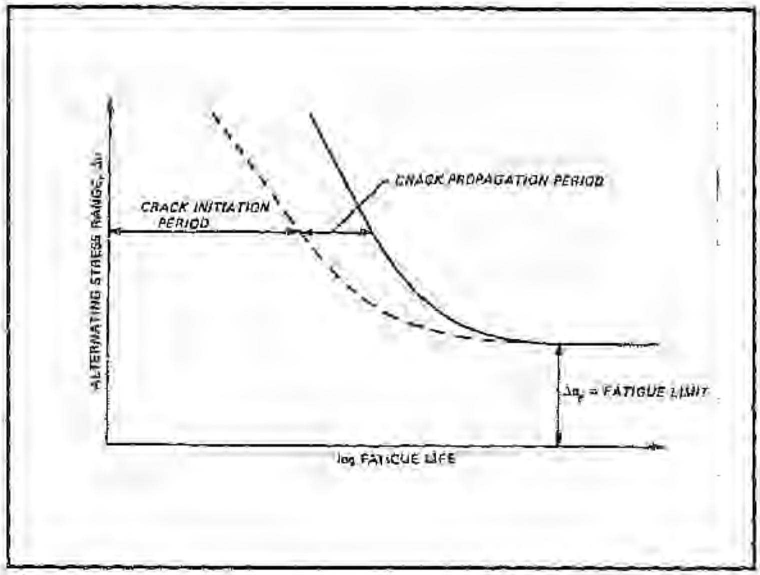

Figure 2.2
The *S-N* Curve
Ewalds & Wanhill, 1989

The time to initiate the dominant crack (stage 1), can, however, account for as much as 90% of the total fatigue lifetime (Suresh, 1992). This first stage is drastically shortened, if not removed altogether, by pre-existing material defects which can serve as crack initiation sites. This means that the size and distribution of defects within the material can play a decisive role in the fatigue life. As a result, considerable scatter can be obtained in *S-N* fatigue data (for example Polák *et al*, 1990). In an unnotched specimen, surface condition can also play a decisive role in determining fatigue lifetime using the *S-N* approach (for example Davies & Barbana, 1972). This introduces considerable risk for the designer using *S-N* data.

A better design methodology is to assume an existing defect (which is usually the case in engineering materials) and to base fatigue calculations on *remaining lifetime*. This means that the fatigue properties are being characterised in terms of *stage 2* (the stable propagation stage) of the fatigue process. The intention is to use fracture mechanics principles to estimate the time for the existing crack to grow to some critical dimension at a given stress amplitude. This approach to determining the fatigue characteristics of a material is discussed in the next section on the application of fracture mechanics to fatigue.

2.2.2 The Application of Fracture Mechanics Principles to Fatigue

By relating *ΔK*, the change in stress intensity factor during cycling, to $\frac{da}{dn}$, the crack growth rate, we relate the change in stress intensity factor to the crack growth rate. It has been shown that as long as the stress ratio, *R*, remains constant, then *ΔK* correlates to the growth rate (Ewalds & Wanhill, 1989).

So, $\frac{da}{dn}=f(\Delta K,R)$

As this method of obtaining fatigue data excludes the crack initiation stage, much of the scatter of the *S-N* method is removed. Fatigue crack initiation is a statistical process, and excluding crack initiation from fatigue data should remove much of the variation in results. Data in this format is also of far more use to the designer. Material fabrication processes will introduce defects into the finished product. When designing for fatigue, the engineer can assume defects of the smallest size detectable by non-destructive testing methods to already be present in the material. Lifetimes at given stress intensities can then be calculated from the *ΔK* vs $\frac{da}{dn}$ data.

Generally, the curve relating crack growth rate to *ΔK* exhibits three stages (*figure 2.3*). The first is a range below the threshold value (ΔK_0) where no growth takes place. The second is often a region of linear log relationship between crack growth rate and *ΔK* (Ewalds & Wanhill, 1989). The most widely accepted description of this part of the crack growth rate curve is the Paris equation :

$$\frac{da}{dn}=C(\Delta K)^m$$

The third region is one of final failure, where K_{max} (the maximum stress concentration) approaches K_{IC}, the fracture toughness.

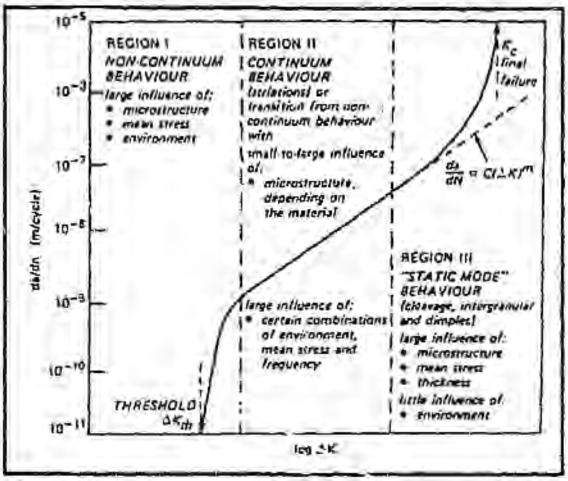

Figure 2.3
The fatigue crack growth rate curve
Ewalds & Wanhill, 1989

2.2.3 Stress Analysis of Cracks Under Monotonic Loading Conditions

The stress distribution ahead of a crack is recognised to contain a singularity at the crack tip which is described by an equation of the form :

$$\sigma_{ij} = \frac{K}{\sqrt{2\pi r}} f_{ij}(\theta) + ...$$

where

K = stress intensity factor
r, θ = polar coordinates of a point with respect to the crack tip (see *figure 2.4*)

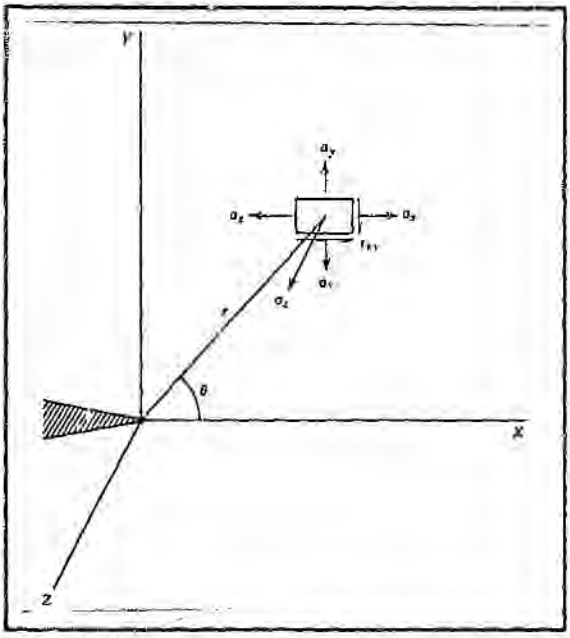

Figure 2.4
Distribution of stresses in vicinity of a crack tip
Hertzburg, 1976

As a result of this stress singularity, there will be a region ahead of the crack tip where the local stresses are greater than the yield strength of the material. Where the stresses exceed the yield strength of the material, a region of plastically deformed material will result (Hertzburg, 1976). This region is known as the *plastic zone*. Linear elastic fracture mechanics applies only to cases where the plastic zone is small in comparison to the crack length and the cracked body still behaves in an elastic manner. When a monotonic load is applied to the crack, there will be a region of elastically strained material surrounding the plastic zone. This region is termed the elastic zone.

2.2.4 Stress Analysis of Cracks Under Cyclic Loading Conditions

A plastic zone will form in front of a propagating fatigue crack during the loading part of its cycle. This zone is equivalent to the plastic zone formed under monotonic loading conditions and is thus referred to as a *monotonic plastic zone* (Suresh, 1992). A second plastic zone forms as a result of unloading the fatigue crack: when the fatigue crack is unloaded, a load of magnitude $-\Delta P$ is applied to the crack (as the load on the crack is diminished by ΔP). This reduction in load instigates a *reversed plastic flow (figure 2.5)*. The result is a *reversed flow plastic zone* embedded in the monotonic plastic zone. So a fatigue crack which is not fully unloaded (i.e. still under load $P_{min} = P_{max} - \Delta P$) will have a region of reversed plastic flow in its monotonic plastic region. In this region of reversed plastic flow, residual *compressive* stresses are induced.

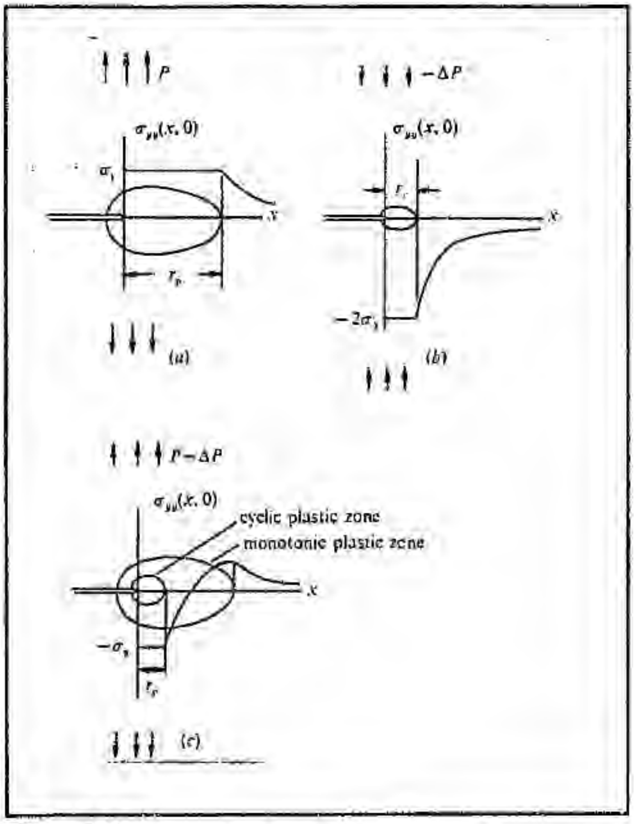

Figure 2.5
Schematic representation of the development of the cyclic plastic zone on unloading:
(a) A monotonic plastic zone is created by load P_{max}
(b) Reducing the load by ΔP results in a reversed plastic zone forming
(c) The resulting stress distribution due to the superimposition of (a) and (b)
Suresh, 1992

In *figure 2.5(c)*, the stress distribution resulting from the combination of the monotonic and reversed flow plastic zones can be seen. Ahead of the crack tip the stresses are seen to be compressive and subsequently change to tensile somewhere between the boundaries of the reversed plastic zone and the monotonic plastic zone. This is consistent with the notion that residual stresses are self-equilibrating (Suresh, 1992) - residual compressive stresses at the crack tip are offset by residual tensile stresses away from the crack tip.

2.2.5 Fatigue Crack Closure

As has already been explained, a region of monotonic plastic deformation forms ahead of a growing fatigue crack. As the crack grows, a wake of monotonically deformed material forms along its sides as in *figure 2.6* (Ewalds & Wanhill, 1989). As this wake is the result of tensile loading, the material in it will be elongated normal to the crack. When the crack is open, this elongated material is of no consequence as it will simply be displaced along the crack sides. When the crack closes, however, the elongated material along the crack flanks will cause the crack sides to come into contact before the minimum load (P_{min}) is reached. This means that the crack will be fully closed before the minimum load (P_{min}) is reached.

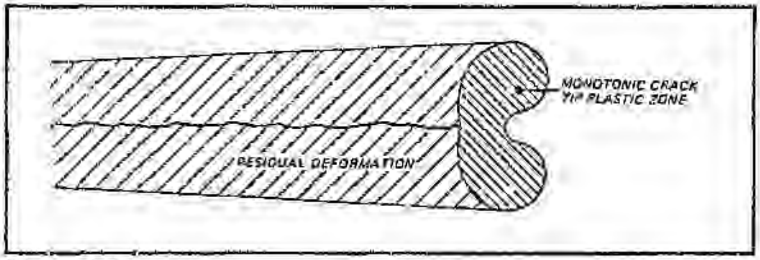

Figure 2.6
Wake of residual deformation around a fatigue crack
Ewalds & Wanhill, 1989

In a Mode I loading regime, no growth will take place while the crack is closed (as Mode I is an opening mode). As the crack is fully closed before the minimum load (P_{min}) and hence before the minimum stress intensity factor, K_{min} is reached, the effective stress intensity range in which the crack can propagate is smaller than ΔK (Ewalds & Wanhill, 1989). It has, in fact, been suggested that the crack will only grow when it is fully open. If σ_{op} ($>\sigma_{min}$) is the stress intensity at which the crack is fully open, then ΔK_{eff} arising from $\sigma_{max} - \sigma_{op}$ is the effective stress intensity range during which crack growth can take place. (Suresh, 1992) .

A *compliance* plot is used to experimentally obtain σ_{op}. A displacement gauge is placed behind the crack tip to measure the crack opening (displacement) in the load cycle. The displacement (δ) measured by the gauge is then plotted against the applied stress (or equivalently against K). The σ - δ plot in the *figure 2.7* shows that the crack remains fully open while the stress is decreased from σ_{max} (at point A) to σ_{op} at (point B). The constant slope between A and B is the same as the measured stiffness (δ versus σ) of the equivalent specimen with a saw-cut the same length as the fatigue crack (Suresh, 1992). This means that no crack closure has occurred due to plastic deformation. After point B, the slope of the curve deviates from the straight line - showing that the crack is closing. The curve becomes linear again after point C. The slope of CD is the same as the stiffness of the equivalent specimen without a fatigue crack (shown by slope OE), indicating that the crack is fully closed after point C.

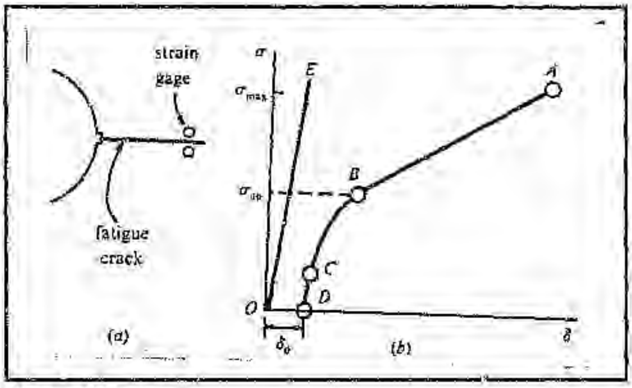

Figure 2.7
A schematic of the relationship between the applied stress and the displacement measured by the strain gauges
Hertzburg, 1976

As *R* (the stress ratio) increases, so ΔK_{eff} becomes closer to ΔK (the proportion of ΔK during which the crack is closed becomes less as ΔK increases with increasing *R*). This may be a reason for the effect that *R* has on crack growth rates. In other words, ΔK_{eff} may account for the effect that *R* has on $\frac{da}{dn}$ (Ewalds & Wanhill, 1989). So it may be:

$$\frac{da}{dn}=f(\Delta K_{eff})$$

2.2.6 Fatigue Crack Growth from Notches

Plastic and elastic zones can be found at the root of a notch in much the same way as at a crack tip as shown in *figure 2.8* (Ewalds & Wanhill, 1989). Therefore, a fatigue crack growing from a notch may start growth under conditions of local plasticity. The size of the plastic zone arising from the notch will initially be very large when compared to the size of the developing crack. In this situation, Linear Elastic Fracture Mechanics will not be able to predict the behaviour of the crack. Once the crack has grown through the plastic zone, it then has to grow through the elastic zone of the notch before reaching the bulk stress-strain field of the material. Even in the elastic zone, the crack growth rates are not always correlated by ΔK.

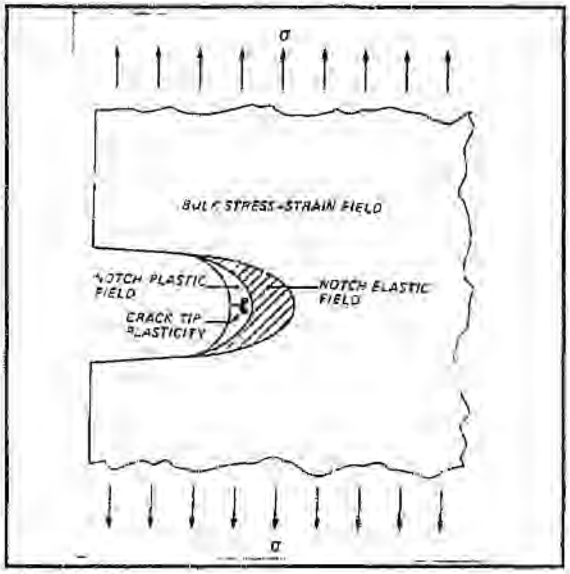

Figure 2.8
Growth of a small fatigue crack at a notch
Ewalds & Wanhill, 1989

The exact manner in which a fatigue crack will deviate from the usual ΔK vs $\frac{da}{dn}$ curve is determined by the nature of the notch. When the crack is in the plastic zone of the notch, its growth rate will be higher than that indicated by the ΔK. Therefore, if the notch has a plastic zone, crack growth rates will be high until the crack grows out of the notch plastic region.

If the notch has an elastic zone, the behaviour of the crack in the elastic zone will depend on the crack length. This is because short cracks tend to grow faster than long cracks at the same ΔK (Ewalds & Wanhill, 1989). This phenomenon is known as the *Short Crack Problem*. One of the causes of this phenomenon is difference between residual deformation in a short crack and in a long crack as in *figure 2.9*. A short crack will have less residual deformation behind it, and therefore less crack closure and a higher growth rate. A longer crack will have more residual deformation in its wake and hence will have greater crack closure and a slower crack growth rate.

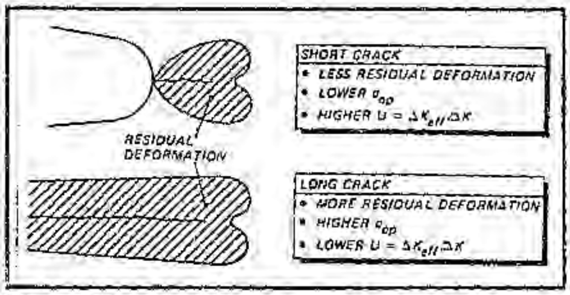

Figure 2.9
Differing plasticity in the wakes of short and long cracks with the same ΔK
Ewalds & Wanhill, 1989

So a short crack growing in the elastic zone of a notch will exhibit faster crack growth than the ΔK- value would suggest. If the crack is not short, then it will exhibit normal growth in the elastic zone. If a notch has only an elastic field (and hence the crack starts growing in the elastic zone), initial crack growth will be faster than would be predicted from the relevant ΔK value.

2.2.7 Fatigue Crack Initiation in Ductile Materials

In ductile materials, dislocation movement plays a very prominent role in fatigue. Fatigue cracks tend to initiate either at the surface or at a defect in the material (Ewalds & Wanhill, 1989). Nucleation sites can be generated by the formation of persistent slip bands (PSBs). PSBs are surface notches formed by cyclic slip. They resemble a series of peaks and troughs (extrusions and intrusions) on the surface of the material. In monotonic loading, slip planes on the surface tend to be regular and resemble a 'staircase' in that they form a series of slip steps. In cyclic loading, the slip systems have the effect of roughening the 'surface' by the formation of these intrusions and extrusions.

PSBs are the surface terminations of dense bands of slip in the material. They are called persistent as etching will not remove them (thus denoting permanent damage) and if they are polished off and the material is subjected to further cyclic loads, they will recur at the same spots. Continuing slip will deepen the intrusions, which act as prime sites for crack initiation. These surface features can be regarded as the initial stages of microcrack formation (Hertzburg, 1976).

A simplified model for the formation of PSBs is supplied by Ewalds & Wanhill (1989). The applied load causes dislocation movement and these dislocations pile up at grain boundaries. At the boundaries the dislocations tend to form pairs called dipoles as a result of their interacting stress fields. An arrangement of vacancy dipoles will mean that the material between them has fewer half planes of atoms than the surrounding material (see *figure 2.10*). These half planes of atoms will be at the surface forming an extrusion. Similarly, an arrangement of interstitial dipoles will have more atom half planes between them which have been removed from the surface, thereby forming an intrusion.

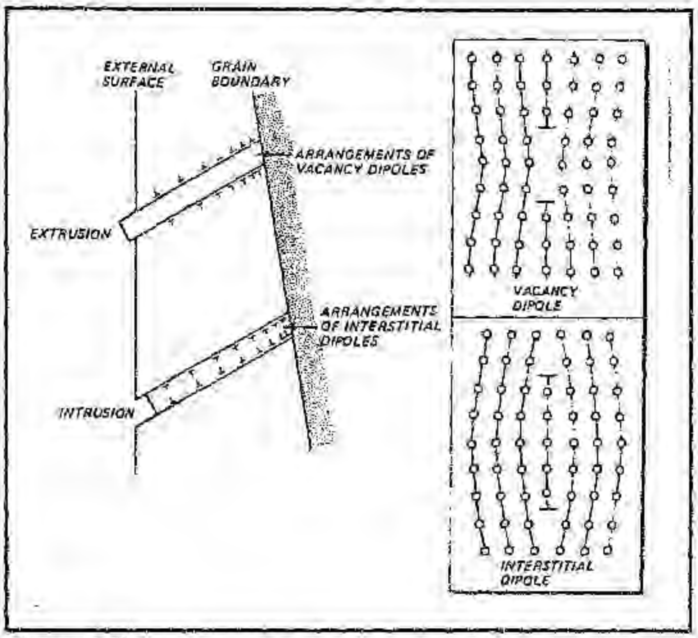

Figure 2.10
Simplified dislocation model of extrusions and intrusions
Ewalds & Wanhill, 1989

Cyclic slip will cause the intrusion cracking to extend a few grains long into the material, thereby initiating a fatigue crack. The fatigue crack then moves into stage two of the fatigue life - stable propagation. As the crack initiation is a result of cyclic slip, the initial crack direction will be at 45° to the applied load. This is because the maximum resolved shear stress which causes dislocation movement is at 45° to the applied load, i.e. in the direction of maximum shear stress. Once the Mode I loading crack starts to propagate, however, its direction will change to perpendicular to the applied load.

2.3 Fatigue in Compression

Generally it has been accepted that fatigue cracks remain closed under compressive forces, and hence will not propagate when in a totally compressive stress field. It has come to be recognised, however, that fatigue cracks can initiate and propagate under compressive loads (Hubbard, 1969; Johansson *et al*, 1970; Reid *et al*, 1979; Suresh, 1985). This fatigue phenomenon is believed to be a result of local tensile stresses at the crack tip (Suresh, 1985).

Analogous with the region of compressive stresses ahead of a crack propagating in tension, there can be a region of residual *tensile* stresses ahead of a crack propagating under compression (Suresh, 1985). These residual stresses can cause crack initiation and propagation to arise under a far-field compressive stress. This has been used to propagate fatigue cracks in notched specimens (Reid *et al*, 1979; Suresh, 1985).

In these tests, notched specimens were subjected to compressive loads. During the application of the initial load, a region of monotonic plastic deformation occurs at the notch tip. This region is comparable with the monotonic plastic zone that forms during the loading cycle of a crack under a far-field tensile load. Finite element studies have shown that when the compressive load is removed, large residual tensile stresses are generated at the notch-tip (Suresh & Brockenbrough, 1988). These tensile stresses arise from a process akin to that which gives rise to compressive stresses in front of a tensile fatigue crack (see *figure 2.11*). The unloading process causes a zone of reversed flow ahead of the notch tip. These large residual tensile stresses form because there is no contact (closure) in the wake of the notch root (Suresh, 1992). When the notch is unloaded, it returns to its original open position. The material at the notch tip which has undergone compressive deformation is subjected to tensile stresses by the notch opening. This means that if a long, sharp fatigue crack rather than a notch was subjected to compressive loading, such a residual tensile field would probably not be generated as the crack would remain closed on unloading.

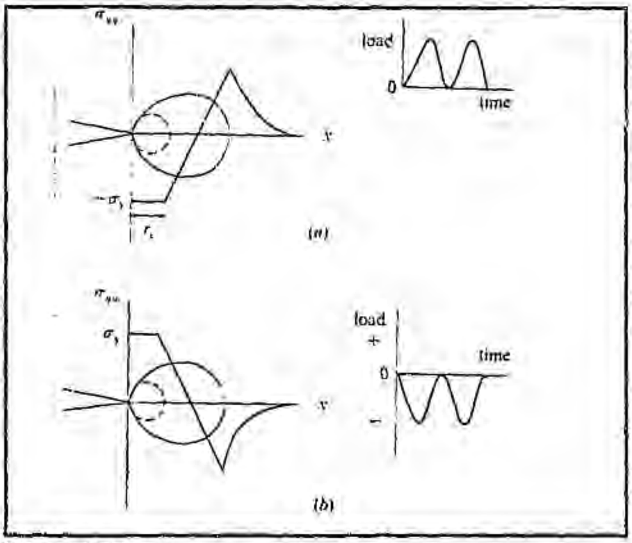

Figure 2.11
near-tip stress variation for
(a) cyclic tension
(b) cyclic compression
Suresh, 1992

The residual tensile stresses generated in the first loading cycle are sufficient for crack initiation and propagation to occur at the notch root. Once the crack starts to grow, the faces of the crack tend to remain partially or fully closed during some portion of the fatigue cycle (Suresh, 1992). Experimental measurements of crack closure show that as the compression fatigue crack grows, the fraction of the loading cycle for which the crack is open decreases (Suresh, Christman & Bull, 1986). The increasing crack closure causes crack growth to decelerate and then arrest as shown in *figure 2.12*.

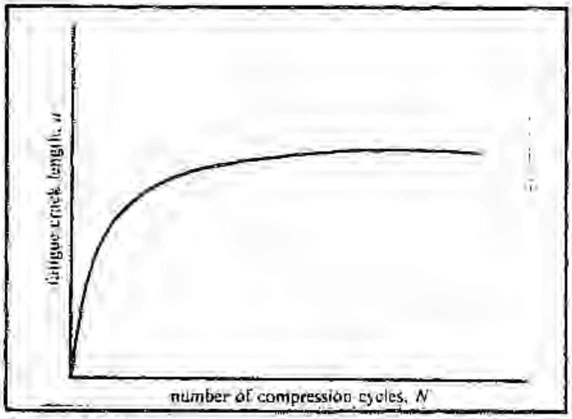

Figure 2.12
Typical variation of crack length with the number of compressive cycles
Suresh, 1992

It must be noted, however, that the region of residual tensile stresses generated in far-field compressive loading is still surrounded by the region of compressive stresses (the compressive plastic zone formed as a result of the initial compressive loading). Suresh (1991) explains this by stating that residual stresses are self-equilibrating. Once the crack grows to the end of the tensile residual stress region, it will encounter residual *compressive* stresses. In addition, when the end of the residual tensile stress region is reached, there is no longer any driving force for crack growth. These two factors, together with increasing crack closure with increasing crack length, will initially cause the crack to decelerate, and then to arrest entirely.

Cracks grown in this manner under compressive loads can be regarded as 'true' fatigue cracks for the following reasons (Suresh, 1992):

- The compressive fatigue cracks grow perpendicular to the applied stress (as do Mode I fatigue cracks). Cracks grown under monotonic compressive loads tend to grow parallel to the applied load.
- The crack length gradually increases as the number of cycles increases
- This effect is not a result of environmental effects as it has been shown to take place in a vacuum
- The rate of crack growth has been shown to be strongly influenced by mechanical factors such as mean stress, stress state and stress range
- Crack closure plays an important role in determining the rate of crack growth

The self-arresting characteristic of compression-fatigue cracks is of particular significance when attempting to introduce stable cracks into brittle materials without catastrophic failure (Suresh, 1985). This is because stable (self-limiting) cracks can be introduced into brittle materials under compressive loads, where introducing the crack under tensile loads would lead to catastrophic failure. Both toughness (K_{IC}) and fatigue testing (for growth rate versus ΔK information) require the presence of pre-existing cracks and compression fatigue can be used to introduce stable cracks into brittle materials for this purpose.

Fatigue cracks under far-field compression-compression loading have been grown in a number of different materials. These include:

7075-T6 aluminium alloy (Hubbard, 1969)
7075-T7351 aluminium alloy (Holm *et al*, 1986)
WC-Co (Johansson *et al*, 1970; Suresh & Sylva, 1986; Human, 1988)
normalised mild steel and EN8 (Reid *et al*, 1979)
2.35Cr-1Mo steel (Suresh, 1985; Holm *et al*, 1986)
polycrystalline alumina (Ewart & Suresh, 1986; Suresh *et al*, 1978)
hot-pressed silicon nitride (Suresh, 1988)
fine-grained zirconia (Suresh, 1988)
Portland-cement-based concrete (Suresh, 1988)

All these materials displayed the same compression fatigue crack growth characteristics: The cracks advance along a plane macroscopically perpendicular to the uniaxial far-field compressive stress axis and all the cracks arrest after progressively slowing down (Suresh, 1991).

As can be seen, this technique has been used to grow fatigue cracks in both ductile and britt materials. In fact, the compression fatigue technique has allowed study of fatigue mechanisms brittle materials (Suresh, 1991). As brittle materials are much stronger in compression than in tension, they are most widely used in compression. In addition, cyclic compression has thus far proved to be the only way in which to introduce and propagate a stable fatigue crack in many brittle materials. So most of the research into stage 2 fatigue in brittle materials has been conducted under compressive cyclic loads (Suresh, 1990).

2.4 Fatigue Cracks in Brittle Materials

The importance of dislocation movement in the initiation of fatigue cracks in ductile materials has already been discussed. Traditionally, the assumption has been that dislocation movement is necessary for fatigue to take place and this immediately raises questions about fatigue and fatigue mechanisms in brittle materials, where little chance of dislocation movement causes the material to fracture before substantial deformation can take place. Fatigue phenomena have, however, been shown to take place in brittle materials (above).

Engineering solids can be broadly classified into three categories (Suresh, 1991):

(i) highly brittle solids
(ii) semi-brittle solids
(iii) ductile (non-brittle solids)

The category of highly brittle solids consists of ionically and covalently bonded solids such as ceramics and diamond.

The category of semi-brittle solids contains materials such as b.c.c. metals and glassy polymers. In these materials a limited amount of plastic deformation will take place before brittle cracking.

Ductile solids (such as f.c.c. solids) conform to the fatigue behaviour already discussed.

Fatigue by cyclic compression has been induced in all three categories of engineering materials (see the list given in the previous section). Tensile fatigue growth rates conforming to the Paris regime have been induced in ceramics (Suresh, 1991). This means that mechanical fatigue effects distinctly different from static loading effects can be induced in brittle materials.

The observed fatigue in brittle materials suggests that *kinematically irreversible* microscopic deformation (of which dislocation movement is an example) is necessary for fatigue (Suresh, 1992), but fatigue damage need not only result from dislocation movements, it can also result from other processes such as microcracking and martensitic transformations.

There are known to be several different means whereby a crack can be initiated in a brittle solid. For example, brittle solids contain internal microscopic defects known as Griffith's flaws and surface defects. Microcracking as a result of residual stresses at grain boundaries and phase interfaces has also been shown to provide nucleation sites for fatigue cracks.

The mechanisms that lead to the generation of residual stresses under compressive loads have been investigated in polycrystalline alumina (Ewart & Suresh, 1986). Notched specimens were used. Microcracks were found to initiate at the grain boundaries in the vicinity of the notch. These microcracks are attributed to residual stresses at the grain boundaries arising from thermal contraction anisotrophy. The application of the compressive loads increases the extent of the microcracking. Residual tensile stresses result at the notch tip if the microcracks remain open during unloading of the maximum far-field compressive load. Frictional sliding (due to the cyclic load) of the faces of these microcracks causes fatigue cracks to initiate on adjacent grain boundaries. Further cyclic loading results in the microcracks coalescing into a macrocrack. Once again, the ultimate length that the crack grows to is limited by the extent of the damage ahead of the crack tip. When a crack is initiated in compression, further cycling results in the formation of debris within the crack due to the repeated contact between the crack walls. This debris can wedge the crack open, thereby having an effect on the rate of crack advance (Suresh, 1990). So the rate of fracture will be governed by two conflicting processes :
(1) the generation of debris which wedges the crack open and
(2) macroscopic closure along the crack wake as the crack grows.

In addition to the fatigue processes witnessed in brittle materials, brittle materials will exhibit stable fatigue growth resembling that of metals if a ductile phase is introduced (Suresh, 1991). This is seen to be the case in WC-Co.

2.5 Compression Fatigue in WC-Co

Johansson *et al* (1970) used cylindrically shaped test pieces with enlarged ends to determine the fatigue life time of WC-Co grades with varying cobalt contents. These pieces were tested to destruction where the test piece shattered under the applied cyclic compressive loads. Resistance to fatigue under compression was found to be greater than resistance to tensile fatigue. Further, it was found that the resistance to fatigue decreased with increasing cobalt content and grain size. No evidence of a fatigue limit was found. Of interest is the fact that limited scatter was obtained in the results.

Subsequent studies used the single-edge-notched geometry loaded in uniaxial compression as shown in *figure 2.13* (Suresh & Sylva, 1986; Godse *et al*, 1987; Human, 1988). In these studies, crack length was monitored as a function of the number of cycles.

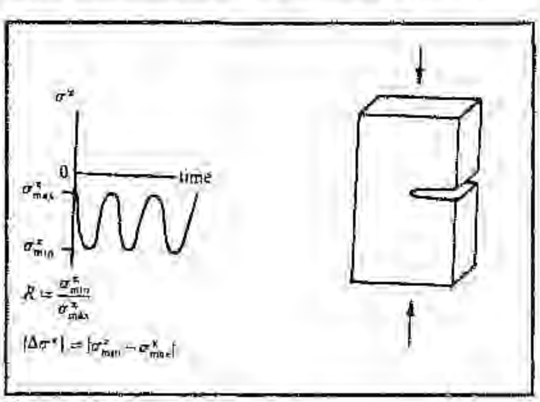

Figure 2.13
Schematic showing the loading of a notched specimen in cyclic compression
Suresh, 1992

Suresh & Sylva's study explained the mechanisms whereby residual stress zones are formed in WC-Co as a combination of those found in metals and those found in brittle materials. The compression crack path was seen to be mainly along the interface between the cobalt binder and the carbide grains. Some evidence of cracking was seen in the binder phase, but there was no cracking visible through the carbide grains. The formation of the residual stresses necessary for compressive fatigue cracking was explained as follows:

(i) Residual stresses are introduced by the plasticity of the cobalt binder:

The binder behaves in a ductile manner. So dislocation movement in the binder results in the formation of monotonic and reversed flow plastic zones. Residual tensile stresses result.

(ii) Residual tensile, compressive and shear stresses exist near the carbide-binder interface as a result of different thermal contraction effects (thermal mismatch):

These residual stresses can lead to microcracking under a far-field applied load.

(iii) A damage zone at the notch tip, characterised by a population of microcracks at the carbide-binder interface, can result in a local stiffness reduction. If a fraction of these cracks remain open during the unloading portion of the compression cycle, residual stresses will result.

(iv) Frictional sliding of interfacial microcracks due to the compressive cycling also adds to the residual tensile stresses:

> Once microcracks have formed, further cyclic loading will cause matching faces of the microcracks to *rub* against each other. The resulting friction and shear along the carbide-binder interfaces can promote further microcracking at adjacent interfaces.

It must, however, be noted that the study by Luyckx (1976) documented the development of slip steps in WC grains subjected to reversed bending fatigue. This suggests that in addition to the mechanisms suggested by Suresh and Sylva, cyclic plasticity within the carbide grains may also play a role in the development of residual stresses.

Godse, Gurland and Suresh investigated the residual stresses ahead of a compression fatigue crack that has arrested. It was found that R and crack tip closure affect the stress state at the crack tip. It was concluded that the measurement of fracture toughness can be affected by residual stresses arising from the compression precracking. A method was suggested to eliminate these residual stresses:

(i) subject the specimen to cyclic compression until the crack arrests
(ii) subject the specimen to tensile fatigue in a bend configuration
(iii) monitor the crack length until a state of arrest is detected (due to residual compressive stresses)
(iv) when crack arrest is detected, increase the maximum stress intensity (K_{max}) by $0.25\ MPa\sqrt{m}$
(v) continue growing the crack at increasing loads until it no longer arrests

At this stage, all residual stresses should have been eliminated.

Presumably Godse *et al* do not suggest a stress-relieving anneal to eliminate residual stresses as their method gives an indication of the extent of the residual stress zone.

In 1988, Human confirmed the propagation of stable cracks in WC-Co and showed that the final crack length can be controlled by the load range and notch geometry. Increases in load range led to increased final crack lengths, as did longer notches. Once the specimens had been cracked under compression, fracture toughness tests were conducted on them. The values obtained from these tests were low when compared to the K_{IC} values reported in the literature. This may suggest that residual stresses at the crack tip had an effect. The method suggested by Godse *et al* was applied to one specimen, and a larger K_{IC} value was obtained in the subsequent fracture toughness test.

Iizuka & Tanaka (1991) also used compression fatigue precracks for fracture toughness testing in single-edge-notched specimens. Instead of uniaxial loading, however, they applied cyclic compressive loads in a four-point bending test as in *figure 2.14*. Once again, stable crack propagation was induced and final crack length was increased by higher applied loads. In order to obtain longer cracks, aqua regia was used to remove contact portions in the wake of the arrested crack. The cracks with a sharper crack tip were then subjected to compressive cycling again, and the arrested cracks restarted. These cracks also progressively slowed down until they re-arrested. The K_{IC} values obtained, however, were in very good agreement with those obtained using other pre-cracking methods. In fact, the authors stated that the maximum amount of residual stresses remaining after compressive precracking could not be enough to influence subsequent fracture toughness tests.

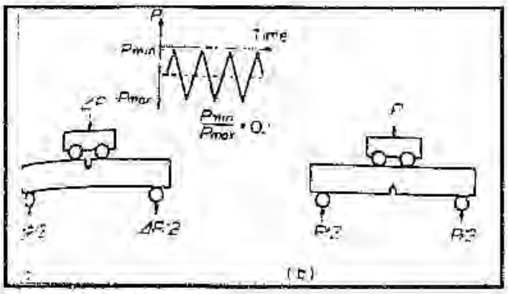

Figure 2.14
Schematic diagram of Single Edge Notched Bending (SENB) specimen subjected to
(a) compressive fatigue
(b) tensile fatigue
in a four-point bend

the last two paragraphs show, there is some uncertainty as regards the effect of residual resses on subsequent tests. The following table summarises the views of researchers on this point:

Table 2.1
The effect of residual stresses

Do Residual Stresses Affect the Results of Subsequent Tests?		
Researchers	**Yes**	**No**
Suresh, 1985		X
Suresh & Sylva, 1986		X
Christman & Suresh, 1986		X
Ewart & Suresh, 1987		X
Suresh *et al*, 1987		X
Godse, Gurland & Suresh, 1987	X	
Human, 1988	X	
Suresh, 1988		X
Iizuka & Tanaka, 1991		X

2.5.1 Fracture Surfaces Arising From Compression Fatigue

Suresh & Sylva (1986) noted that the crack path was primarily along the interface between the carbide grains and the cobalt binder. Some evidence of growth in the binder phase was noted, but there was no evidence of any cracking in the carbide grains. The material that Suresh & Sylva used was WC-25wt.%Co. Observations of the fracture surface after testing revealed a uniform crack front through the centre thickness of the specimen. It was, however, noted that some non-uniformity of crack front occurred at the slower growth rates just before crack arrest. It is thus implicit that the crack front could be distinguished.

Human (1988), using WC-10wt.%Co reported that the fracture path included transgranular fracture through the carbide grains, fracture along the interface between the carbide grains and the cobalt binder, fracture along the interface between carbide grains and fracture in the cobalt binder. In addition, the fracture surface transition from compression fatigue fracture to fast fracture was reported as being visible at low magnifications. Under the SEM, however, the compression fatigue front was not distinguishable.

Iizuka & Tanaka (1991) did not report on the fracture path in their WC-8%Co material. They did, however, note differences between the compression fatigue fracture surface and the fast fracture surface. They reported that the difference between the fracture surfaces was mainly in the amount of deformation in the cobalt ligaments. There were large amounts of deformation visible on the fast fracture surfaces, but this was not the case in the compression fatigue surface.

A possible explanation for the differing fracture path results reported by Human and Suresh & Sylva may be the vast difference in the Co-content of the materials that they used.

2.6 Tensile Fatigue in WC-Co

The following table is an overview of studies conducted into tensile fatigue in WC-Co.

Table 2.2
Tensile fatigue studies in WC-Co

Researchers	Year	Data	Test	Paris Law	Other
Davies & Barbana	1972	*S-N* curves WC-25%Co	- rotating beam cantilever machine - high frequency *da/dn* vs ΔK	n/a	- Detected slow crack growth - Improvement in fatigue life with improved surface polish - considerable scatter in results
Evans & Linzer	1976	*da/dn* vs ΔK WC-6%Co	double torsion	yes m = 11	-WC-Co exhibits crack -tip plasticity - m was found to increase with increasing average stress intensity (K_{ave})
Almond & Roebuck	1980	*da/dn* vs ΔK WC-11%Co	wedge-indentation precrack and 4-point bend	yes m = 10	Cyclic loading causes failure mode of binder to change from ductile to brittle
Evans	1980		Review of fatigue in ceramics		Introduction of metallic phase into a ceramic introduces potential for fatigue
Lueth	1981	*da/dn* vs ΔK 6 - 25% Co	double torsion	yes m between 15 and 25	- Lower Co materials have a higher m-value - There is a threshold value for fatigue crack growth - Fatigue crack growth resistance increases with increasing K_{IC}
Knee & Plumbridge	1984	*da/dn* vs ΔK 7.5 - 25% Co	4-point bend	yes $R = 0.1$: $5<m<10.8$ $R = 0.5$: $3.9<m<24$	- there is a microstructure independent threshold - Threshold value depends on stress ratio R (ie crack closure) - m increases with decreasing Co content and WC grain size
Roebuck & Almond	1988	*da/dn* vs ΔK	Review	yes $5<m<20$	High m-values should be interpreted as indication that crack growth is composite of stage 2 and 3 crack propagation
Fry & Garrett	1988	*da/dn* vs ΔK 6 - 25% Co	double torsion	yes $10<m<20$	- Frequency has no effect - Increased mean free path leads to decreased fatigue crack growth rate and affects m

Researchers	Year	Data	Test	Paris Law	Other
Polák, Obrtlik & Vrbka	1990	*S-N* WC-9%Co	smooth specimens subjected to push-pull loading	n/a	- Considerable scatter in *S-N* results - *S-N* scatter depends on defects present
Schleinkofer, Sockel, Schlund, Görting & Heinrich	1995	*S-N* WC-6%Co	static, monotonically increasing & cyclic loads	n/a	- Hard metals do exhibit a 'true' fatigue effect - cyclic loading lowers the subsequent inert strength due to subcritical crack growth - SEM and TEM investigations suggest that fatigue processes are located mostly in the Co phase
Schleinkofer, Sockel, Schlund Kindermann, Schulte, Werner Görting & Heinrich	1996	*S-N*	- High temperature - CVD-coated	n/a	- WC-Co has a higher sensitivity to fatigue at 700°C than at room temperature
Schleinkofer, Sockel, Görting & Heinrich	1996	*S-N*	static, monotonically increasing & cyclic loads	n/a	- TEM investigations show that in samples subjected to cyclic loading, a martensitic phase transformation from f.c.c. to h.c.p. structure occurs in the Co ligaments
Schleinkofer, Sockel, Görting & Heinrich	1996	*S-N*	static, monotonically increasing & cyclic loads	n/a	-Hard metals do exhibit a 'true' fatigue effect - fatigue effects occur during cyclic loading at stress amplitudes which are much smaller than the bending strength of the material
Kursawe, Schulte & Sockel	1998	*S-N*	static, monotonically increasing & cyclic loads	n/a	- TEM investigations show that the f.c.c to h.c.p transformation and the resulting embrittlement is followed by subcritical crack growth in the Co phase.

2.6.1 *S-N* Testing

Davies and Barhana (1972), Polák *et al* (1990) and Schleinkofer *et al*, (1995, 1996) conducted *S-N* fatigue tests. As the testing techniques used by the different studies differ considerably, it is expected that there would be some disparity in their results.

Davies and Barhana (1972) reported that the fatigue life improved considerably with improved surface polish. As they used unnotched specimens, this would be consistent with the notion of a rougher surface providing potential fatigue initiation sites. In addition, considerable scatter was reported in the results, suggesting a sensitivity to imperfections in the material.

Obrtlik *et al* (1990) also reported considerable scatter in their results. In explaining the fatigue processes in WC-Co, they reported that at stresses smaller than 1650 *MPa* the WC only deforms elastically while the plastic deformation is concentrated in the Co-binder. Cyclic loading below 1650 *MPa* results in cyclic plastic strain concentrated in the binder phase. They suggested that this strain causes extrusion and intrusion formation. As has been described in *section 2.2.7*, these surface irregularities lead to the formation of a fatigue crack. The resulting fatigue *S-N* curve will depend on the size of subcritical defects in the material, as these defects serve as locations for fatigue crack initiation. The considerable scatter obtained in the fatigue results is therefore explained by the dependence of fatigue life on subcritical defects.

Obrtlik *et al* (1990) conducted their tests at higher loads than Davies and Barbana (1972), and so their reported lifetimes are correspondingly shorter.

Schleinkofer *et al*, (1995) compared the behaviour of specimens loaded under static, monotonically increasing and cyclic loads in an attempt to gain greater understanding of hard metals under cyclic loads. comparison of the different loading regimes clearly showed that fatigue takes place. Measurements of inert strengths after the material had been subjected to cyclic loading showed that damage by subcritical crack growth lowered the reliability of the material. Microstructural differences were found to affect the fatigue properties of the material, but the complexity of WC-Co made it difficult to determine general rules as to how microstructure affects fatigue.

Schleinkofer *et al*, (1996) investigated fatigue at high temperatures and the effects of coatings on the fatigue life. Elevated temperature tests were conducted to closely model the conditions when WC-Co is used as a cutting tool. The CVD (Chemical Vapour Deposition) process was shown to have no effect on the mechanical properties of the bulk material. Another result was that the cyclic strength was lower at 700°C than at room temperature.

2.6.2 Growth rate ($\frac{da}{dn}$ vs ΔK) testing

A number of factors have been shown to affect the growth rate of fatigue cracks in WC-Co. These are summarised below. In addition, findings concerning possible threshold ΔK values at which fatigue crack are discussed. Finally, various interpretations of the m-values obtained in growth rate testing are discussed.

The m-value appearing in the Paris equation ($\frac{da}{dn}=C(\Delta K)^m$) is of considerable significance. The higher the value of m, the greater the growth rate and the rate at which the growth rate increases with increasing load or crack length. The m-value can therefore be regarded as a measure of a materials resistance to fatigue crack growth - the higher the value of m, the more susceptible to fatigue crack growth the material will be.

2.6.2.1 The effect of cobalt content on growth rate

Lueth (1981) reported that increasing cobalt content resulted in lower m-values and hence better resistance to fatigue crack propagation - a result opposite to that reported by Johanssen *et al* (1970) in their compression fatigue tests. Knee & Plumbridge (1984) supported Lueth's findings that m decreased with increasing cobalt content. Fry & Garrett (1988) also showed that increasing the cobalt content decreased the fatigue crack growth rate.

2.6.2.2 The effect of grain size on growth rate

Knee & Plumbridge (1984) found that m decreased with increasing grain size. This finding supports the result of Johanssen *et al* (1970) in their earlier compression fatigue tests. Fry & Garrett (1988) also in agreed that increasing grain size improves resistance to fatigue crack growth.

2.6.2.3 Correlation of growth rates to K_{IC}

Lueth (1981) reported that resistance to fatigue crack growth in WC-Co has a direct correlation to K_{IC}. Knee & Plumbridge (1984) reported that the m-value increased with decreasing toughness - also indicating that resistance to fatigue crack propagation increases with increasing toughness.

2.6.2.4 The effect of *R* on crack growth rates

Knee and Plumbridge (1984) found that fatigue growth rates were increased with increasing *R*. They also found that the higher *R*-value the greater was the range of m-values.

2.6.2.5 The existence of a *ΔK* threshold value

Lueth (1981) reported the existence of a *ΔK* threshold value. Knee and Plumbridge (1984) found a microstructure-independent threshold value and showed *R* to have an effect on this threshold value.

2.6.2.6 Interpretation of the high m-values

Almond & Roebuck (1980) reported that cyclic loading causes the failure mode of the binder phase to change from ductile to brittle. They related the occurrence of the low-ductility fracture to the high value of 10 that they obtained for m. Ductile fatigue failure modes give m-values of 2-3. In steels, where fatigue crack propagation occurs by intercrystalline or transgranular cleavage (brittle failure), m-values of 6-7 are obtained. It is therefore to be expected that fatigue crack growth in WC-Co will proceed by a brittle failure mode. This expectation was confirmed by careful fractographic observations.

Knee and Plumbridge (1984) comment that high m-values suggest that in addition to stable fatigue crack propagation, some static (ie fast fracture) events (such as cleavage, microvoid coalescence or transgranular fracture) are taking place. In ductile solids at high values of *ΔK* approaching fast fracture, such static fracture events start to occur in addition to the fatigue crack propagation. These additional static events cause a marked sensitivity of propagation rates to microstructure (Suresh, 1992). This interpretation is upheld by Roebuck & Almond (1988) in their review. They also suggest that the high m-values obtained for WC-Co should be interpreted as crack propagation taking place by a combination of stage 2 and stage 3 fatigue growth mechanisms.

2.6.3 Tensile Fatigue Fracture Surfaces

The following table examines the fatigue fractography results from the tensile fatigue in WC-Co studies:

Table 2.3

Fatigue fractography results

Researchers	**Crack Path**	**Fractography results**
Davies & Barhena **WC-25%Co**	- predominantly in binder phase - some carbide-Co interface cracking - some transgranular cleavage near final fracture region	- no striations - rub markings on mating surfaces - transgranular cleavage exhibited possible river markings - fracture mode was predominantly ductile in the cobalt
Almond & Roebuck **WC-11%Co**	- fatigue crack path is in the binder phase - fatigue crack propagates with little deformation of the binder phase	- fast fracture occurs by ductile rupture of the binder, fatigue occurs by brittle failure of the binder - fatigue fracture surfaces were easily distinguished from fast fracture surfaces by lack of deformation in Co binder - no striations
Lueth **6 - 25% Co**		- no striations or other fatigue induced markings - no difference between fast fracture and fatigue fracture surfaces
Knee & Plumbridge **7.5 - 25% Co**	- Crack advance involves brittle fracture of WC grains ahead of crack tip followed by fracture of Co ligaments - Majority of crack path is between WC and Co and crack will deviate around WC grains to stay at this interface - Favourably oriented WC grains in the path have fractured	- Considerable accumulation of debris on fracture surface (particularly at low *R*) obscures detail of fracture mode in binder - Difference between fatigue and fast-fracture is absence of debris in fast fracture - Fatigue fracture path shows same features as fast fracture path, suggesting fatigue consists of increments of static fracture
Almond & Roebuck **Review**		- binder phase composition could be responsible for the contrasting fractographic observations
Fry & Garrett **6 - 25% Co**	- Path has intergranular fracture with dimples in the binder phase and with transgranular cracking of large carbide grains	- Fast fracture and fatigue indistinguishable
Polák, Obrtlík & Vrbka **WC-9%Co**		- No sharp transition between fatigue and fast fracture surface detected

Schleinkofer, Sockel, Schlund, Görting & Heinrich **WC-6%Co**	- crack path lies predominantly in the binder	- presence of two structures of Co in binder suggest Co phase transformation may play a role in the irreversible microscopic changes ahead of the crack tip - crack paths of growing subcritical cracks lie mainly in the binder - phase transformation from f.c.c. cobalt to h.c.p. cobalt takes place
Schleinkofer, Sockel, Görting & Heinrich	- crack path lies predominantly in the binder	- TEM investigations show that in samples subjected to cyclic loading, a martensitic phase transformation from f.c.c. to h.c.p. structure occurs in the Co ligaments

2.6.3.1 Mechanisms of Fatigue Crack Propagation

Fractographic examinations are carried out in order to obtain information about the mechanism of failure that occurred.

As already mentioned, Almond and Roebuck (1980) suggested that cyclic loading causes the binder failure mode to change from ductile to brittle. This effect could be a result of the fact that the ductile binder, which provides the major contribution to the plasticity of WC-Co, is the minor phase in terms of volume. So any deformation ahead of the crack tip would cause concentrated plasticity in the binder phase leading to work hardening and lower ductility

Lueth (1981), however, states that the fact that fast fracture and fatigue fracture surfaces were seen to be identical suggests that fatigue is not an active mechanism in WC-Co and the stable crack growth consists merely of increments of fast fracture. Knee and Plumbridge (1984) also state that as their fatigue crack path showed the same features as their fast fracture path, fatigue crack propagation proceeds by increments of static fracture. They described the mechanism of fatigue crack propagation as cleavage of WC grains ahead of the crack tip followed by failure of the Co ligaments. Both these studies therefore suggested that there is no 'true' fatigue in WC-Co and that the stable crack propagation observed consists merely of increments of fast fracture.

Fry & Garrett (1988) also reported that fatigue fracture surfaces are indistinguishable from fast fracture surfaces. Further, they reported that the mean stress had a substantial effect on the crack growth rate. This they interpreted as an indication that some 'static' (fast) fracture modes were taking place together with the fatigue process: Fatigue crack propagation rates depend on R and ΔK and are therefore, according to Fry and Garrett (1988), independent of the average applied stress. Fast fracture is entirely dependent on the applied loads, which are related to the average applied stress. The existence of a true fatigue process was, however, indicated by the lack of a frequency effect: If the crack growth consisted only of increments of fast (or static fracture), then crack growth rates would depend on the amount of *time* that the crack was subjected to the applied loads. Increasing frequency causes a decrease in the amount of time that the specimen is subject to the applied loads at each cycle and should therefore cause a decrease in crack growth rates. Further, comparisons of data from monotonic and cyclic crack growth tests confirmed the existence of a true fatigue process in WC-Co.

In their 1996 fatigue studies, Schleinkofer *et al*, (1996) used TEM investigations to show that a phase change from the f.c.c. to the h.c.p. structure occurs in the cobalt ligaments during cyclic loading. This phase change results in embrittlement and subcritical cracking in the Co phase. SEM investigations suggested that the cyclic loading resulted in the crack propagating almost entirely through the cobalt phase.

Table 2.4
Fatigue fracture surfaces vs fast fracture surfaces

Researcher	**Are fatigue fracture surfaces distinguishable from fast fracture surfaces ?**
Davies & Barhana 1972	Some rub marks were found on the fatigue surface - otherwise the same as fast fracture surface
Almond & Roebuck 1979	Yes - fatigue causes brittle failure of the binder as opposed to the ductile failure mode in fast fracture
Lueth 1981	No
Knee & Plumbridge 1984	No
Fry & Garrett 1988	No

2.6.4 Summary of Tensile fatigue results

As has been shown, contradictory results are almost as numerous as the different testing methods. What consensus can be found is that the value of m is higher than that found in steels (usually 6-7). This is generally interpreted as an indication that 'static' (stage 3) crack growth effects are taking place together with the stage 2 stable fatigue crack propagation. Some researchers, however, dispute the existence of a 'true' fatigue effect in WC-Co and state that the stable crack growth witnessed is wholly a result of increments of static crack growth. This area of contention is carried through to contradictory reports of fracture surface appearance.

An area of some consistency is that considerable scatter is obtained in *S-N* data, particularly when unnotched specimens are used. This is entirely in agreement with the notion that fatigue crack initiation times are dependent on flaws in the material.

Although it is generally agreed that microstructure plays a role in fatigue crack growth rates, the exact mechanisms are not understood. It does, however, seem to be generally accepted that increasing grain size brings about greater resistance to fatigue crack propagation. Very few studies have investigated the effects of *R* and microstructure on crack growth rates.

2.7 Finite Element Analysis

2.7.1 Introduction

The finite element method has been used in a number of studies involving WC-Co. The method has also been used to study crack propagation in a variety of other materials. The finite element method itself is well established and is routinely used, both in research establishments and in industry. Although the applications that are presented here use the FE method only for stress/strain or fracture mechanics type analyses, the method is also used in a variety of other analysis types. These include heat transfer, thermal stress analysis, mass diffusion analysis and acoustic analysis (*ABAQUS* Standard Users Manual, 1996).

2.7.2 Finite Element Studies of WC-Co

These can be divided into two categories - the first is the study of fracture in WC-Co, assuming an existing crack and the second is the study of stresses within the microstructure.

2.7.2.1 Facture Analysis of the WC-Co Microstructure using the FE Method

The following table summarises the studies of stresses in the WC-Co microstructure:

Table 2.5
Fracture analysis of WC-Co microstructure

Study	Title	Purpose	FE Mesh	Results
Sigl and Schmauder, 1988	A finite element study of crack growth in WC-Co	FE study of crack growth in WC-Co to study the plastic deformation of binder ligaments	The mesh was built on a micrograph with an arrested crack. Residual thermal stresses were neglected. This model was embedded in a linear elastic zone exhibiting the bulk WC-Co properties.	Plasticity is confined to the ligaments along a narrow band around the expected fracture path. Non-bridging binder regions deform purely elastically
Fischmeister *et al, 1988*	Finite Element Modelling of Crack Propagation in WC-Co Hard Metals	Same study as above	As above	Void formation in the binder can be predicted
Spiegler and Fischmeister, 1992	Prediction of Crack Paths in WC-Co Alloys	Prediction of the path that a crack will take through the WC-Co microstructure	Differently-shaped Co regions were embedded in a bulk WC-Co mesh and the void formation in the differently shaped regions was compared	The critical angle at which a crack enters a cobalt region can be used to predict the preferred site for void nucleation and hence the subsequent crack path

Aoki *et al*, 1996	Finite element fracture analysis of WC-Co alloys	Study was performed to gain detailed understanding of ductile fracture in Co.	Three differently-shaped Co regions were modelled at the tip of a crack embedded in bulk WC-Co	Effects of the shape of the Co region and of the stress state on distributions of hoop stress, hydrostatic stress and microvoid volume were discussed

2.7.2.2 Other Properties of WC-Co Examined using the FE Method

The following table summarises the other FE studies in WC-Co :

Table 2.6
Other properties of WC-Co using the FE method

Study	Title	Purpose	FE Mesh	Results
Jaensson & Sundström, 1972	Determination of Young's Modulus and Poisson's Ratio for WC-Co Alloys by the Finite Element Method	To determine whether the finite element analysis procedure could be applied to the microstructure of a two-phase material for the analysis of elastic properties	Built on an electron micrograph of WC-Co microstructure	-Macroelastic properties of a two-phase material can be analysed using the FE method -Grain boundary cracks between carbide grains have little effect on the overall stiffness of the WC-Co
Sundström, 1973	Elastic-Plastic Behaviour of WC-Co Analysed by Continuum Mechanics	To determine whether the FE method can be used to predict the elastic-plastic behaviour of two-phase materials	Built on an electron micrograph of WC-Co microstructure	FE applied to a two-dimensional model of real microstructures comprising as few as 20 grains gives reasonable agreement with experimental stress-strain curves.
Spiegler *et al* 1992	Finite Element Modelling of the Thermal Residual Stress Distribution in a WC-10wt%Co Alloy	To map the spatial distribution of residual thermal stresses in a realistic WC-Co microstructure.	Built on a micrograph, which was then embedded in bulk WC-Co.	While the mean equivalent stress in the Co phase is below the yield stress, local maxima are well above yield limit. Maxima are found at interfaces and are relaxed by local plastic deformation.

Quinn *et al* 1996	Simulation of Co Binder Failure in WC-Co Hardmetals	To simulate void growth in constrained Co layers using a variety of different parameters	The binder was assumed to contain a periodic array of unit cells, each containing a void. As a result of symmetry, the analysis was confined to one quadrant of a unit cell.	Overall stress state was shown to have a considerable effect on void growth. Void shape was found to have little overall effect on the void behaviour. Relative slip system orientation was shown to be more significant than lattice orientation.

3 Experimental Procedure

3.1 The Material

WC-Co grades T6 and G6 have been tested. Properties of these grades pertinent to this project are given as follows by the supplier (Boart Longyear, 1996):

Table 3.1
WC-Co properties

	T6	G6
Binder weight %	6 % Co	6% Co
Average grain size	1.8 *μm*	2.3 *μm*
Transverse rupture strength, four-point bending	2190 *MPa*	1910 *MPa*
Compressive Strength	4610 *MPa*	4270
Fracture Toughness	12.6 $MPa\sqrt{m}$	13.7 $MPa\sqrt{m}$

The microstructures of the two grades are illustrated in the figures below:

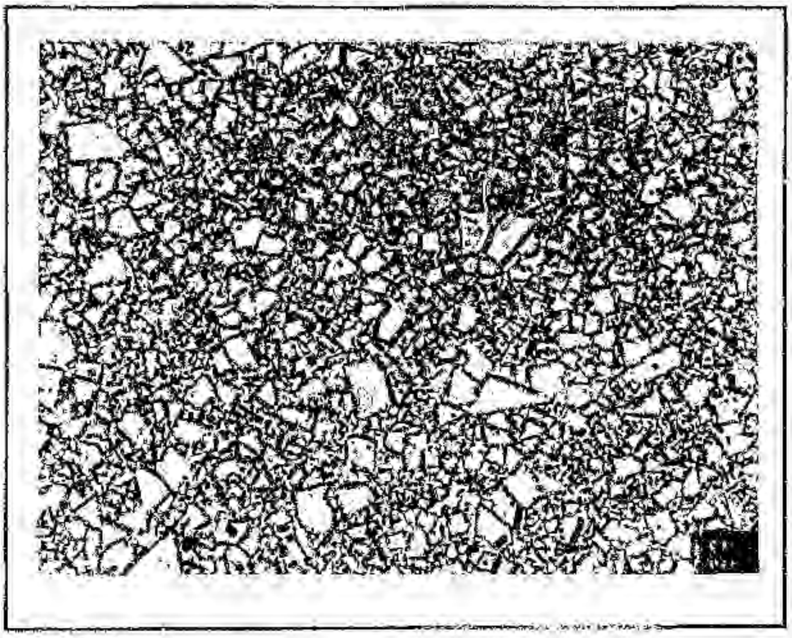

Figure 3.1
The microstructure of grade T6
1500 X magnification

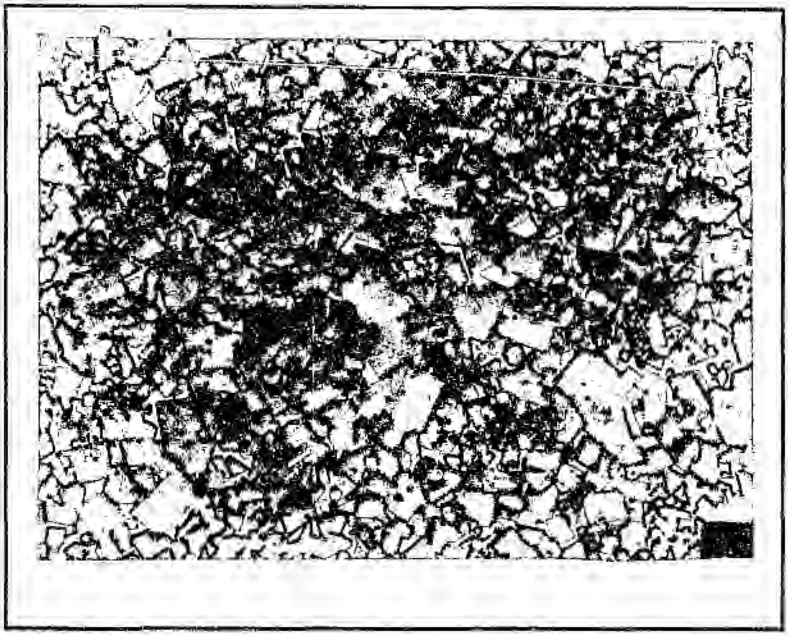

Figure 3.2
The microstructure of G6
1500 X magnification

The individual specimens are identified by their grade followed by a number indicating the order in which the specimen was tested. Hence the first specimen of grade T6 to be tested was called T6.1 and the second T6.2.

3.2 Specimen Geometry

For both, the specimens are shaped as in *figure 3.3*. The dimensions in the figure are, however, specific to grade T6.

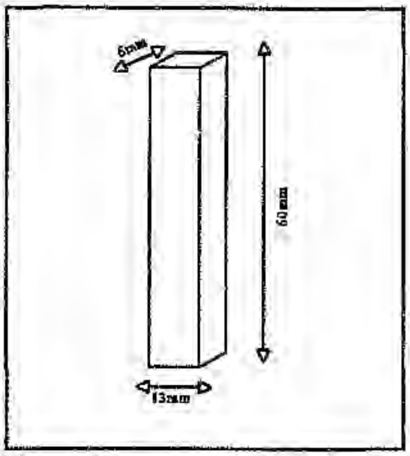

Figure 3.3
T6 Specimen Geometry

The following table gives the specimen dimensions for both grades:

Table 3.2
Specimen dimensions

	T6	G6
Height	60 *mm*	63 *mm*
Width	6 *mm*	7 *mm*
Thickness	13 *mm*	15 *mm*

The single edge notched geometry generally used in compression-compression fatigue testing was chosen. The specimen size was selected to be as close as possible to that used by Suresh & Sylva (1986) and Human (1988). In addition, small specimens were chosen so as to keep the applied loads within the capacities of the available testing machines.

3.3 Specimen Preparation

Specimen preparation for fatigue testing involved two steps:

1. Notching the specimen
2. Precracking the specimen so as to have a sharp crack tip at which to initiate the fatigue crack.

3.3.1 Specimen Notching

The specimens were notched in the centre of their longest side as shown in *figure 3.4*. The notches were cut using a Buehler diamond saw. The notch radius (*r*) is 0.19mm (this value is determined from the width of the wafering blade used to cut the notch). The notch-length to specimen-width ratio varies from 0.1 to 0.2. This ratio is smaller than the 0.3 - 0.4 used by Suresh & Sylva (1986) and the 0.28 - 0.4 ratio used by Human (1988). The reason for using shorter notches is to allow more space for growing the fatigue crack on the small specimens used. All the specimens were notched to approximately 2mm deep.

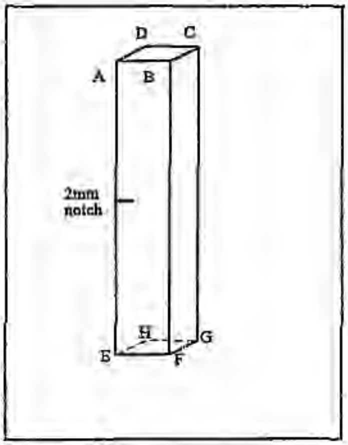

Figure 3.4
Notched Specimen

After notching, the specimens were polished on faces *ABEF* and *DCGH* to facilitate crack growth monitoring.

3.3.2 Precracking

The precracking was done by standing the specimen between parallel platens on a 100 *kN* capacity Amsler Vibraphore.

Figure 3.5, illustrates the loading direction and the stress cycle.

Figure 3.5
The loading of a notched specimen in cyclic compression

A load ratio (*R*) of 10 was chosen to keep testing conditions close to those used by Human (1988) and Suresh & Sylva (1986). The maximum compressive load was chosen so that the maximum stress at the notch root would be the compressive strength of the material. The applied loads were calculated as explained in the next section.

3.3.2.1 Calculation of the stress concentration (*k*) at the root of the notch under axial tension

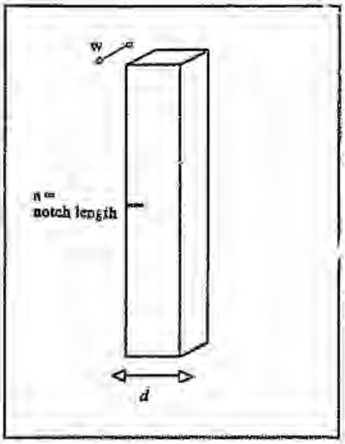

Figure 3.6
Calculation of the stress concentration factor (*k*) at the root of the notch

Using the notation in *figure 3.6* :

a = notch length
d = specimen width
r = notch radius
w = specimen depth

The stress concentration, k, at the root of the notch, is obtained using the following equations:

$$k = k_1 + k_2(\tfrac{a}{d}) + k_3(\tfrac{a}{d})^2 + k_4(\tfrac{a}{d})^3 \qquad \text{----------- (1)}$$

where for $$0.5 \le \tfrac{a}{r} \le 4$$

$$k_1 = 0.721 + 2.394\sqrt{\tfrac{a}{r}} - 0.127\tfrac{a}{r} \qquad \text{----------- (2)}$$

$$k_2 = 1.978 - 11.489\sqrt{\tfrac{a}{r}} + 2.211\tfrac{a}{r} \qquad \text{----------- (3)}$$

$$k_3 = -4.413 + 18.751\sqrt{\tfrac{a}{r}} - 4.596\tfrac{a}{r} \qquad \text{----------- (4)}$$

$$k_4 = 2.714 - 9.655\sqrt{\tfrac{a}{r}} + 2.512\tfrac{a}{r} \qquad \text{----------- (5)}$$

from Roarke & Young, 1975, for the case of tensile loading .

In the specimen geometry used here, $\frac{a}{r} > 4$

Appendix 1 contains a discussion of the inaccuracies this introduces.

3.3.2.2 Calculation of the required loads

k, the stress concentration factor, is the ratio of the applied stress to the nominal stress at the root of the notch. So the stress concentration factor at the base of the notch is:

$$k = \frac{\textit{Stress at the notch root}}{\textit{Nominal stress across specimen waist}} \qquad \text{---------- (6)}$$

By choosing the largest compressive stress at the notch base to be equal to the compressive strength of the material one can calculate the stress to apply. The maximum applied compressive stress, σ_{max}, is therefore calculated by dividing the compressive strength by the stress concentration factor at the notch base. So σ_{max} is calculated from:

$$k = \frac{\textit{compressive strength}}{\sigma_{max}} \qquad \text{---------- (7)}$$

Once σ_{max} has been calculated, the maximum (σ_{min}), mean (σ_{ave}) and amplitude (σ_{amp}) stress values are calculated from the *R* ratio.

These stress values have then to be converted into loads to be applied by the vibraphore.

In standard units:

$$\sigma\ (Pa) = \frac{P\ (N) \times 10^{6}}{\textit{cross-sectional area}\ (m^{2})}$$

3.3.2.3 An example of the precracking load calculations

Using specimen T6.1, where:
a = notch depth = 2mm
r = notch radius = 0.5 * wafering blade thickness = 0.19mm
d = width = 13mm
w = depth = 6mm

One obtains:
k_1 = 7.151 from (2)
k_2 = -12.024 from (3)
k_3 = 8.044 from (4)
k_4 = -2.169 from (5)

And so k = 5.484 from (1).

Then, using (7) to calculate the maximum applied compressive stress:

$$applied\ stress = \frac{compressive\ strength}{k} = -\frac{4610}{5.484} = -840.6\ MPa$$

So, the maximum compressive applied stress, σ_{max} = -840.6 MPa

Now, $$R = \frac{\sigma_{min}}{\sigma_{max}} = 0.1$$

So $$\sigma_{min} = \sigma_{max} \times 0.1 = -840.6 \times 0.1 = -84\ MPa$$

$$\sigma_{ave} = \frac{\sigma_{min} + \sigma_{max}}{2} = \frac{-84 + -840.6}{2} = -462.3\ MPa$$

$$\sigma_{amp} = \sigma_{max} - \sigma_{ave} = \sigma_{ave} - \sigma_{min} = 378.3\ MPa$$

Now the loads have to be calculated from the stresses:

$$\sigma\ (Pa) = \frac{P\ (N)}{d\ (m) \times w\ (m)} = \frac{P\ (N)}{0.013 \times 0.006\ (m^2)}$$

Therefore, using conversion factor Q:

$$1Q = 0.006 \times 0.013 \times 10^6\ Pa = 78N \qquad \text{---------- (8)}$$

Using the conversion factor, *Q*, calculated in equation (8), the following loads are obtained:

$$P_{max} = 0.078 \times (-840.6) = -65.6\ kN$$

$$P_{min} = 0.078 \times (-84) = -6.6\ kN$$

$$P_{ave} = 0.078 \times (-462.3) = 36\ kN$$

$$P_{amp} = 0.078 \times 378.3 = 29.5 kN$$

3.3.2.4 Monitoring the growth of the precrack

The precrack length was monitored by stopping the test and making a replica of the crack. The specimens remained loaded at P_{ave} in the vibraphore while replicas were taken. Replicas were made by dipping cellulose acetate film into acetone and placing the wet film over the notch and crack. The film was then allowed to dry on the specimen. The result was a reverse image of the notch with the crack at its root. The crack length was then measured on either side of the specimen at 100 times magnification. The crack length was taken to be the average of the two measured values.

All the precracks were grown in compression until they arrested. Crack arrest was assumed once the specimen had been subjected to 500 000 loading cycles without any increase in crack length.

Crack growth rate curves were determined for the initial specimens of each grade by measuring the crack length every 250 000 cycles. Once a growth rate curve had been determined for each grade, the curve was used to predict the number of cycles that it would take for the crack to arrest, and on subsequent specimens the test was simply run for this number of cycles. A replica would then be taken of the resulting crack and the specimen would be subjected to a further 500 000 cycles to ensure that the crack had indeed arrested.

The tests were conducted at frequencies between 220 and 230 *Hz*.

3.4 Fatigue Bending Tests

The precracked specimens were then subjected to a four-point bending fatigue test in an ESH servo-hydraulic machine. The four-point bend geometry is illustrated by *figure 3.7*:

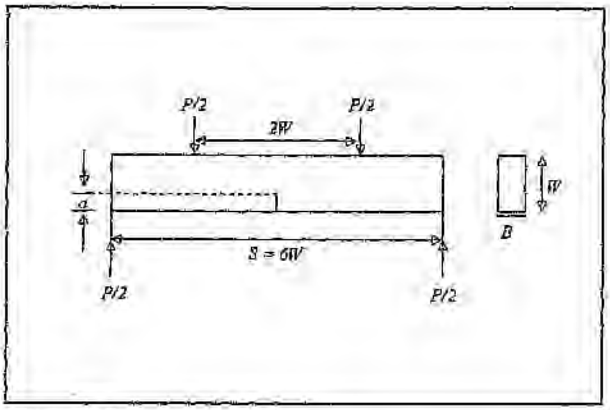

Figure 3.7
Geometry for 4-point bend single edge-notched specimen (SENB4)

Using the notations in *figure 3.7* :

a = sum of notch and precrack length
W = specimen height
B = specimen thickness
S = specimen length
P = applied load

A stress ratio, R, of 20 was used for the four-point bend tests. The procedure outlined by Godse *et al* (1988) was used:

(i) an initially low K-value of 6.5 $MPa\sqrt{m}$ (approximately half the expected K_{IC}) was chosen as K_{max}
(ii) the crack was grown until it arrested
(iii) K_{max} was increased by 0.5 $MPa\sqrt{m}$
(iv) steps (ii) and (iii) were repeated until the crack stopped arresting and a constant or increasing growth rate was obtained
(v) at this stage the test was run at constant loads, and the increasing ΔK (as the crack length increased) values were plotted against measured crack growth rates
(vi) a sinusoidal wave form was used at frequencies of 5 Hz and 20 Hz.

3.4.1 Calculation of Loads for the Four-Point Bend Test

Using the previous notation, Y is a proportionality factor between P and K defined by:

$$Y = \frac{KB\sqrt{W}}{P} \qquad \text{----------- (9)}$$

(The Welding Institute : Tests for Fracture Toughness and Fatigue Assessment)

A simple polynomial approximation to Y for the SENB4 geometry is given by:

$$Y = 11.94(\tfrac{a}{W})^{\frac{1}{2}} - 14.82(\tfrac{a}{W})^{\frac{3}{2}} + 77.82(\tfrac{a}{W})^{\frac{5}{2}} - 139.02(\tfrac{a}{W})^{\frac{7}{2}} + 148.80(\tfrac{a}{W})^{\frac{9}{2}} \qquad \text{---------- (10)}$$

For $0 \le \frac{a}{W} \le 0.6$ and $\frac{S}{W} = 6$ this approximation has an accuracy of ±0.2%

Once Y has been determined using the approximation given in equation (10), the load required to obtain a given K value can be determined using equation (9).

3.4.2 Example of Load Calculations for the Four-Point Bend Test

For the starting loads used on each T6 specimen with :

$K_{max} = 6.5\ MPa\sqrt{m}$ and

a = notch length + precrack length = 2 mm

$B = 6$ mm

$W = 13$ mm

Substituting $\frac{a}{W} = \frac{2}{13} = 0.154$ into equation (10) one obtains $Y = 4.35$

Using $Y = 4.348$ and $K_{max} = 6.5\ MPa\sqrt{m}$ in equation (9) one obtains $P_{max} = 1.02\ kN$

Using $R = \frac{\sigma_{\min}}{\sigma_{\max}} = \frac{P_{\min}}{P_{\max}} = 0.2$ gives $P_{min} = 0.2 \times P_{max} = 0.21\ kN$

$$P_{ave} = \frac{P_{\max} + P_{\min}}{2} = 0.61\ kN$$

$$P_{\max} - P_{ave} = P_{ave} - P_{\min} = 0.41\ kN$$

The ESH Servo-hydraulic machine can be used in different load ranges. In using the machine, however, voltages (V) rather than loads (kN) are specified. The maximum output is 10 V

irrespective of which load range is used. The procedure is, therefore, to select an appropriate load range (based on the loads to be applied) and to convert the loads to the equivalent voltage in that load range. For loads of the magnitudes given above, the 0 - 5 *kN* load range is appropriate. This means that 5 *kN* will be applied to the specimen whenever the voltage is 10 *V*. So to obtain the voltage which should be applied, all the loads are multiplied by two. Hence the following voltages will be applied to obtain the loads calculated above:

$V_{max} = 2 \times P_{max} = 2.05\ V$

$V_{min} = 2 \times P_{min} = 0.41\ V$

$V_{ave} = 2 \times P_{ave} = 1.23\ V$

$V_{amp} = 2 \times P_{amp} = 0.82\ V$

The following table gives a list of the conversion factors used to obtain the voltages from the loads. The required load is multiplied by the conversion factor to obtain the voltage which must be used.

Table 3.3

Load range conversion factors

Load Range	5 *kN*	10 *kN*	20 *kN*	50 *kN*
Conversion factor to *V*	2 *V/kN*	1 *V/kN*	0.5 *V/kN*	0.2 *V/kN*

3.4.3 Monitoring the Crack Growth Rate

The crack length was measured while the cyclic bending test was running with traveling microscopes on either side of the specimen. Crack tip identification was aided by the use of dye-penetrant diluted with acetone, both of which were chosen for their non-corrosive properties. At the lower frequency used (5 *Hz*), the liquid can be seen pulsing in the crack as the crack opens and closes under the cyclic load. Other methods which were attempted for crack measurement were the use of replicas (as in the precracking) and unloading the specimen and checking the crack length at high magnification. The cracks grown in the bending tests are much finer than the cracks grown in the compression precracking and are therefore more difficult to see and measure on replicas. Unloading the crack for measurement has the disadvantage that the crack will not be fully open during measurement and will consequently be more difficult to see. This method was used a couple of times, however, just to check that lengths being recorded through the traveling microscope were realistic. *In situ* observations have the advantage that the crack can be observed while loaded and the test does not have to be stopped (as is necessary for making a replica).

Consecutive crack length measurements allow growth rates to be calculated. In addition, the crack length and the applied loads can be used to calculate ΔK (in a reversal of the process described above for calculating the loads). From these results ΔK can be plotted against the crack growth rate.

3.5 The Finite Element Model

3.5.1 Introduction

This finite element model (FEM) was built on a microstructural level in order to model the precrack initiation. A micrograph of the WC-Co T6 microstructure was selected and the FEM was built directly onto the micrograph. This microstructural model was then built into a macroscale/continuum model of the entire test specimen (as illustrated in *figure 3.8*) in order to model the effect of the precracking farfield applied stresses. The microstructural model was built into the continuum model in such a way that the microstructural region represents the area at the base of the notch - ie the region in which the crack is most likely initiate.

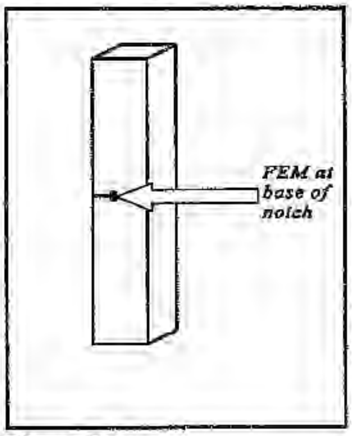

Figure 3.8
Schematic of Microstructural FEM Position

The FEM was built using *ABAQUS* version 5.7. *ABAQUS* is a finite element program that runs in this case on a UNIX platform (*ABAQUS Standard* Users Manual, 1996).

The process of building the FEM can be broken down into two parts, each of which consists of several steps:

Model data definition
This consists of all the data that is used to define the model:
1 Node definition
2 Element definition
3 Contact surface definition
4 Boundary conditions
5 Material Properties
6 Constitutive relationship

History Definition:
This defines what happens to the model:
7 Loading Procedure

Each of these steps is briefly explained below. In each instance the *ABAQUS Standard* Users Manual (*ABAQUS Standard* Users Manual, 1996) is the reference that has been used.

1 Node definition

The nodes or interpolation points are defined first. This is done by assigning a name (or node number) to each interpolation point and then specifying its coordinates. Some of this process is automated within *ABAQUS*.

2 Element definition

The topography/geometry of the model is defined by combining the nodes into elements. In this model the majority of the elements used are rectangular with eight nodes specified to define the boundary as follows :

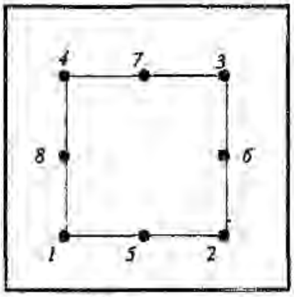

Figure 3.9
Four-sided, eight-node element

In some places, the geometry of the microstructure necessitates the use of triangular elements which are defined by six nodes:

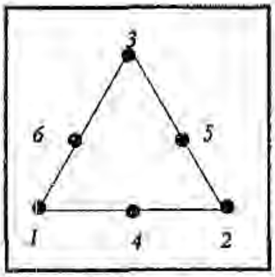

Figure 3.10
Three-sided, six-node element

The boundaries of the elements fit together to define the topography/geometry of the model.

3 Contact surface definition

Most of the carbide-cobalt (WC-Co) and carbide-carbide (WC-WC) interfaces in the model are simply defined by a common node shared between neighbouring elements. This was done so as to create the interfaces without allowing sliding or friction between the WC and the Co or between the carbide grains. But in some cases, where the geometry of the model prevents nodes in neighbouring elements from coinciding, the WC-Co interfaces in the model are defined by means of 'contact surfaces'. Each side of the contact surface interface is defined as a surface and the contact between the surfaces is then defined by tying the surfaces together.

4 Boundary conditions

Finally, the movement of the mesh is limited by defining boundaries on two sides of the model. Movement along the bottom boundary of the model is limited to the x-direction and movement along the right side of the model is limited to the y-direction. This is done so as to prevent free body translation.

5 Material Properties

Each element was given material properties which define its behaviour. The properties used in this FEM are : Young's Modulus, Poisson's ratio and the thermal expansion coefficient of the material. Plastic properties are defined for the cobalt matrix.

6 Constitutive relationship

The constitutive relationship is a mathematical model used to define stress-strain behaviour. In this case, the Gurson model (Gurson, 1977) is used to model void nucleation and growth in the cobalt.

7 Loading

Finally the loading conditions, consisting of physical loads and temperature changes, are applied to the model.

3.5.2 Selecting the Micrograph

The micrograph was taken using a scanning electron microscope (SEM) at 3000 times magnification. The specimen was prepared for the SEM by polishing and etching so as to highlight the two different phases. The specimen was etched in Murakami's solution (10*g* $K_3Fe(CN)_4$, 10*g* NaOH, 100*ml* H_2O) for 120 seconds (ASM Handbook, Etching). The total size of the region that the model is built on is approximately 15 μm x 15 μm.

The region of the microstructure chosen for the micrograph was selected to be as representative of the general microstructure of the material as possible. Once the micrograph had been selected it was scanned into a computer so that the model could be built directly on it.

3.5.3 Defining the mesh

3.5.3.1 The Microstructural Mesh

This part of the mesh was defined using a 'divide-and-conquer' approach of breaking the microstructure into its WC grains and Co regions and defining the mesh for each of these regions. Some complex WC grains and Co regions had to be broken further into several smaller regions, once again to simplify the process of mesh building.

The coordinates of each region were determined using a program called *MapEdit*. *MapEdit* is usually used for designing maps/images for the World Wide Web (so it is, in fact, an HTML editor). Using *MapEdit*, the WWW programmer connects regions/points on an image to specific WWW site addresses. For example, a tourism board may use *MapEdit* to design a map where the user can obtain more information about a specific region by clicking the mouse on that region of the map.

MapEdit works by writing a text file which contains the coordinates of each region of the image and links the coordinates with information such as the name of the region, or the address that anyone selecting the region should be taken to. For the FEM, the "name" of each region was stored together with its coordinates.

In order to automate what would otherwise have been an extremely tedious process, a C program was written to convert the output of *MapEdit* (ie the regions and their coordinates) into the input file for the finite element program, *ABAQUS*.

The program reads the coordinates from the *MapEdit* file and creates a node at each coordinate. It then defines nodes between the coordinates and finally defines the elements that link all those nodes. Any small errors in the input file were corrected directly in *ABAQUS*.

Once the corrected structure was set-up in *ABAQUS*, contact surfaces were defined where the mesh does not match. The contact surfaces were tied together in a manner that prevents the surfaces from moving relative to each other.

The following figures show the mesh which was placed on the microstructure. WC grains are green, and Co regions are red. The gray region is the base of the notch where the microstructural model has been placed and the blue region is the bulk material surrounding the microstructure.

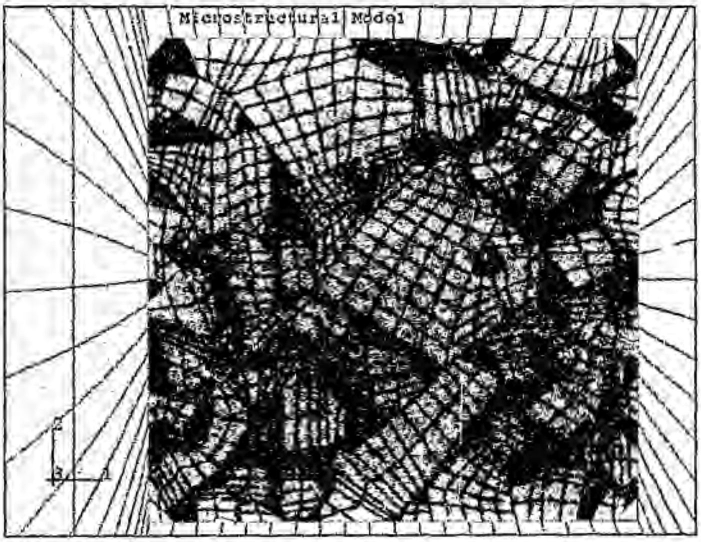

Figure 3.11
Finite Element Mesh

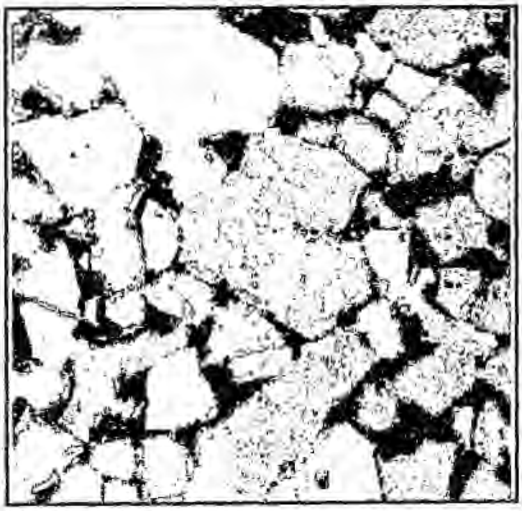

Figure 3.12
Micrograph of FEM region

3.5.3.2 The Continuum Mesh

The continuum model was built around the microstructural model so as to allow the application of the compressive stresses. The rectangular elements used in the continuum model were given the bulk properties of WC-Co. The microstructural model was tied to the continuum model using tied contact surfaces. *Figure 3.13* shows the continuum model. The black region represents the notch.

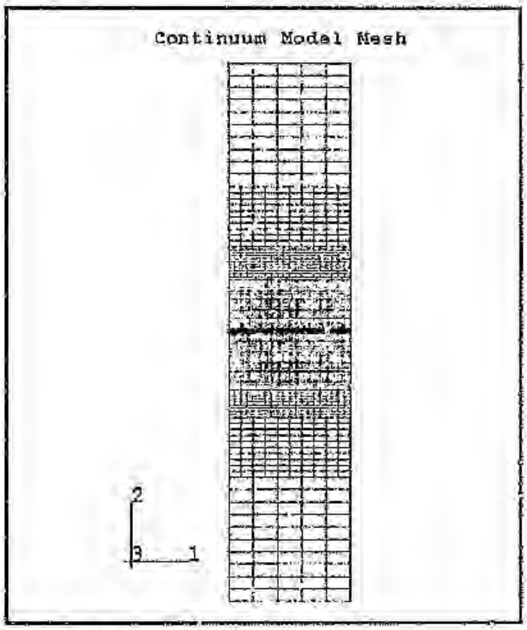

Figure 3.13
The Continuum Model

Figure 3.14 shows the detail of the notch, with the microstructural model at the root of the notch.

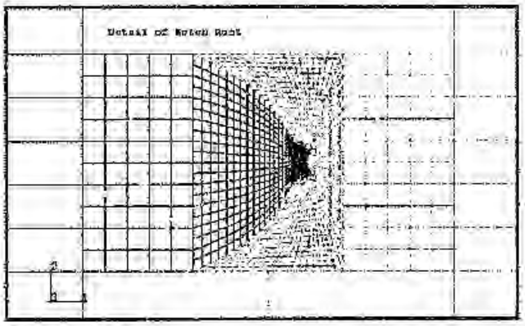

Figure 3.14
Mesh Detail

3.5.3.3 Stress State Model

In addition to the microstructural model embedded in the continuum model, a further continuum model was built without the microstructural region. This model was built to investigate the stress state at the base of the notch without microstructural effects. In this model, the microstructure was replaced with bulk WC-Co elements, as shown in *figure 3.15*.

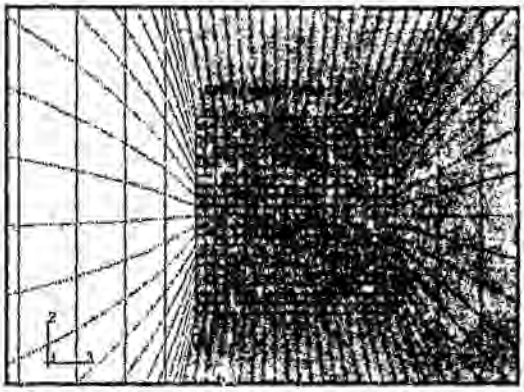

Figure 3.15
The Stress State Model

This model was then subjected to the same loading conditions as the model with the microstructural region.

Both the stress state model and the model with the microstructural region are built in plane strain, which implies that there is no displacement out of the plane of the model. So the finite element model is purely two-dimensional, consisting only of a thin slice of the WC-Co test specimen. This means that the model can only be regarded as a guide to the physics of the problem, rather than a precise numerical representation.

3.5.4 Property and Procedure Definition

3.5.4.1 Materials Properties

The following properties were used to define the material:

Table 3.4
Materials properties used in the FEM

	WC	Co	WC-Co
Young's Modulus *(MPa)*	707×10^3 [1]	211×10^3 [1]	625×10^3 [2]
Poisson's ratio	0.194 [1]	0.31 [1]	0.21 [2]
Coefficient of Thermal Expansion (K^{-1})	5.8×10^{-6} [3]	12×10^{-6} [3]	5.2×10^{-6} [2]
Yield Strength *(MPa)*	n/a	500 [4]	n/a

[1] Fischmeister *et al*, 1988
[2] Boart Longyear, 1996
[3] Spiegler *et al*, 1992
[4] Aoki *et al*, 1996

The WC and the bulk WC-Co were treated as being purely elastic. The yield stress, σ, of the constrained Co was determined from the following equation::

$$\sigma = \sigma_0 + (\sigma_S - \sigma_0)\ [1 - \exp\ (-\frac{\varepsilon_{pl}}{\varepsilon^*})] + k_y L^{-\frac{1}{2}}$$

(Poech *et al*, 1991)
where

L is the mean linear intercept of the binder
$k_y = 7\ Nm^{-1/2}$ is the Hall-Petch coefficient which accounts for the limited slip due to the constrained binder
σ_0 = yield stress of unconstrained Co
σ_S = 970 MPa = a plastic flow parameter
$\varepsilon^* = 0.06$
ε_{pl} = plastic strain

3.5.4.2 Constitutive Relationship

The elastic behaviour of the materials is described using Young's Modulus and Poisson's ratio. The constitutive model used for the plastic failure of the cobalt phase is the Gurson model (Gurson, 1977), which describes the failure of a ductile metal by the nucleation and growth of voids.

In the statement of the Gurson model below, the triaxial stress state has been broken down into two components: a hydrostatic component and a deviatoric component. The hydrostatic component, p, is defined as follows:

$$p = \frac{1}{3}(\sigma : I)$$

and the deviatoric component, S, is defined as :

$$S = \sigma + pI$$

where σ is the macroscopic stress tensor and **I** is the unit matrix.

The Gurson constitutive model for a material with a small volume fraction of voids is stated as follows:

$$\Phi = \left(\frac{q}{\sigma_y}\right)^2 + 2q_1 f \cosh\left(-\frac{3}{2}\frac{q_2 p}{\sigma_y}\right) - (1 + q_3 f^2) = 0$$

Where :

$q = \sqrt{\frac{3}{2}(S : S)}$ is the Mises stress

p is the hydrostatic pressure
f is the volume fraction of the voids
σ_y is the yield stress of the fully dense material
q_1, q_2 and q_3 are parameters introduced by Tvergaard (Tvergaard,1981) with the following recommended values:
$q_1 = 1.25$
$q_2 = 1$
$q_3 = q_1$
$q_1 = q_2 = q_3 = 1$ gives the original Gurson equation.
S is defined above

The model gives reasonable results for material with less than 10% voids - ie for $f < 0.1$

In this model, the change in void volume fraction, is given as:

$$\dot{f} = \dot{f}_{gr} + \dot{f}_{nucl}$$

where

$\dot{f}_{gr}$ is the rate at which the void volume fraction changes due to void growth

and

$\dot{f}_{nucl}$ is the rate at which the void volume fraction changes due to void nucleation.

These are discussed in greater detail in *Appendix 2.*

3.5.4.3 Loading Procedure

The following initial conditions are applied to the specimen:

Temperature	1200 ℃
Pressure	50 *Bar*
Relative Density	1

These are the conditions which the specimen is subjected to during the sinter HIP step in the manufacturing operation.

The loading procedure has then been broken into four steps:

Step 1:

Temperature : Eutectic temperature lowered to room temperature

Load applied : 50 *bar* decreased to atmospheric pressure

Step 1 simulates the cooling of the specimen from the sinter HIP process.

Step 2:

Temperature : room temperature

Load applied : none

The nodes and elements which make up the specimen notch are removed from the model. So the cutting of the notch is simulated in this step. None of the compressive stresses that may be introduced into the material as a result of cutting the notch are explicitly included in the model.

Step 3:

Temperature: room temperature

Load applied : the maximum precracking load (σ_{max}) is applied to the specimen top and bottom

The first load cycle maximum load is simulated in this step.

Step 4:

Temperature : room temperature

Load applied : the precracking load is removed from the specimen.

3.6 Verification of the FEM Results

In order to ensure that the FEM model accurately represents the precracking process, the FEM results were compared to other researcher's results. The thermal residual stresses predicted by step 1 of the FEM model were compared with the results of neutron diffraction studies (eg Krawitz *et al*, 1988).

Experimental results are not so readily available, however, for the stresses generated in steps 3 and 4. In order to verify these results, a single-load test was performed on a prepared T6 specimen. The specimen was then examined in the SEM so as to compare the magnitude and sites of damage on the specimen with the areas of high tensile stress predicted by the model.

4 Results and Discussion

This chapter presents results from the precracking and fatigue experiments as well as the results from fractography, stress analysis and verification of the stress analysis.

4.1 Precrack Results

4.1.1 Precrack Growth Rates

The precracking tests on T6 samples were conducted at approximately the loads calculated in the previous chapter, *section 3.3.2.3*, ie:

$$P_{\max} = -65.6\ kN$$

$$P_{\min} = -6.6\ kN$$

$$P_{ave} = -36\ kN$$

$$P_{amp} = 29.5kN$$

The precracking tests on G6 samples were carried out at higher loads, due to the larger cross-sectional area of the specimens. The precracking loads for the G6 samples were calculated using the same method as was used for the precracking loads for the T6 samples and were the following:

$$P_{\max} = -78\ kN$$

$$P_{\min} = -7.8\ kN$$

$$P_{ave} = -42.9\ kN$$

$$P_{amp} = 35.1\ kN$$

Figure 4.1 shows the crack length versus the number of cycles for grade T6:

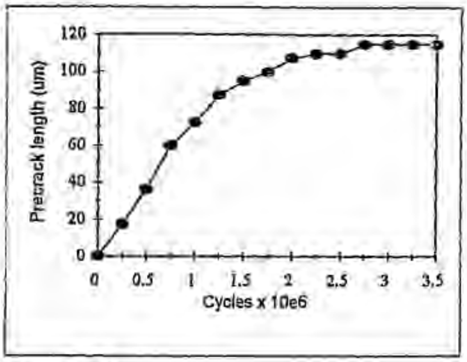

Figure 4.1
Average the crack length versus the number of cycles for Grade T6

Figure 4.1 is the crack length versus the number of cycles curve for specimens T6.2 and T6.3.

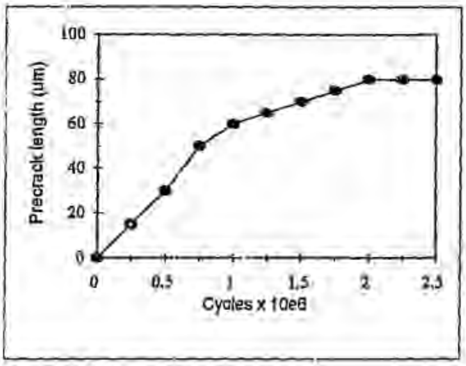

Figure 4.2
Crack length versus the number of cycles Curve for Grade G6

Figure 4.2 shows the crack length versus the number of cycles curve for grade G6, determined on specimen G6.2.

Both the above curves are typical curves as reported in the literature, where the crack grows at a decreasing rate until it arrests. Suresh *et al* (1986) have shown that as the crack grows longer, the fraction of the loading cycle for which the crack is open decreases. Crack growth deceleration and arrest have been attributed to this crack closure effect combined with the residual compressive stresses ahead of the crack (Suresh, 1991).

4.1.2 Final Precrack Lengths

The following table lists the final length of each precrack and the number of cycles it was subjected to.

Table 4.1
Final Precrack Lengths

Specimen	**Final Precrack Length (μm)**	**Total number of cycles**
T6.2	110	3.25×10^6
T6.3	120	2.5×10^6
T6.4	530	7.25×10^6
T6.5	3390	4×10^6
T6.6	140	4.5×10^6
T6.7	130	4×10^6
T6.8	285	6×10^6
T6.9	195	6×10^6
T6.10	480	6×10^6
G6.2	80	2.5×10^6
G6.3	220	6.5×10^6

Table
Summary of final precrack lengths

T6.1 and G6.1 specimens were notched with a new blade which had not yet been worn down to a rounded shape. The result was 'square' notches. When the T6 'square' notch was subjected to cyclic compression, a crack grew off each corner as can be seem in *figure 4.3*.

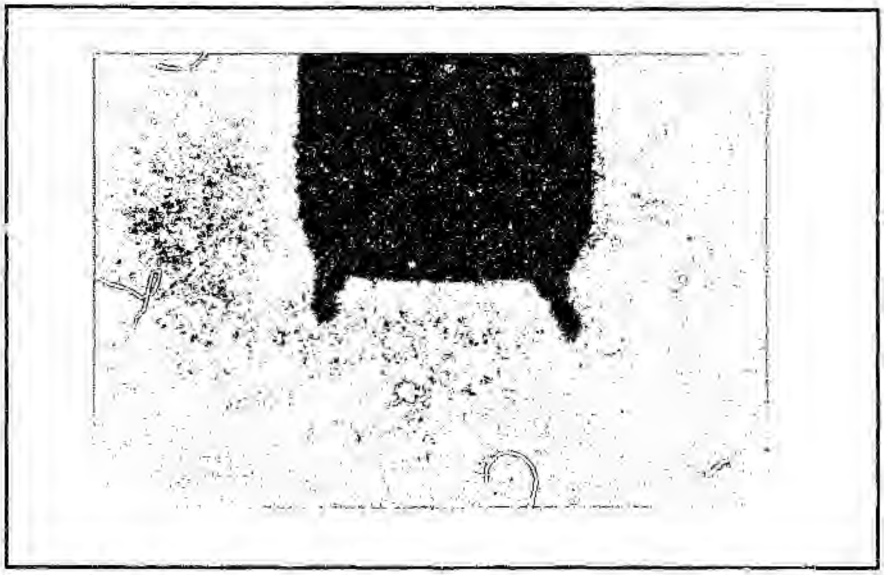

Figure 4.3
Fatigue cracks growing off the corners of a square notch
100X Magnification

Specimen T6.5 developed a 6mm-long fatigue crack on one side, while the on other side it developed a 'typical' compression fatigue crack. The start of the 6mm fatigue crack can be seen in *figure 4.4*. Whereas all the other compression fatigue cracks had a wide, blunt appearance, the crack grown on specimen T6.5 is long and narrow. Both the appearance and length of this crack suggest that it grew in tension. Subsequent measurement of the specimen with a Vernier calliper showed that the ends were not parallel. The two arrows in *figure 4.5* show where the far corner of the specimen was almost 0.1 mm longer than the near corner. This would have resulted in the load being placed on the far corner as shown in the *figure 4.5*. This load application would cause a bending moment at the notch causing a tensile stress there. The tensile fatigue crack in *figure 4.4* resulted. *Figure 4.6* shows a typical precrack for comparison.

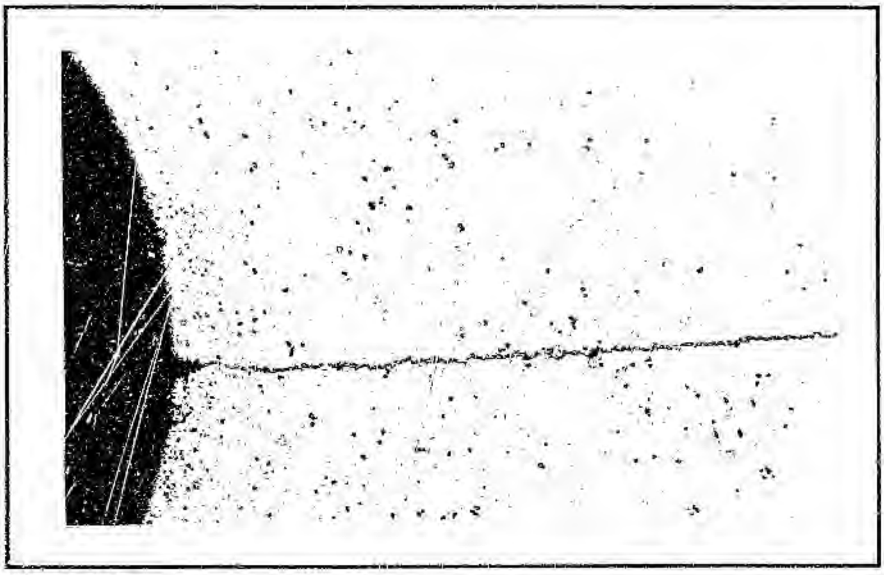

Figure 4.4
Tensile fatigue crack grown on specimen T6.5
400X Magnification

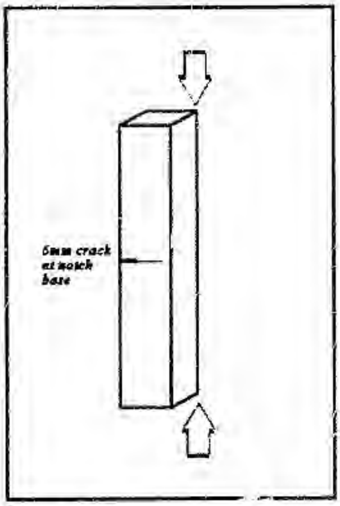

Figure 4.5
Tensile fatigue crack on compression loading

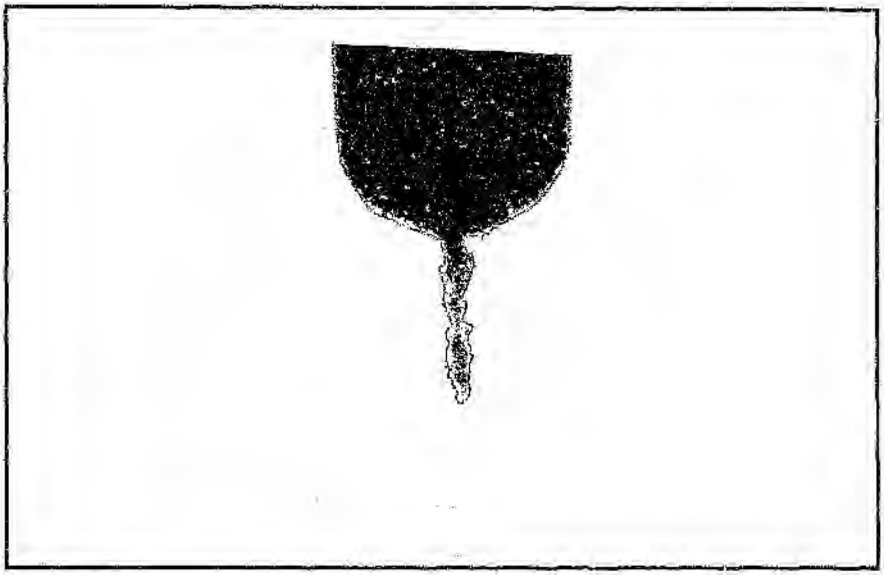

Figure 4.6
Typical precrack from a round notch
100X Magnification

None of the precrack lengths were the same on both sides of the specimen. This uneven cracking would have resulted from the base of the notch not being 'centred' in the specimen. In specimen T6.3, for example, the crack shown in *figure 4.7* is 160 *μm* long, while the other side of the crack shown in *figure 4.8* is 80 *μm* long.

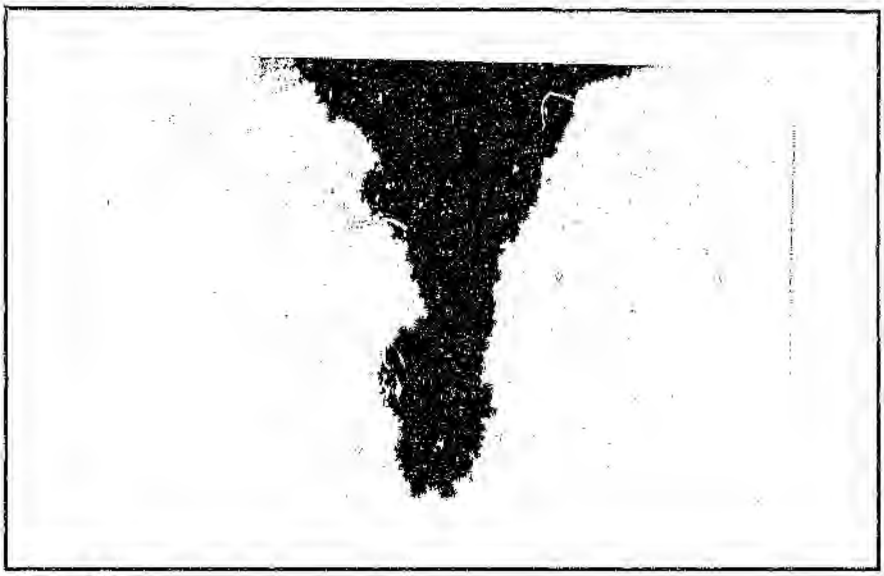

Figure 4.7
Longer side of precrack on specimen T6.3
400X Magnification

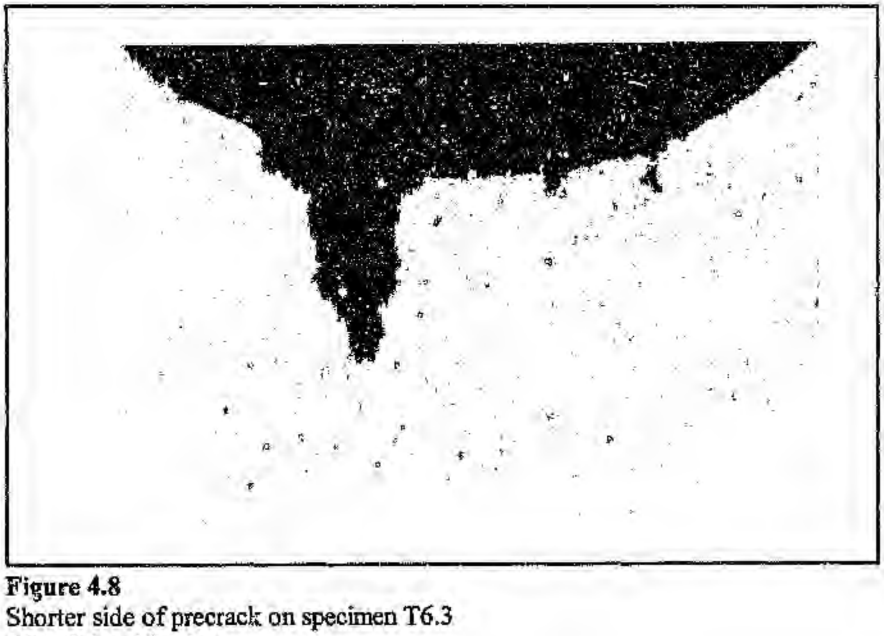

Figure 4.8
Shorter side of precrack on specimen T6.3
400X Magnification

Figure 4.9 is a plot of the final precrack lengths in specimens T6 against the number of cycles which the test specimen was subjected to. T6.1 and T6.5 are not included in the plot due to the reasons discussed above.

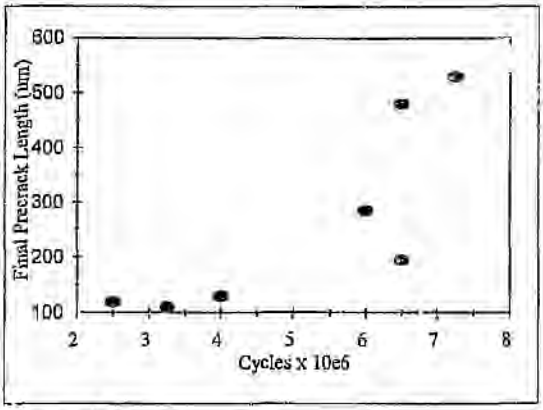

Figure 4.9
Final Crack Length vs Number of Cycles in specimens T6

The above curve suggests that there is a relationship between the number of cycles and the final precrack length. This is contrary to the growth rate curves generated both in this project and by other researchers, which show that the crack arrests after a certain number of cycles and so there should be no relationship between final crack length and number of cycles (once the crack has arrested). This is discussed in detail at page 74. All the final lengths in the above graph were determined once the crack had not grown for 500 000 cycles, ie the cracks had arrested.

4.1.3 Morphology of Compression Fatigue Cracks

Figure 4.10 shows another general morphology of the precrack produced by compression-compression fatigue, viewed on an optical microscope. The precrack is wide and blunt, with some smaller cracks at the crack tip that are only visible at higher magnification (*figure 4.13*). *Figures 4.11* and *4.12* , taken on the SEM, show this in detail. *Figure 4.13* shows the crack tip. There are small, "sharp" cracks ahead of the main crack tip and there is also considerable crack branching, as manifested by the missing fragments.

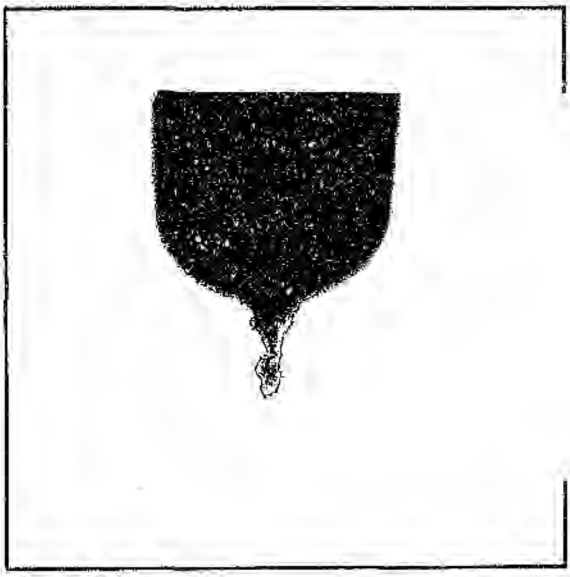

Figure 4.10
Precrack Morphology
Grade F6
400X Magnification

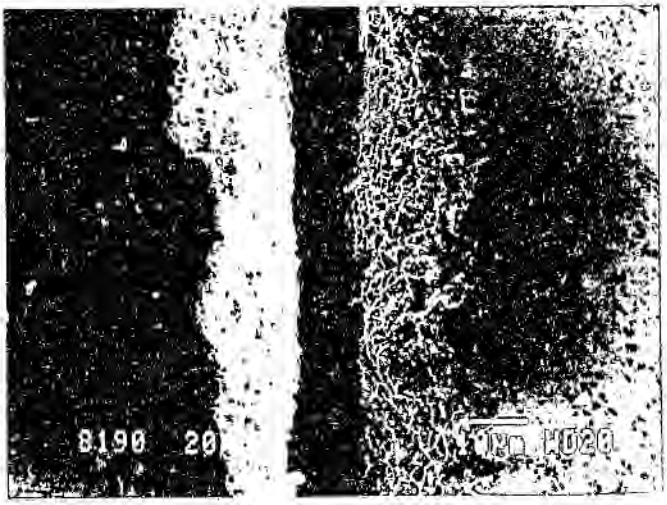

Figure 4.11
Detail of Precrack Outcrop
Grade T6

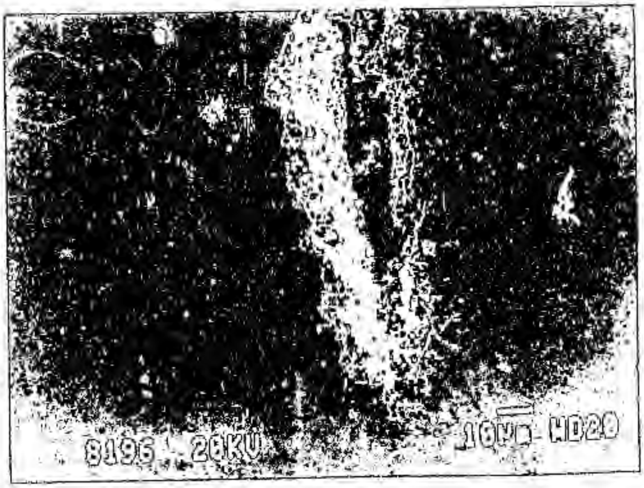

Figure 4.12
Detail of Precrack Tip
Grade T6

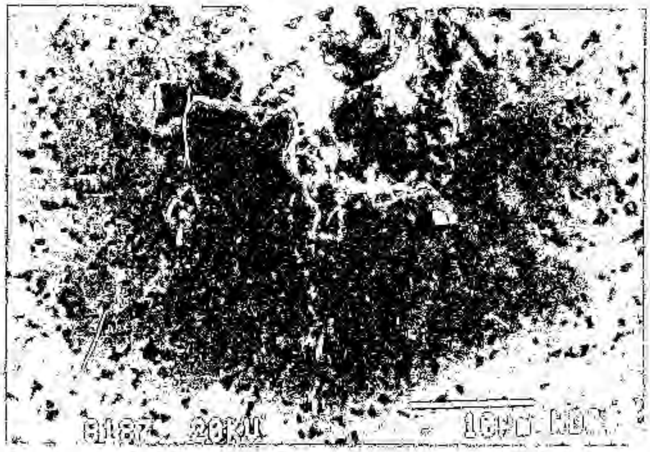

Figure 4.13
Precrack tip detail
Grade T6

The material below the notch tip has fine cracks on either side as a result of the extensive crack tip branching.

Figure 4.14 shows a region of the compression fatigue crack. On the right, there is an area from which a piece of the material has fallen off. On the left, there is a region encircled by fine cracks where it looks as if another piece of material is about to fall off.

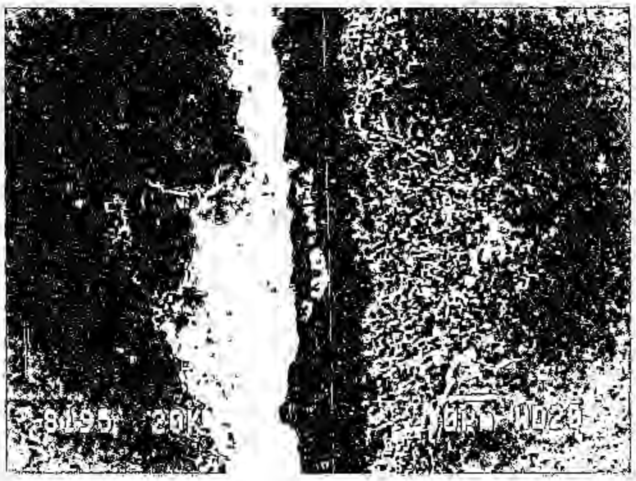

Figure 4.14
Precrack Crack Branching
Grade T6

Figures 4.13 and 4.14 show that fine cracks form, both in front and on the side of the precrack, with considerable crack branching. Areas of the material become surrounded by these fine cracks and eventually fall out of the specimen altogether, thus increasing the area of the main precrack.

Figure 4.9 shows that there is a relationship between the final precrack length and the number of cycles that the test is run for. *Figures 4.1* and *4.2*, however, show that the precrack decelerates and arrests. The fact that the precrack arrests means that any subsequent cycles should not cause any further growth, so *figures 4.1* and *4.2* imply that there should be no relationship between number of cycles and final precrack length. A number of researchers have reported growth rate curves similar to those in *figures 4.1* and *4.2*. Their results are summarised in below:

Table 4.2
Precracking growth rate results from the literature

Researchers	Year	Material	No cycles at which the crack arrested	No cycles test run for	Intervals precrack measured at	Frequency test conducted at
Reid *et al*	1979	Mild steel	$\pm 5 \times 10^5$	8×10^5	1×10^5	25 *Hz*
Suresh	1985	Steel	$\pm 1{,}1 \times 10^5$	$1{,}4 \times 10^5$	0.2×10^5	50 *Hz*
Suresh & Sylva	1986	WC-Co	$\pm 3 \times 10^5$	4×10^5		4 *Hz*
Ewart & Suresh	1986	Polycrystalline alumina	$\pm 2 \times 10^5$	4×10^5	0.2×10^5	20 *Hz*
Figures 4.1 and *4.2*	1998	WC-Co	$\pm 30 \times 10^5$	40×10^5	25×10^5	± 230 *Hz*

Clearly, *figure 4.9* contradicts these results by showing that the precrack continues growing (which it must do if there is a relationship between the final precrack length and number of cycles). A possible mechanism of fatigue compression crack growth based on the present experimental results is presented here in order to explain this discrepancy.

As was shown in *figures 4.10*, *4.12* and *4.13*, there are always sharp cracks ahead of the main body of the precrack. This fact, coupled with observations of the crack replicas taken during testing, suggest that initially the crack consists entirely of sharp, branching cracks at the notch tip, as illustrated schematically below:

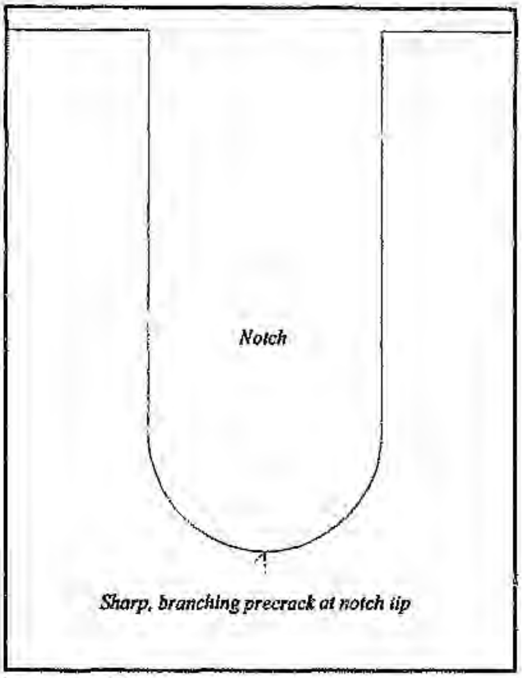

Figure 4.15
Initial Precrack Appearance

As shown in *figures 4.13* and *4.14*, the sharp, branching cracks propagate during subsequent compression cycles and cause 'chunks' of material to fall out of the specimen entirely. This is represented schematically in *figure 4.16*, where the material at the tip of the notch in *figure 4.15* has fallen out of the specimen. This in effect increases the length of the notch, by forming a new notch, with a smaller radius than the original notch, at the tip of the original notch.

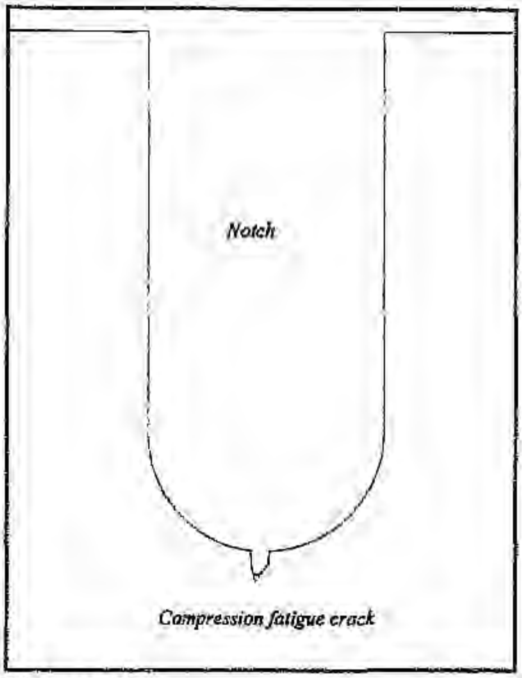

Figure 4.16
A 'Chunk' of Material is dislodged at the Notch Tip

Once loads are applied to the 'new notch', new near-tip residual stresses will result. New, fine, branching cracks will form at the base of the new notch as a result of the new region of residual stresses, and so the entire process will recur. The next step, once again consisting of dislodging material and forming new, sharp, cracks is schematically illustrated in *figure 4.17*.

In all the precrack growth rate research reported above, precrack arrest was generally assumed after less than 3 x 10^5 cycles (or in the case of *figures 4.1* and *4.2*, after 5 x 10^5 cycles). In all the studies quoted in *table 4.1*, the tests were run for less than a million cycles at low frequencies. In addition, the fine cracks ahead of the precrack tip shown in *figure 4.13* are scarcely visible using an optical microscope and therefore cannot be measured on a replica viewed through an optical microscope. So the precrack arrest that is reported is probably a slow, undetected growth of the fine, 'sharp' cracks ahead of the precrack. So although crack closure and residual compressive stresses (Suresh, 1991) may cause the crack growth to decelerate, it seems that the notch growth (caused by material being dislodged) is the dominant mechanism.

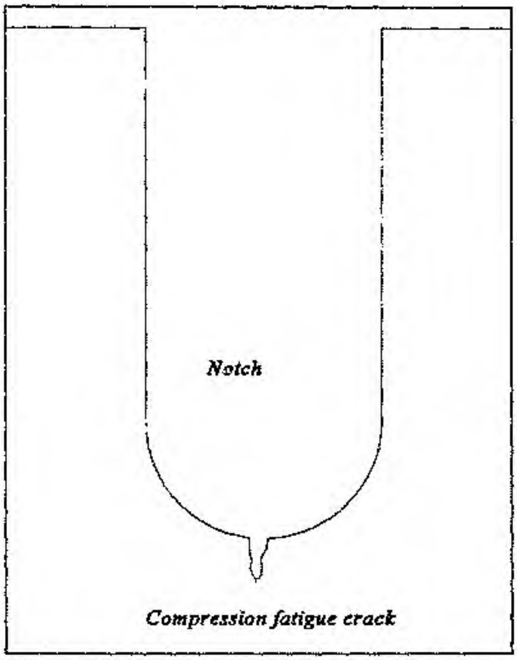

Figure 4.17
Precrack Schematic

4.2 Four-Point Bending Fatigue Test Results

The following growth rate curves were obtained for grade T6 and G6. Each curve was determined from a single specimen.

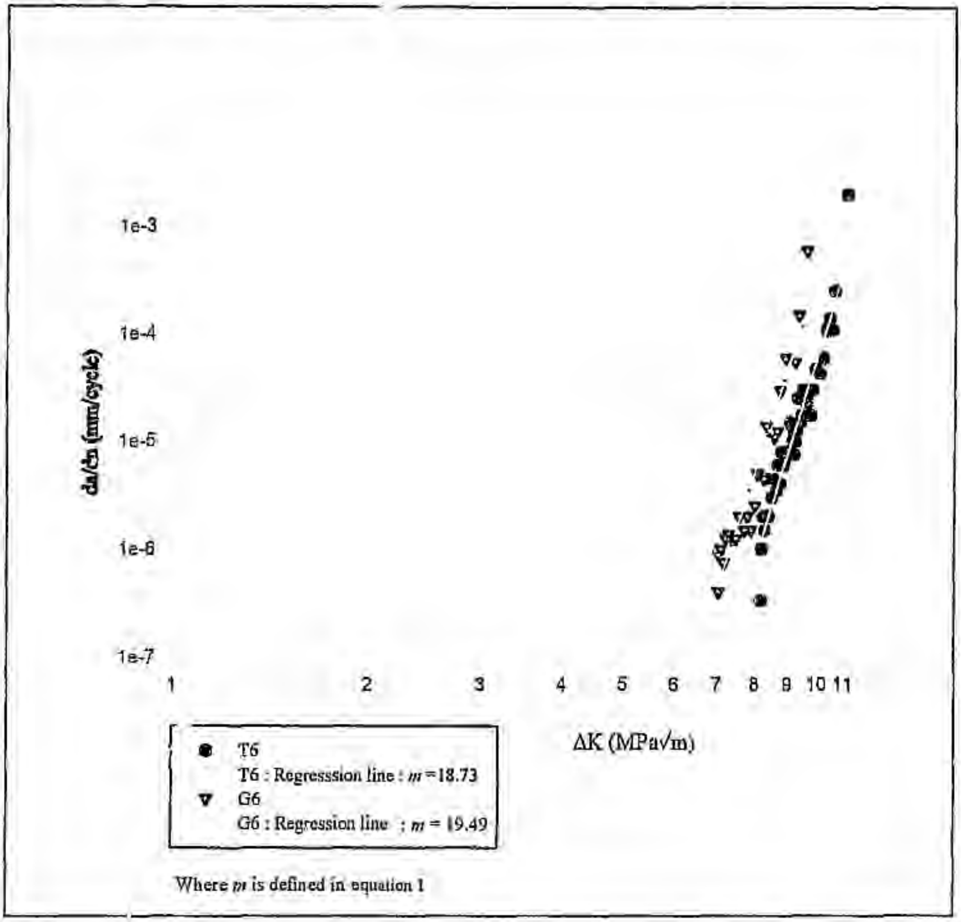

Figure 18
Fatigue Growth Rate Curves for grades T6 and G6

In each case, the data was fitted to the Paris equation:

$$\frac{da}{dn}=C(\Delta K)^m$$ ------------------ [1]

As discussed in *section 2.6.2*, the larger m-value of the Paris equation, the greater the rate at which the growth rate of the fatigue crack increases and therefore the lower the resistance to fatigue crack propagation. The above curves show a lower m-value (and hence a better resistance to fatigue crack propagation) for T6 than G6. The literature is consistent in reporting that m decreases with increasing grain size (Knee & Plumridge, 1984; Johansen *et al* 1970; Fry & Garrett, 1988). Further, the literature indicates a positive correlation between toughness and resistance to fatigue crack propagation. T6 has a smaller average grain size (reported as 1.8 μm, Boart Longyear, 1996) and a lower fracture toughness (reported as 12.6 $MPa\sqrt{m}$, Boart Longyear, 1996) than G6 (2.3 μm and 13.7 $MPa\sqrt{m}$, Boart Longyear, 1996). So T6 should have the larger m-value (ie, the lower fatigue resistance), but this not the case in the results presented here.

The regression coefficient for the T6 regression line is 0.9164 and for the G6 regression line is 0.9252. So, the m-values can be quoted as follows:

$m_{T6} = 18.73 \pm 0.78$

$m_{G6} = 19.49 \pm 0.73$

So, in fact, the two m-values are statistically the same and the discrepancy reported above can be attributed to experimental scatter. This would suggest that the method used here is not sensitive enough to discriminated between grades with very close properties.

The m-values obtained here are, however, consistent with the m-values in the literature that listed in *table 2.2.*

4.3 Fractography

The fracture surfaces of the samples tested as described in *sections* 3.3 and 3.4 were examined using a scanning electron microscope (SEM). *Figure 4.19* is a schematic showing how fracture progresses once it initiates from the notch. The notch was approximately 2*mm* long. The precrack, which initiated at the base of the notch, varied in length across the breadth of the specimen, with lengths ranging from about 30μm to 200μm. The lengths presented in Table 4.1 are averages of the crack length measured on the surface at either side of the specimens. Such variations in the length of the precrack were observed both between specimens, and within the same specimen. Different types of fracture surfaces were observed in the precrack region. The fatigue region, which resulted from the four-point bend fatigue tests, was generally a few millimetres long - depending on how long the fatigue crack grew before K reached the critical K_{IC} value and fast fracture occurred. The rest of the fracture surface resulted from the final fast fracture of the specimen.

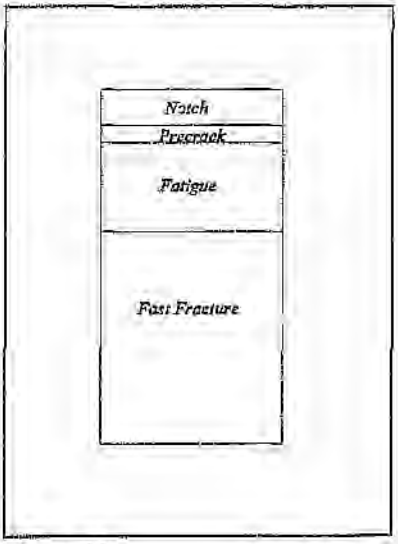

Figure 19
Schematic of Fracture Surface
Not to scale

As the precrack and fatigue fracture surfaces will be compared with the fast fracture surface, the results of fractography on the fast fracture surface will be presented first. As the fracture surfaces occurring in grades T6 and G6 are the same in all salient features, the fractography results for these two grades will be presented together.

4.3.1 Fast Fracture

Figure 4.20 shows the fast fracture surface of a T6 specimen and *figure 4.21* shows the fast fracture surface of a G6 specimen. In both, the angular shaped grains are the carbide grains, and the cobalt ridges occur as lighter areas on the carbide grains. At higher magnification, with T6 in *figure 4.22* and G6 in *figure 4.23* , the cobalt ridges are visible in greater detail on and between the carbide grains. In all the fast fracture micrographs, the cobalt ridges are clearly defined.

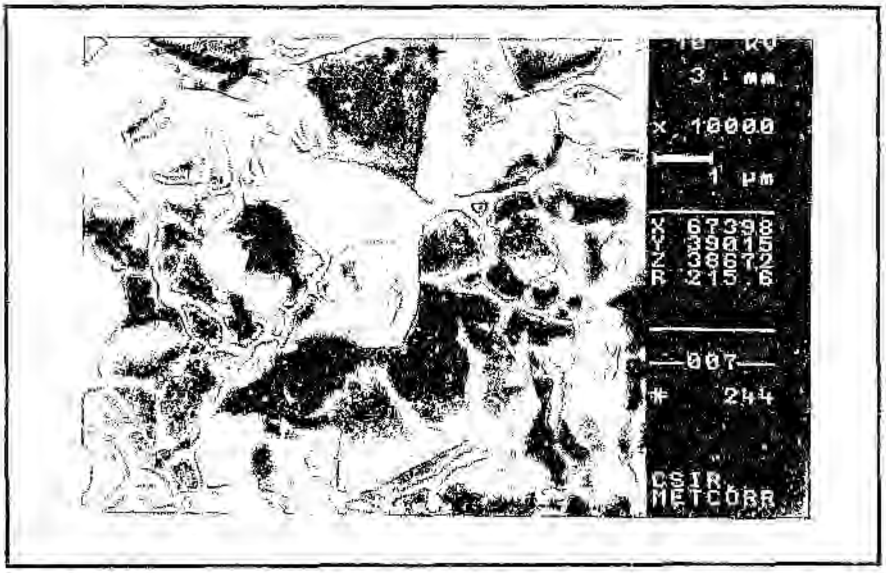

Figure 4.20
Fast Fracture
Grade T6

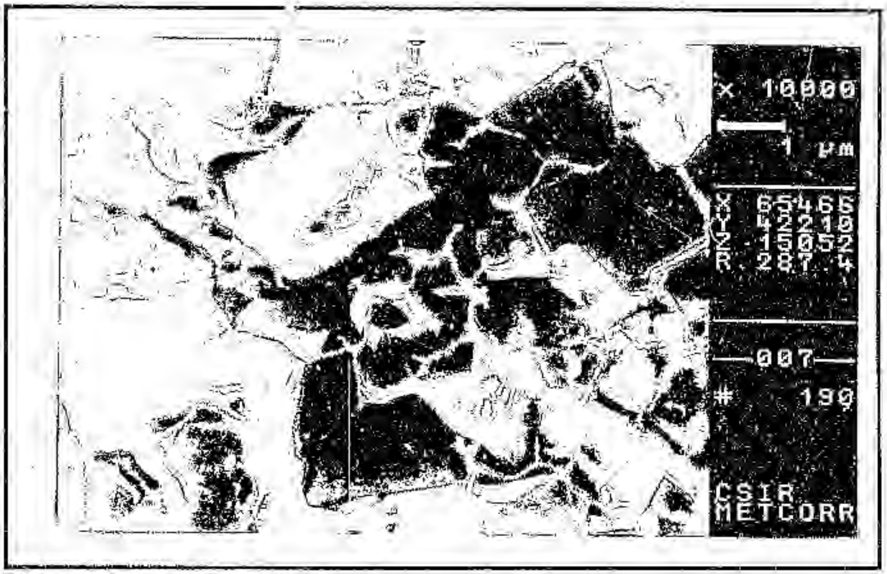

Figure 4.21
Fast Fracture
Grade G6

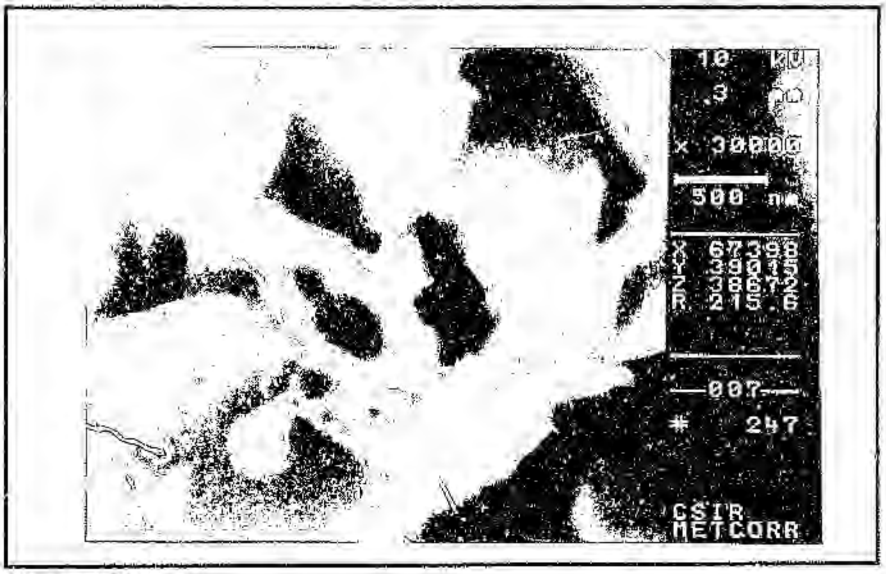

Figure 4.22
Fast Fracture
Grade T6

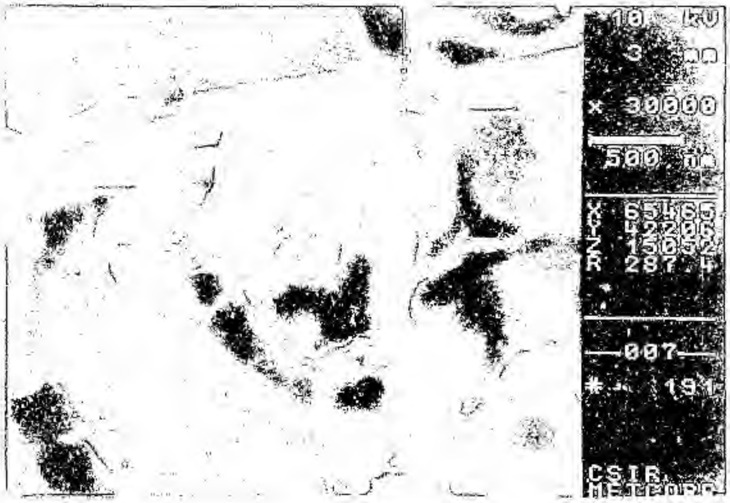

Figure 4.23
Fast Fracture
Grade G6

4.3.2 Precrack Fractography

At a low magnification, considerable crack branching and change in fracture surface orientation are visible in the precrack region. For instance, a "step" can be seen on the fracture surface shown in *figure 4.24*. The extent to which these fracture surface orientation changes can occur is shown in *figure 4.25*. The crack branching, which generates steps on the fracture surface, is consistent with the crack branching shown in *section 4.1.3* and discussed in connection with the precrack growth mechanism in *section 4.1.3*.

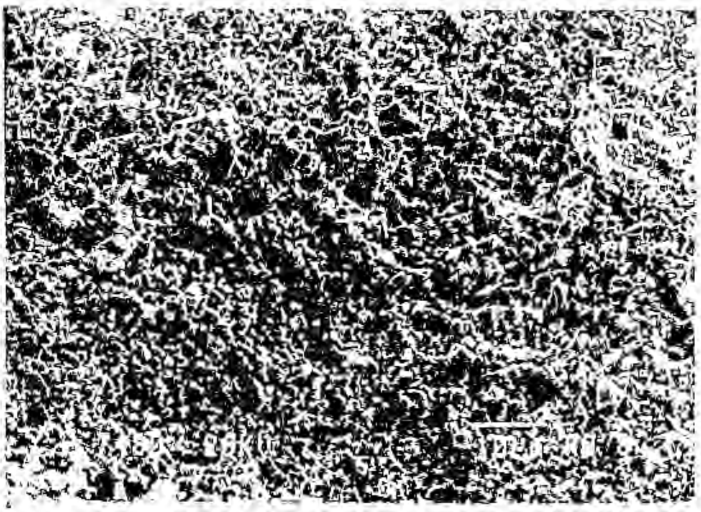

Figure 4.24
Precrack fracture surface
Grade G6

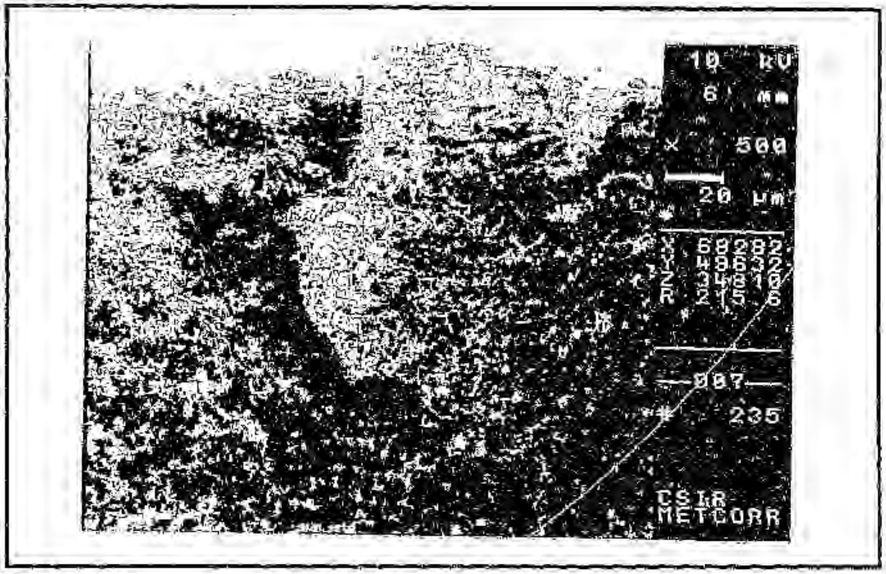

Figure 4.25
Precrack fracture surface
Grade G6

The level changes in the micrograph give the impression of a 'chunk' about to fall off in the manner discussed in *section 4.1.3*.

Two different types of fracture surfaces occur within the precrack region: a cobalt ridge deficient fracture surface and a "intermediate" region in which some cobalt ridges are visible, although less than in the neighbouring fatigue region. *Figure 4.26* was taken on a specimen that was broken without being subjected to fatigue loading and shows the transition from the "intermediate" region to fast fracture : fewer cobalt ridges are visible in the top half of the micrograph than in the bottom half. The following sequence of micrographs, all taken at 5000X magnification on the same T6 specimen, which was broken before being subjected to the four-point bend fatigue test, shows the progression. *Figure 4.27* shows the cobalt ridge deficient region, *figure 4.28* shows the "intermediate" region and *figure 4.29* shows a fast fracture surface for comparison. What is noticeable in this sequence of micrographs is the increase in the number of visible cobalt ridges through the sequence.

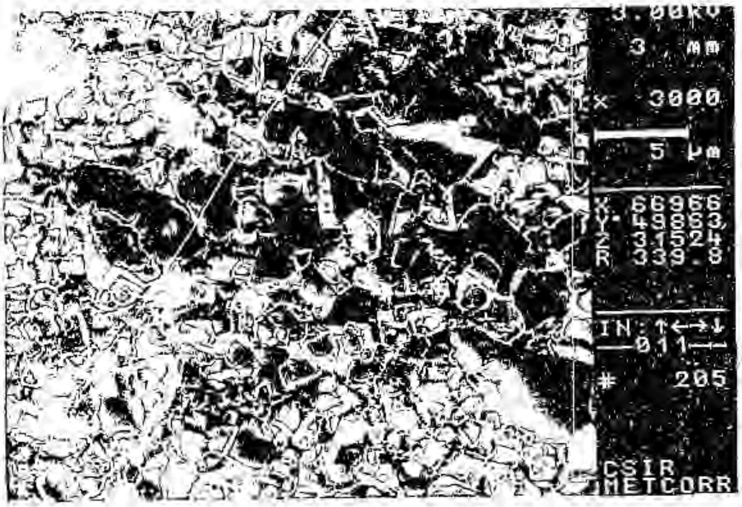

Figure 4.26
Interface between precrack and fast fracture
Grade T6

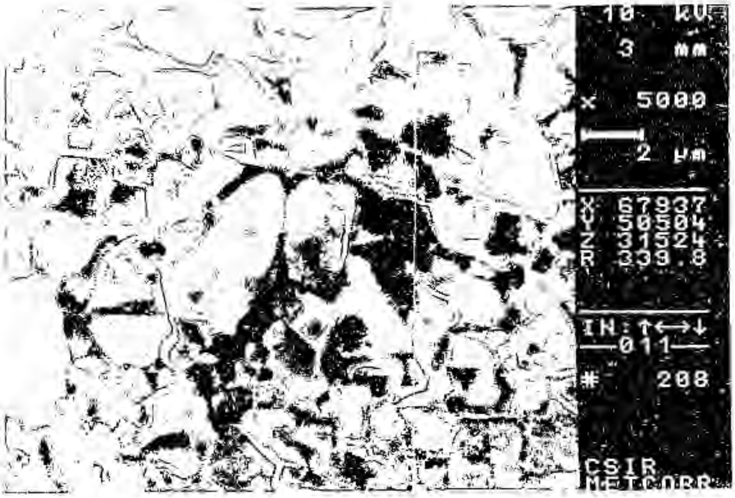

Figure 4.27
Cobalt Ridge Deficient Precrack Region
Grade T6

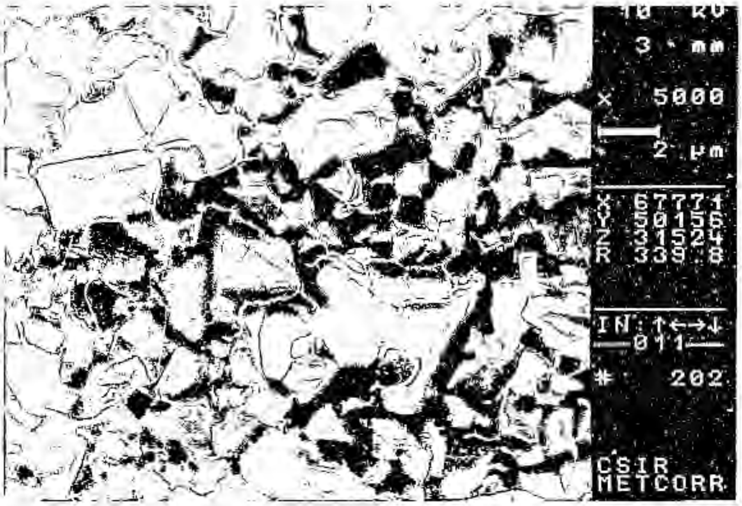

Figure 4.28
Intermediate Precrack Region
Grade T6

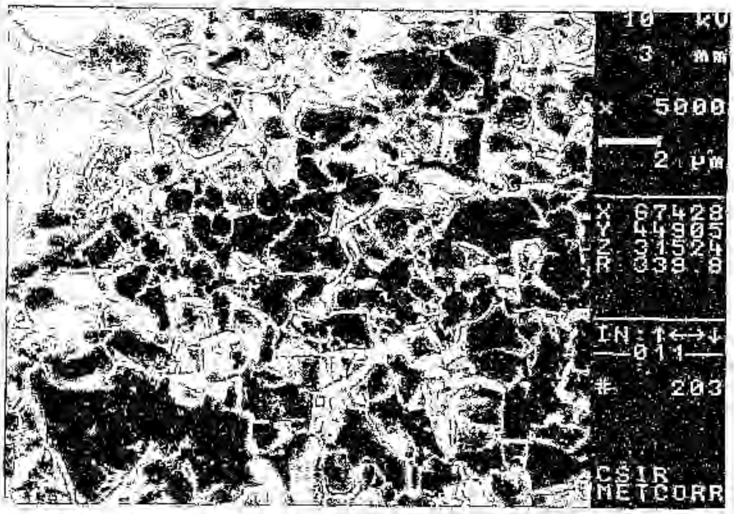

Figure 4.29
Fast Fracture Surface
Grade T6

Figure 4.30 shows the cobalt deficient precrack region in grade G6. As in T6, there are no visible cobalt ridges.

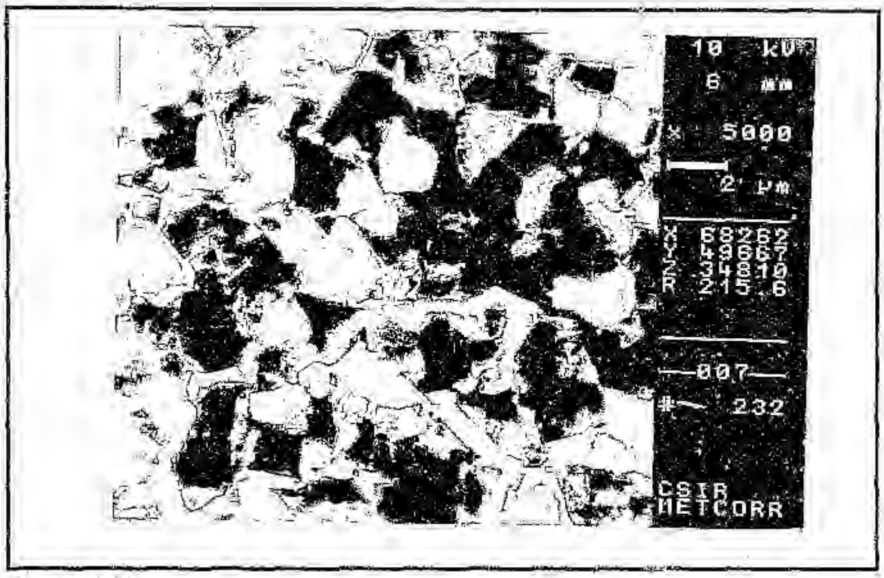

Figure 4.30
Cobalt ridge deficient area
Grade G6

Figure 4.31 shows the cobalt ridge deficient region in grade T6 at higher magnification. There are no cobalt ridges visible in the micrograph. The WC grains appear to be chipped - there are no sharp corners visible. There is some cobalt visible on the fracture surface, but it does not occur in clearly defined ridges. There is also some debris on this part of the fracture surface. The same features are visible in grade G6, as shown in *figure 4.32*.

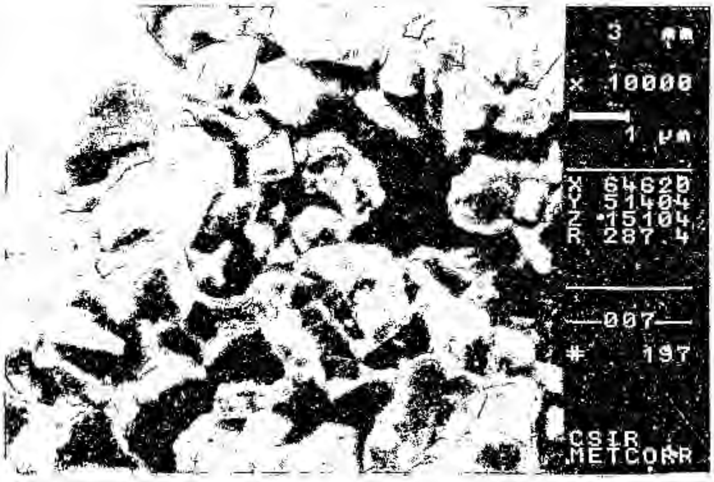

Figure 4.31
Precrack Cobalt Ridge Deficient Region
Grade T6

Figure 4.32
Precrack Cobalt Ridge Deficient Region
Grade G6

Figure 4.33 shows the "intermediate" region at higher magnification. Some cobalt ridges are visible, but fewer than in *figure 4.34*, which is the fast fracture surface for comparison. There is also some carbide grain damage in the intermediate region, for instance the large carbide grain on the left of *figure 4.33*.

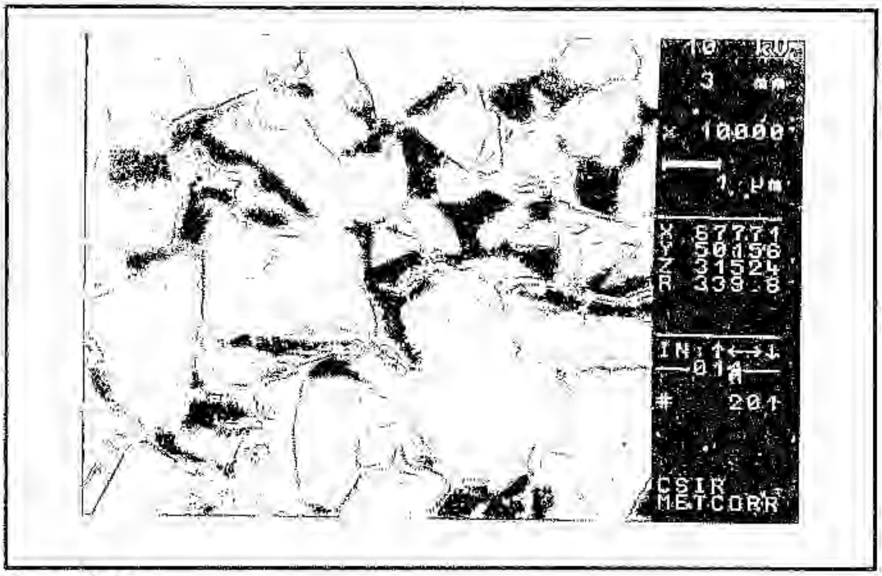

Figure 4.33
Intermediate Precrack Fracture Surface
Grade T6

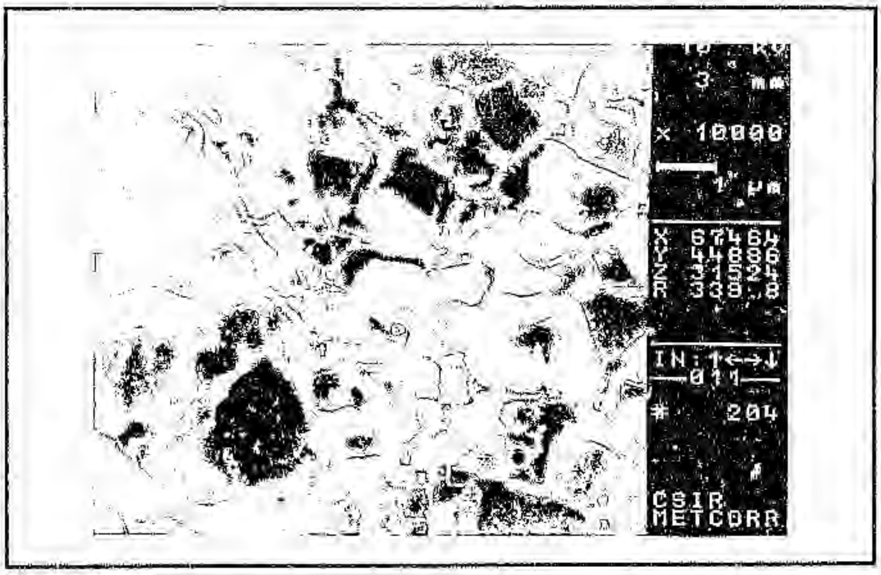

Figure 4.34
Fast Fracture Surface
Grade T6

That there are two separate fracture surfaces in the precrack region should not be surprising, since there are two separate mechanisms at work in precrack propagation. The first mechanism is the mechanism by which the sharp, fine initial cracks grow and the second mechanism is that which occurs when the 'chunk' of material falls out, destroying the original fracture surfaces. There is no doubt that the cobalt deficient regions have been substantially more damaged than the 'intermediate' regions which suggests that the 'intermediate' region corresponds to the initial, fine cracks, while the cobalt deficient region corresponds to the dislodged material.

The lack of cobalt ridges on parts of the precrack fracture surface can be explained by examining the loading conditions. Normally, cobalt ridges form in the presence of unidirectional stresses which results in the cobalt ligaments elongating in the direction of the applied stress. In this case, the material is successively crushed by repeated compressive loading. This means that the ligaments will not be pulled apart unidirectionally to form cobalt ridges. Rather the ligaments will be torn and squashed by the repeated loading.

4.3.3 The Fatigue Surface

4.3.3.1 Crack Morphology

In the four-point bend fatigue test, the cracks observed through the travelling microscope did not exhibit crack branching and consisted of a single thin line, in which the dye penetrant pulsed as the crack opened and closed. Immediately after the specimens were broken in the four-point bend fatigue test, the fatigue crack marked by the dye-penetrant on the fracture surface exhibited very little crack bowing and was the same length on either side of the specimen.

4.3.3.2 Fractography

At lower magnifications, the fatigue fracture surface is similar to the fast fracture surface. At higher magnifications, the appearance of the carbide grains remains the same as in fast fracture - but the appearance of the cobalt ridges differs dramatically. *Figures 4.35* and *4.36* show fast fracture and fatigue surfaces respectively in grade T6. The appearance of the cobalt differs dramatically : the fast fracture cobalt appears as ridges and dimples, while the fatigue cobalt is blurred and rugged. This effect is also illustrated in *figures 4.37* and *4.38* at higher magnification. Finally, G6 fatigue fracture surfaces are shown in *figures 4.39* and *4.40*.

Fast fracture in WC-Co occurs first by a crack extending through the carbide phase, and then by void nucleation and growth in the cobalt phase (Sigi and Schmauder, 1988). As the voids increase in size behind the opening crack, ligaments of cobalt are stretched until they rupture (Fischmeister *et al*, 1988). The result is the smooth cobalt ridges visible on the fast fracture surfaces. In fatigue, the cobalt that remains on the carbide grains differ dramatically from fast fracture. The fatigue cobalt is rugged and does not form well defined ridges. This suggests that a different type of failure mechanism is taking place in the cobalt during fatigue.

Almond and Roebuck (1980) suggested that the cobalt failure mechanism may change from ductile to brittle due to the fatigue loading. Further, Schleinkofer *et al* (1996) showed that a phase change from f.c.c to h.c.p. takes place in the cobalt binder ligaments behind the crack tip. The same martensitic phase transformation was shown to occur around the crack tip. This phase transformation strongly reduces the amount of plastic deformation that can take place in the cobalt.

TEM micrographs of fatigue cracks show parallel cleavage cracks in the cobalt which give a 'zig-zag' shape to the overall fracture (Kursawe *et al*, 1998). This 'zig-zag' appearance appears to match with the rugged appearance of the cobalt in the present fatigue SEM micrographs. The rugged, uneven appearance of the cobalt may therefore be explained by brittle microcracking occuring in the h.c.p. cobalt in the cobalt ligaments and around the crack tip.

Schleinkofer *et al* (1996) also reported that the fatigue crack travels almost entirely through the cobalt phase. This is also the case here as the WC grains do not have cleavage patterns.

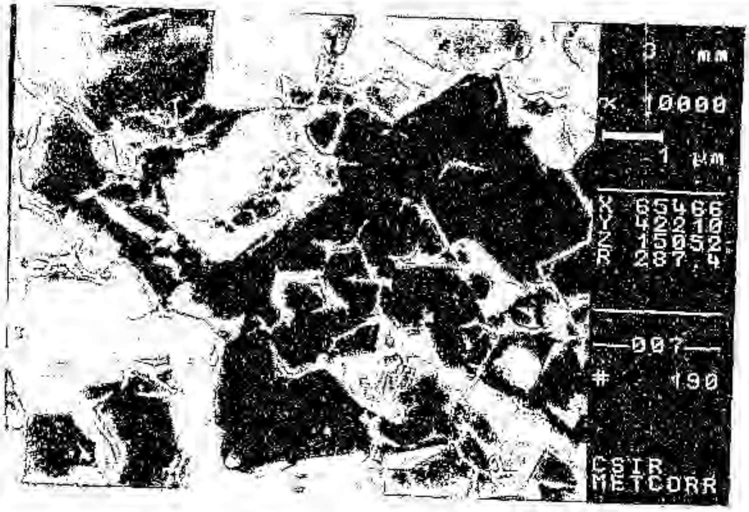

Figure 4.35
Fast Fracture Surface
Grade T6

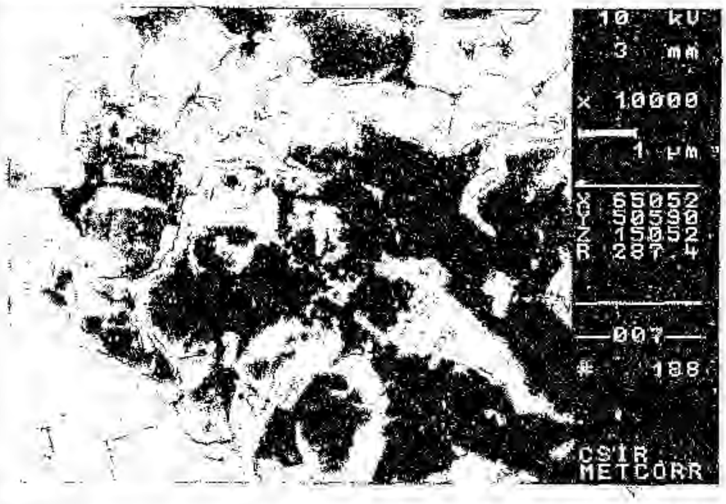

Figure 4.36
Fatigue Fracture Surface
Grade T6

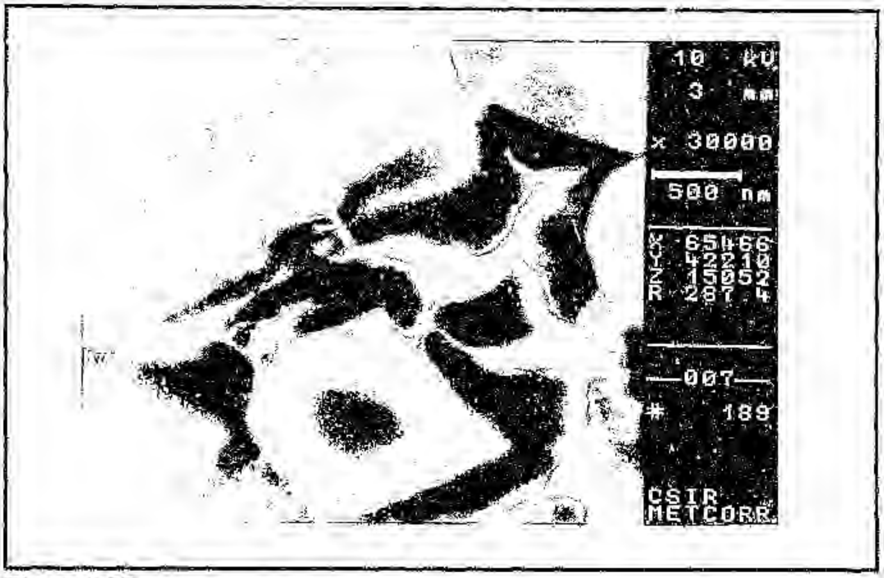

Figure 4.37
Fast Fracture Surface
Grade T6

Figure 4.38
Fatigue Fracture Surface
Grade T6

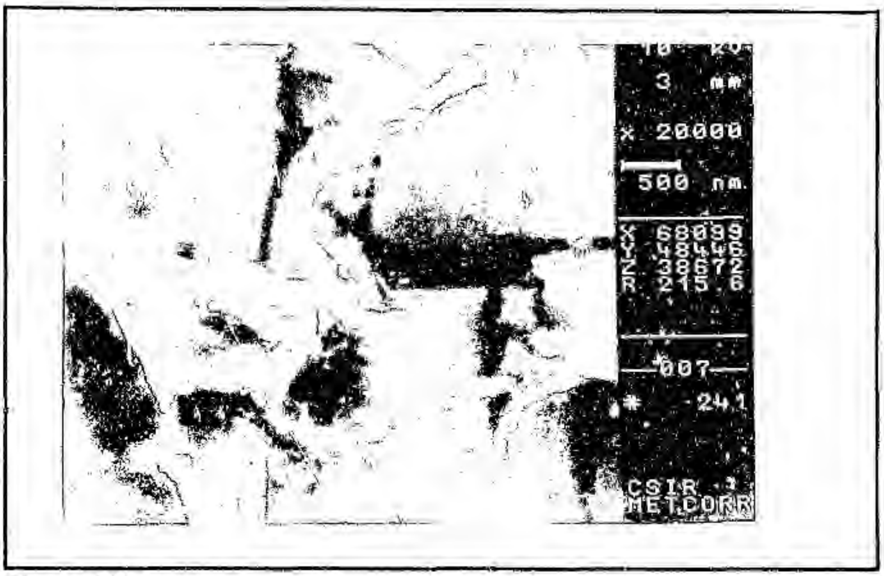

Figure 4.39
Fatigue Fracture surface
Grade G6

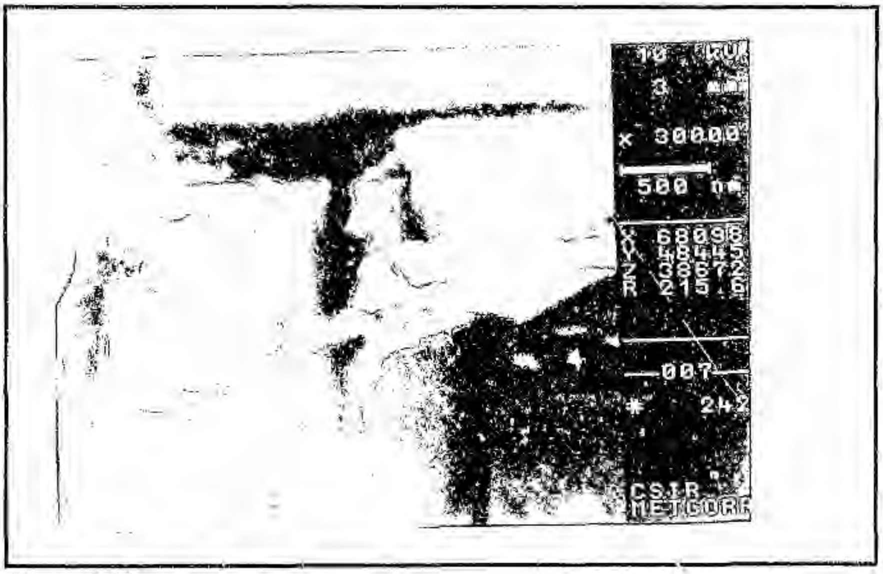

Figure 4.40
Fatigue Fracture Surface
Grade G6

4.4 Stress Analysis

Figure 4.41 shows the geometry of the microstructural model before loading, with the Co regions in red and the WC in green. The grey area is the notch that will be removed. The blue areas around the microstructure represent the bulk WC-Co.

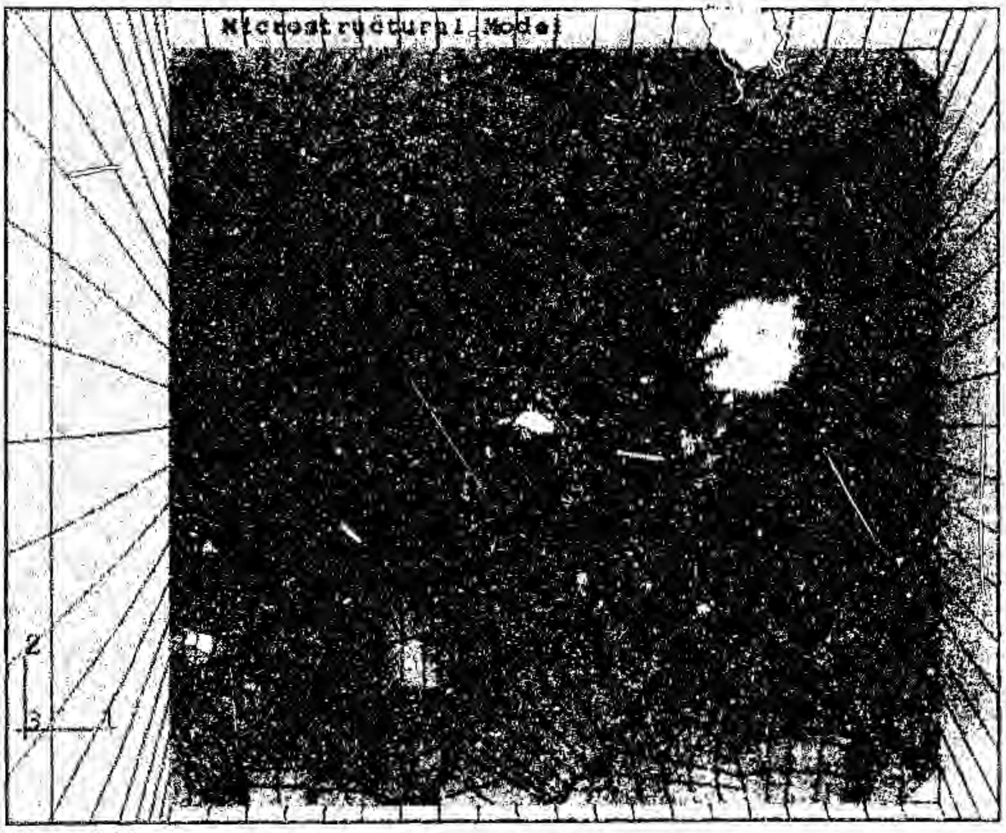

Figure 4.41
Microstructural FEM

All the stress values in the contour map legends in the following figures are in *Pa*.

4.4.1 Step 1 : Residual Thermal Stresses

In *figure 4.42* below, the larger of the principal stresses in the plane of the model is mapped. The stresses in the Co regions mostly range between 70 and 1860 *MPa*, while the stresses in the WC grains are mostly between -1000 and 70 *MPa*. At corners of WC grains and where WC grains meet, higher compressive stresses are generated. These can be as large as -2000 *MPa*.

Figure 4.43 shows the smaller of the principal stresses in the plane of the model. Here the stresses in the Co vary from -200 to 1000 *MPa*, while the stresses in the WC vary from below -1000 *MPa* to 400 *MPa*.

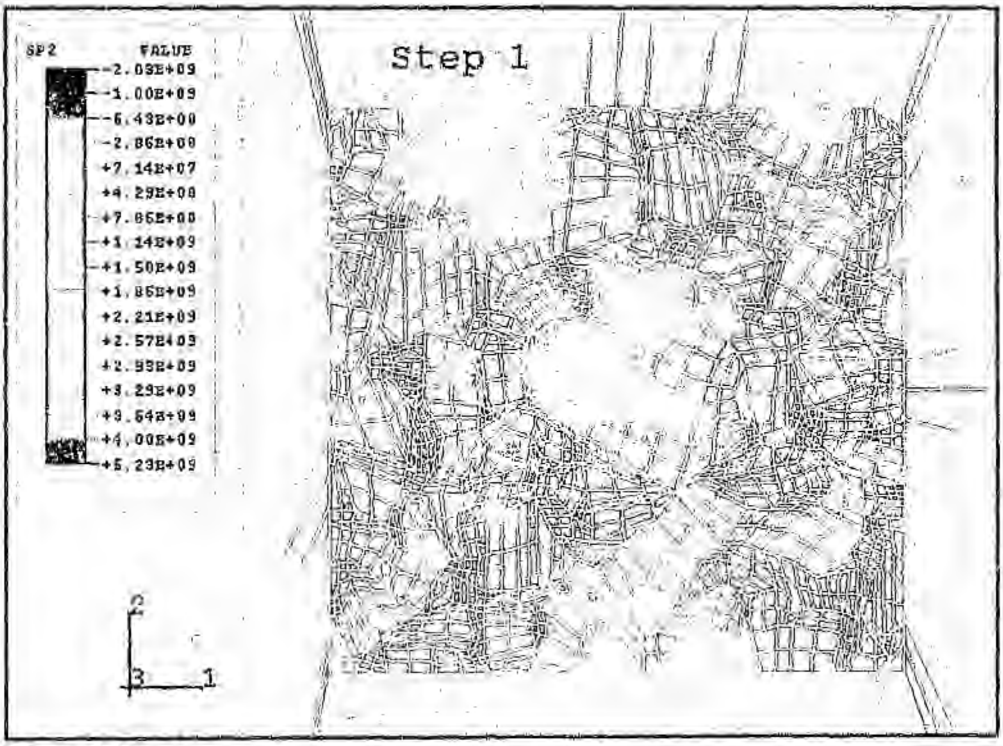

Figure 4.42
Step 1 : Residual Thermal Stress
Larger of the principal stresses in the plane of the model

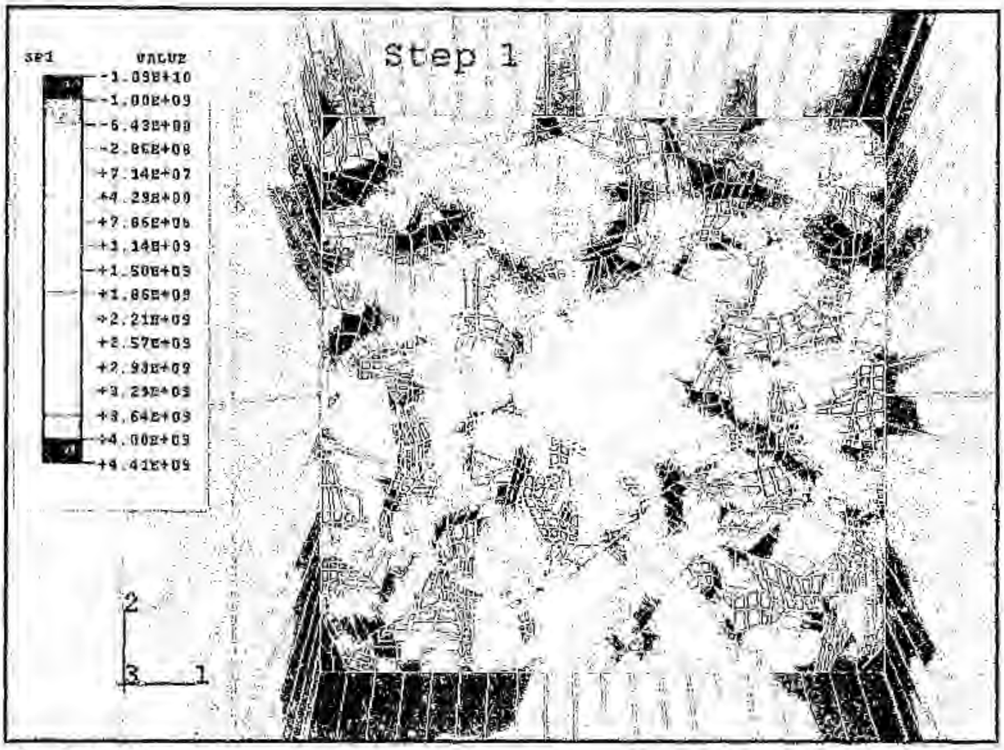

Figure 4.43
Step 1 : Residual Thermal Stresses
Smaller of the principal stresses in the plane of the model

4.4.2 Step 2 : Cutting the Notch

In the second step, the elements making up the notch are removed. This can be seen on the left of the microstructural region. *Figures 4.44* and *4.45* compare the stresses in steps 1 and 2. Here, the larger of the principal stresses in the plane of the model are mapped again. The stress contour maps remain mostly the same, but some of the high compressive stresses in the WC are released at the notch base and the tensile stresses in the Co alongside the notch are also reduced.

In *figures 4.46* and *4.47*, the smaller of the principal stresses are compared in steps 1 and 2. Once again some of the higher tensile stresses in the Co near the notch are relaxed, while some of the larger compressive stresses in the WC are relaxed. But, some new areas of compressive stresses form away from the notch, as the stresses are redistributed away from the notch free surface into the bulk of the material (compare *figures 4.46* and *4.47*).

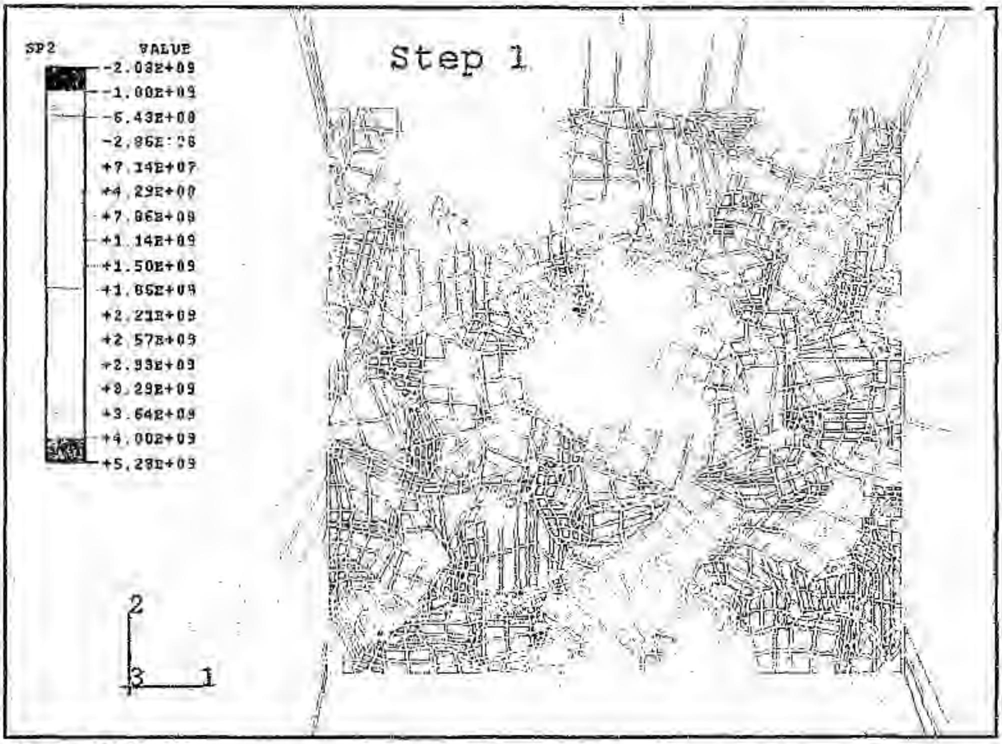

Figure 4.44
Step 1 : Residual Thermal Stresses
Larger of the principal stresses in the plane of the model

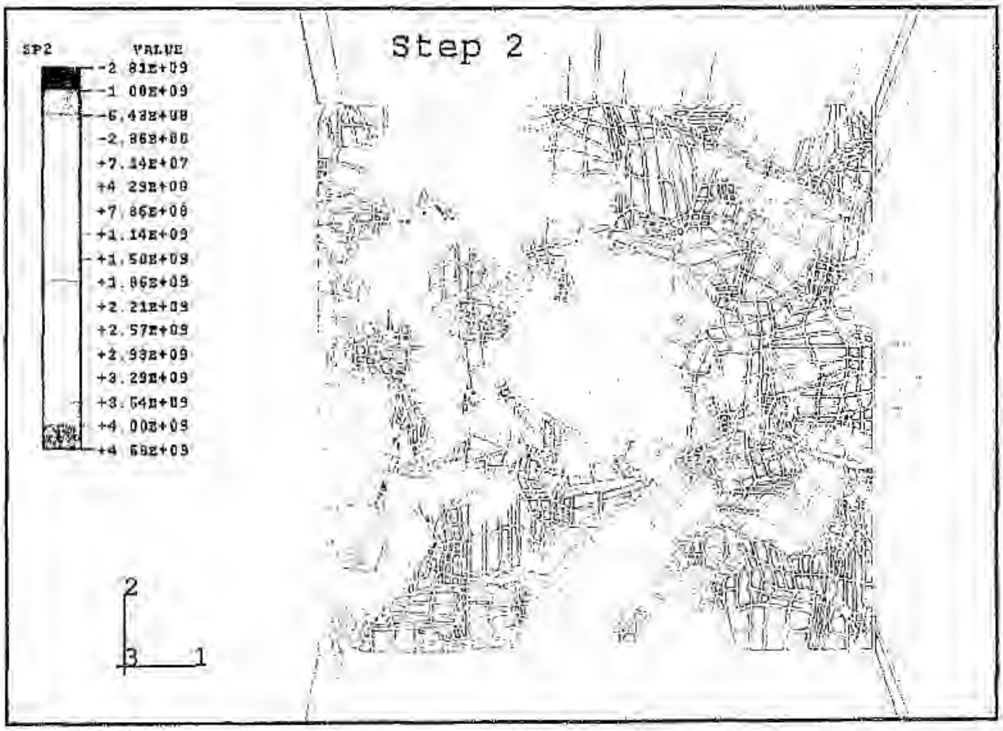

Figure 4.45
Step 2 : Cutting the notch
Larger of the principal stresses in the plane of the model

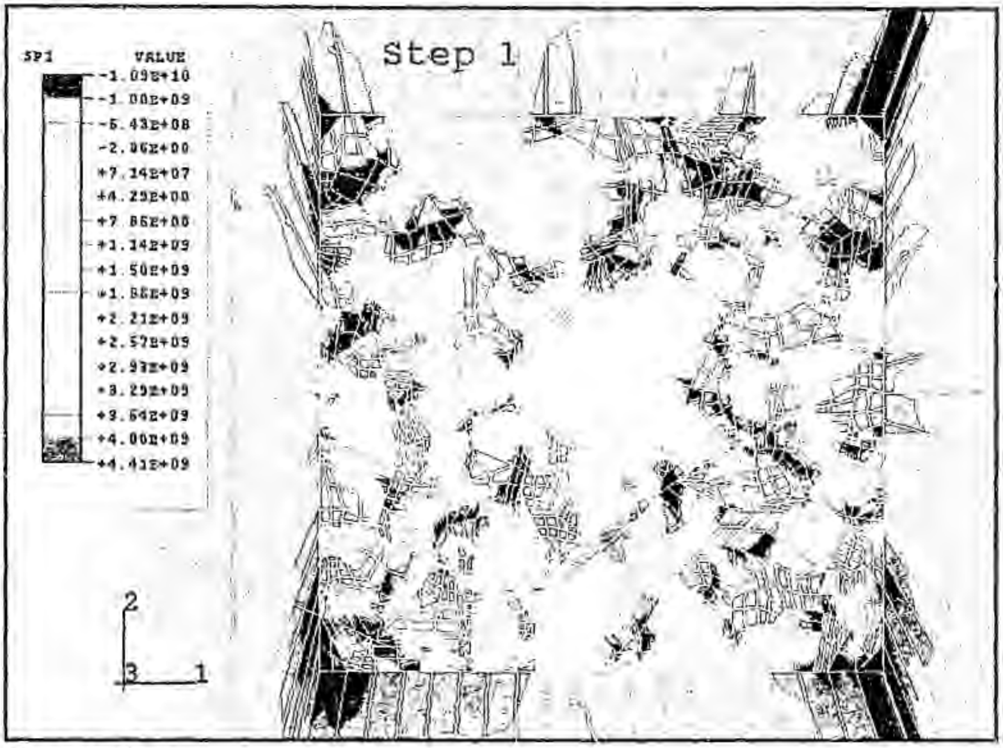

Figure 4.46
Step 1 : Residual Thermal Stresses
Smaller of the principal stresses in the plane of the model

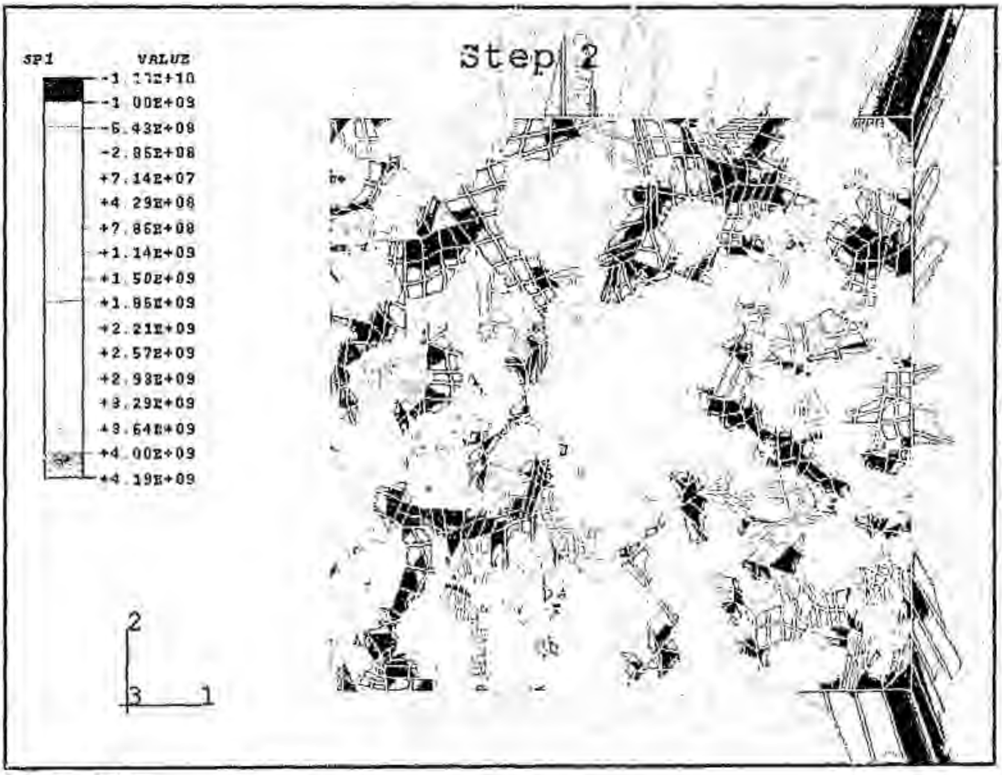

Figure 4.47
Step 2 : Cutting the notch
Smaller of the principal stresses in the plane of the notch

4.4.3 Step 3 : Loading the Specimen

The model was loaded to the same loads as the T6 specimens:

$$P_{max} = -65.6\ kN$$

First, the results of loading the bulk continuum model are presented so as to give an idea of the stresses that are generated by the loading regime. *Figure 4.48* is a map of the stresses in the loading direction (direction 2 on the map) in the stress state only model. The high stresses generated at the corners of the square region are not truly representative of the stress state, as the stress concentrators that occur at the corners of the square region do not, in fact, exist. This stress concentrator is a result of the geometry with which the microstructural part of the model is connected to the continuum model and is, therefore, not a 'real' representation of the stresses that arise. So ignoring those stresses, a maximum compressive stress of -1000 *MPa* is generated in the specimen, while tensile stresses of up to 2000 *MPa* are generated at the base of the notch. The compressive stresses in the model are considerably lower than the compressive strength of T6 WC-Co which is quoted at 4610 *MPa* by the manufacturer (Boart Longyear, 1996).

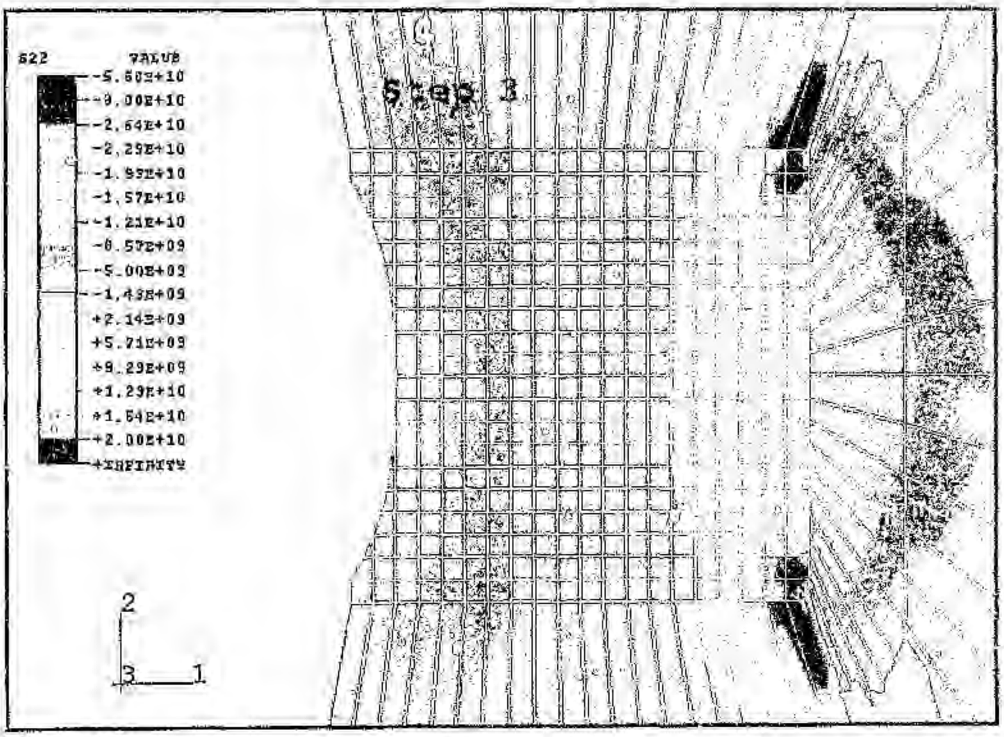

Figure 4.48
Step 3 : Loading the specimen
Stress state FEM
Direction 2 : the loading axis

In *figure 4.49* below, only the tensile stresses from *figure 4.48* are mapped (all the compressive stresses are represented in dark blue). This map shows that there is, in fact, a region of tensile stresses at the notch tip during compressive loading, concurring with the results of Suresh & Brockenbrough (1988). The tensile stresses range up to 2000 *MPa*.

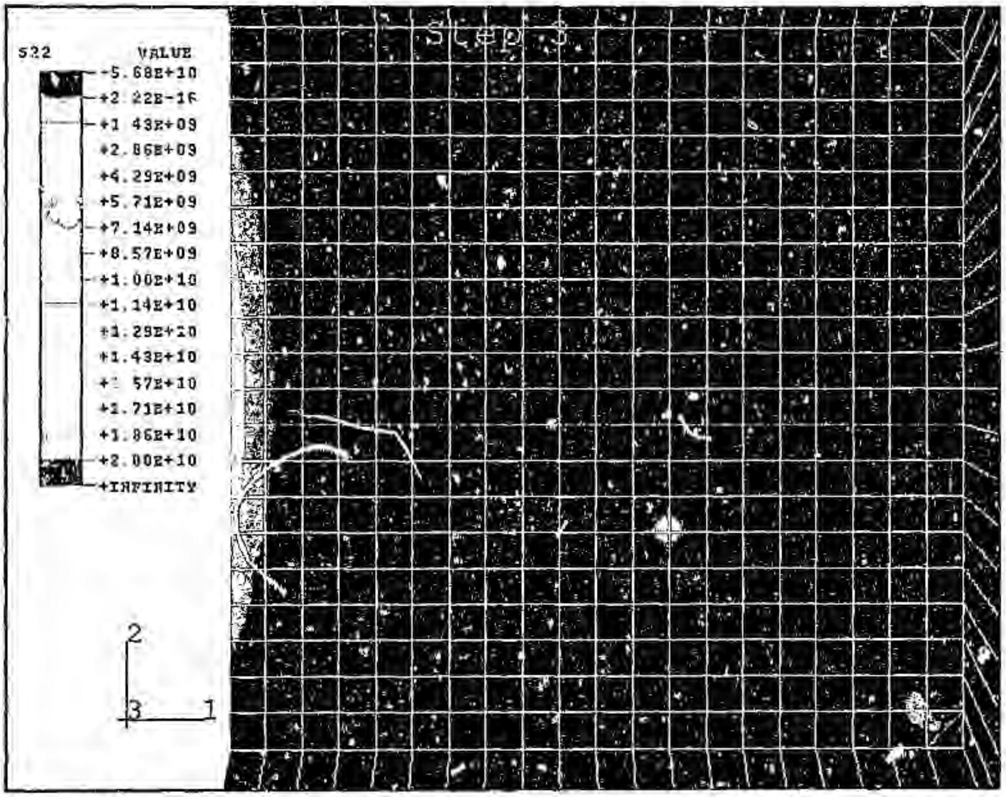

Figure 4.49
Step 3 : Loading the specimen
Tensile stresses in the stress state model
Stresses in direction 2 : the loading axis

Figure 4.50 is a map of the stresses in the direction 1. Once again, disregarding the effect of the false stress raising corners, maximum compressive stresses of -5000 *MPa* are generated. Some tensile stresses (up to 2000 *MPa*) are generated at the notch tip.

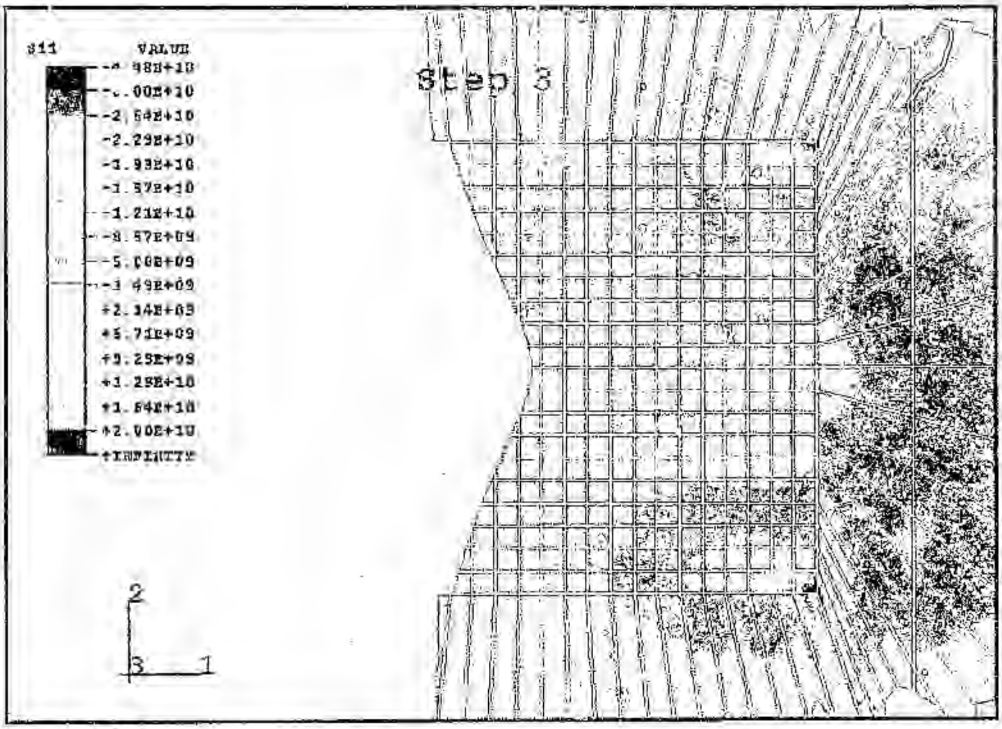

Figure 4.50
Step 3 : Loading the specimen
Stress state model
Stresses in direction 1

In *figures 4.51* and *4.52*, the stresses in the directions 2 and 1 are shown, this time on the microstructural model. In these stress maps, the effect of the composite microstructure on the stresses generated during loading is marked. In both directions, the stresses cover a wide range of values, from -10 000 *MPa* (which is well above the compressive strength of the material) to 10 000 *MPa*. But for the most part, the stresses in the cobalt range between -1000 *MPa* and 2000 *MPa*.

Further, there are some regions, particularly in the direction of the loading axis, that the compressive stresses reach a magnitude of -80 *GPa*. These regions of high localised compressive stresses occur where WC grains meet in the loading axis. These very high stresses are an indication of the areas in which failure is likely. In reality, some deformation of the carbide grains (as here they have only been given elastic properties) or cracking within or between grains would occur at these sites. Similarly, the areas of very high tensile stresses indicated in direction 1 will have failed before such high stresses have built up.

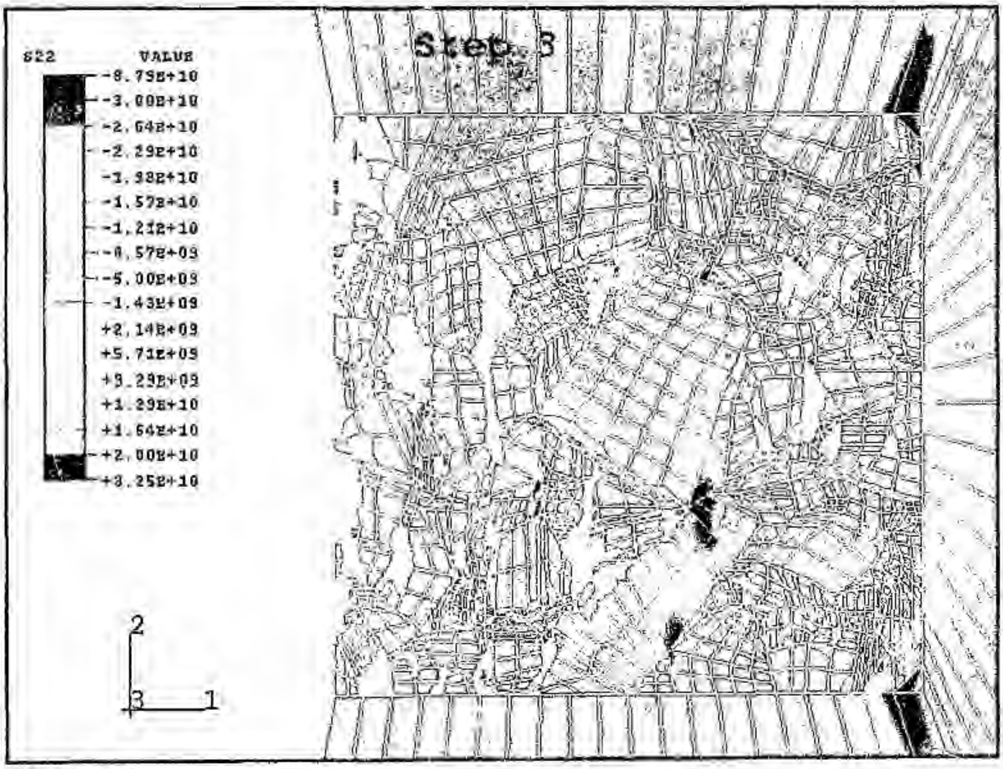

Figure 4.51
Step 3 : Loading the specimen
Stresses in direction 2 : the loading axis

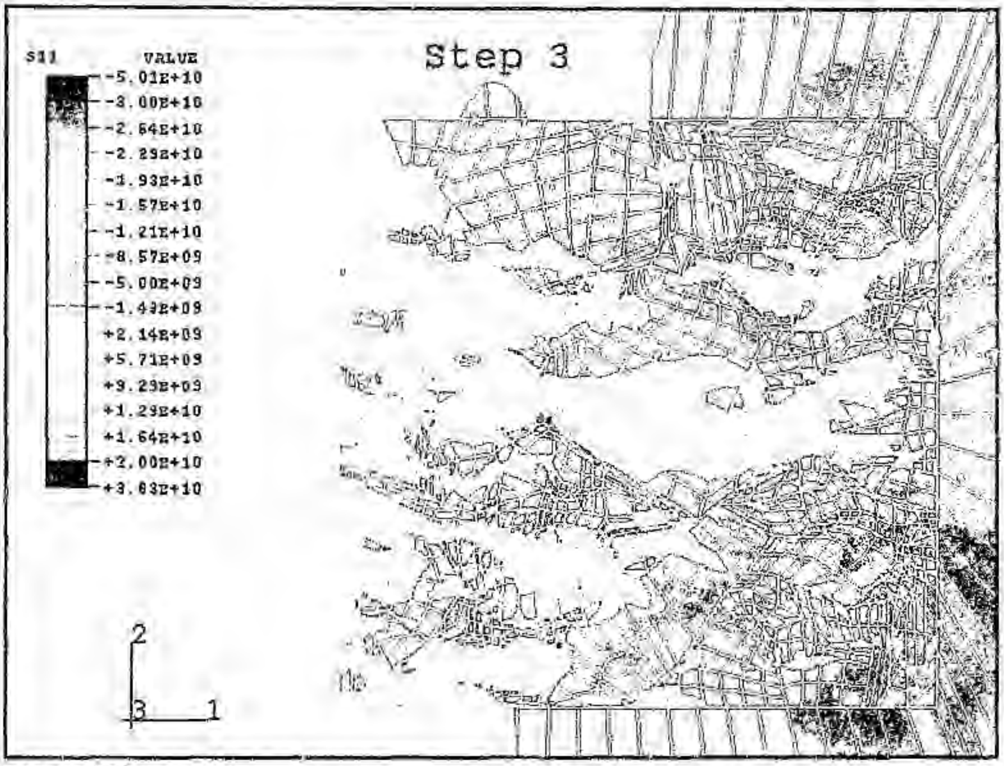

Figure 4.52
Step 3 : Loading the specimen
Stresses in direction 1

Figure 4.53 shows the equivalent plastic strain in the cobalt. When the Gurson model is used in *ABAQUS*, this value acts as a yes/no flag, telling whether the material is currently yielding or not (*ABAQUS* Standard Users Manual, 1996). The figure shows that deformation is occurring in areas of the Co phase.

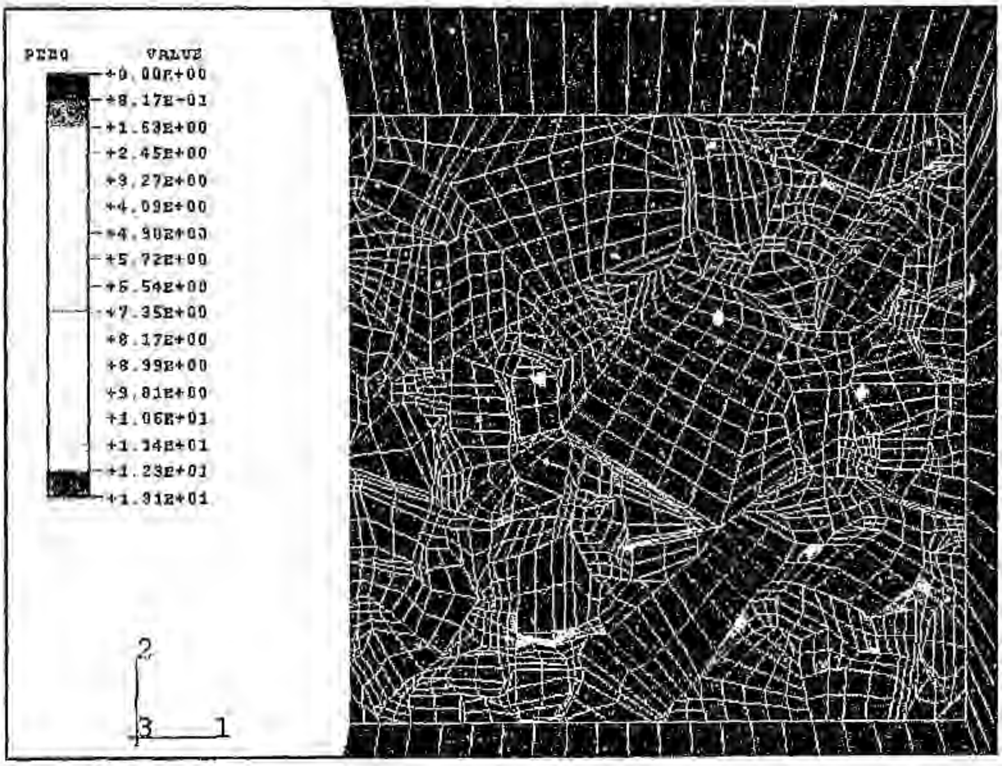

Figure 4.53
Step 3 . Loading the specimen
Plastic deformation in the cobalt

4.4.4 Step 4 : Unloading the Specimen

In *figures 4.54* and *4.55*, the microstructural model of the unloaded specimen is presented. *Figure 4.54* represents once again the stresses in the loading direction : near the notch tip the stresses generally remain similar to those generated during loading. But further away from the notch tip (in the region of 10 *μm* away from the notch tip), extremely high tensile stresses are generated (up to 20 000 *MPa*) . These tensile stresses are a result of the plastic flow in the cobalt. This can be seen by comparing the figure below with *figure 4.53*. The high stress regions in the carbide in *figure 4.54* coincide with the areas of plastic flow in the cobalt. When the specimen is unloaded, the plastic flow in the cobalt remains (this can be seen in *figure 4.56*) and causes the new stresses in the carbide. Also, the extremely high localised compressive stresses that were generated during loading were not relieved by the unloading.

There is very little change in the picture of the stresses in direction 1 on unloading.

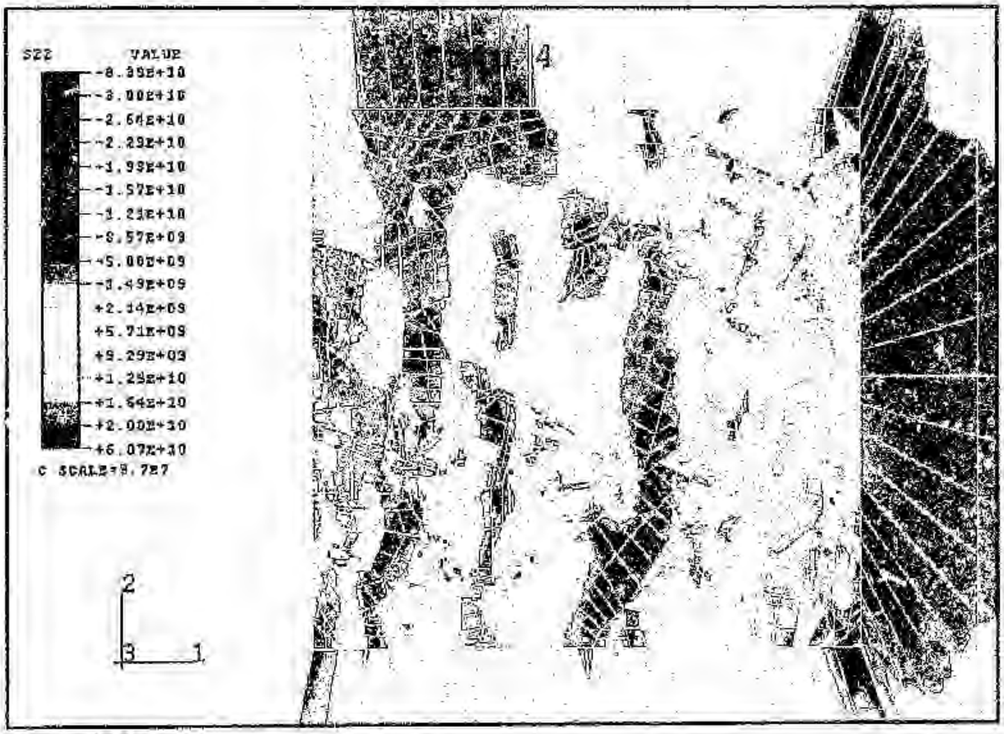

Figure 4.54
Step 4 : Unloading the specimen
Stresses in direction 2 ; the loading axis

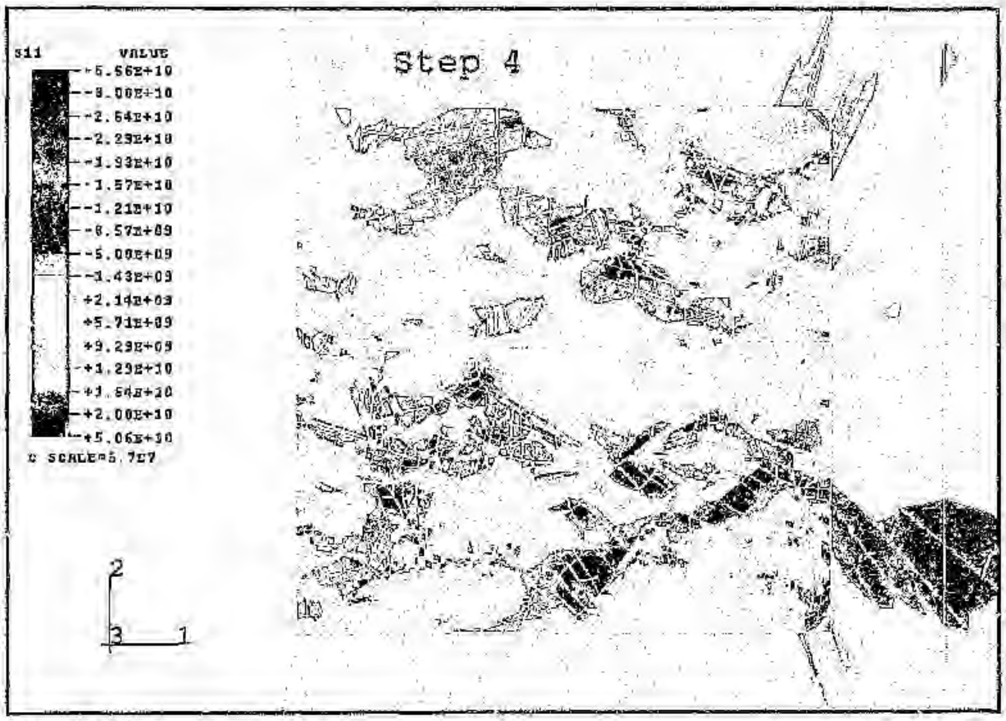

Figure 4.55
Step 4 : Unloading the specimen
Stresses in direction 1

In *figure 4.56* below, the equivalent plastic strain is plotted for step 4. Once again, some deformation is present in the Co phase. These is no difference between the areas of plastic flow in *figure 4.54* (which occur during step 3) and those below.

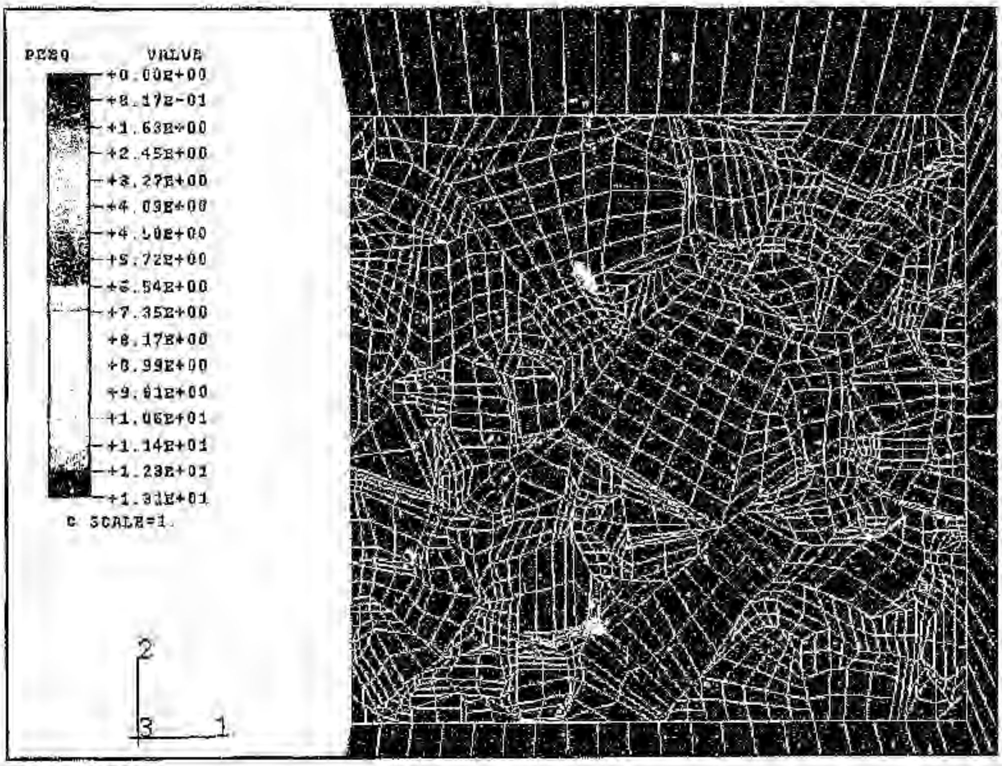

Figure 4.56
Step 4 : Unloading the specimen
Plastic deformation in the cobalt

4.4.5 Void Formation

Void nucleation and growth are defined by three variables in ABAQUS:

ε_N, the mean value of the normal distribution of the nucleation strain, typically 0.1 to 0.3

s_N, the standard deviation of the normal distribution of the nucleation strain, usually 0.05 to 0.1 and

f_N is the volume fraction of nucleated voids, given as 0.04

The values of the three variables stated above are the values given by Tvergaard and Needleman, 1984, for a typical metal. Tvergaard and Needleman determined these values for void formation in a steel bar, subjected to unidirectional tensile loading.

Using these values in the final element model resulted in the formation of voids during step 1, which is contrary to the fact that WC-Co is fully dense after sinter HIPing. In addition, these values led to such a large amount of void formation during step 3 (the loading), that the Gurson constitutive model no longer applied and the stresses could not be calculated.

The void nucleation values were adjusted until no voids were formed during cooling and until the loading stresses could be calculated. Finally, the following values were used for the void nucleation variables:

$\varepsilon_N = 3$

$s_N = 0.01$

$f_N = 0.001$

The increase in mean strain and decrease in void nucleation volume can be explained by the highly constrained nature of the cobalt. Under such constrained conditions, a very large deviatoric stress component will be required for void nucleation and growth, hence the greater difficulty in nucleating and growing voids than in unconstrained tension.

Figure 4.57 represents the voids that have formed in the cobalt phase during step 3, ie the loading of the specimen, while *figure 4.58* shows the one area where voids did form in closer detail. In the contour maps that follow, the void volume fraction is mapped. A vvf of 1 means that the material is fully voided, while a vvf of 0 (as is almost the case in the following contour maps) means that the material is fully dense.

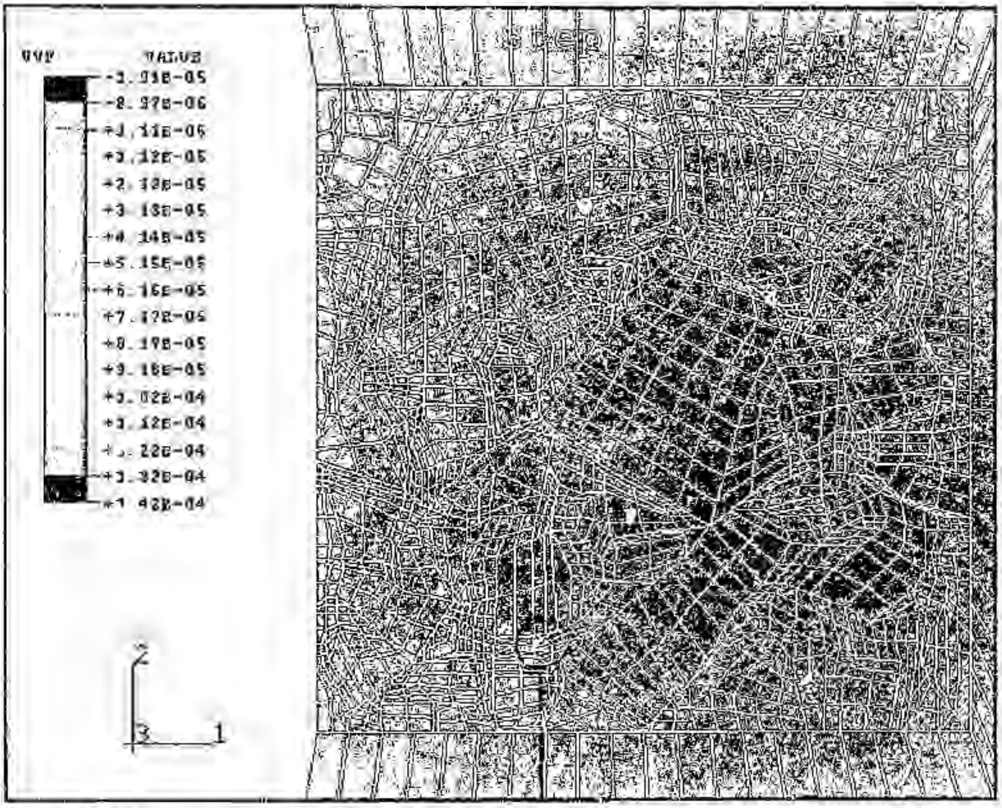

Figure 4.57
Step 3 : Loading the specimen
The void volume fraction

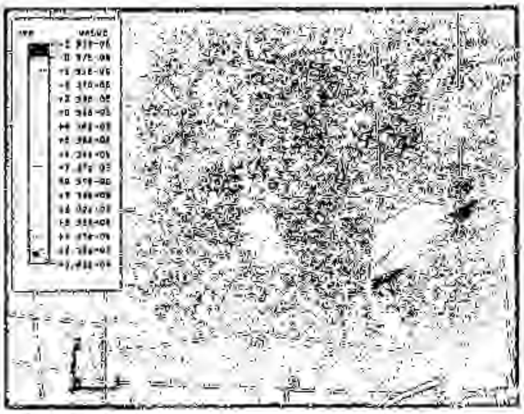

Figure 4.58
Step 3 : Unloading the specimen
The void volume fraction

In step 4, ie during unloading, voids formed in more areas than in step 3, as is shown in *figure 4.59*, but the void volume fraction appears to be smaller those areas than was the case in step 3. This can be seen in *figures 4.60, 4.61* and *4.62*. So presumably some of the voids represented in *figure 4.58* actually closed on unloading (compare with *figure 4.60*).

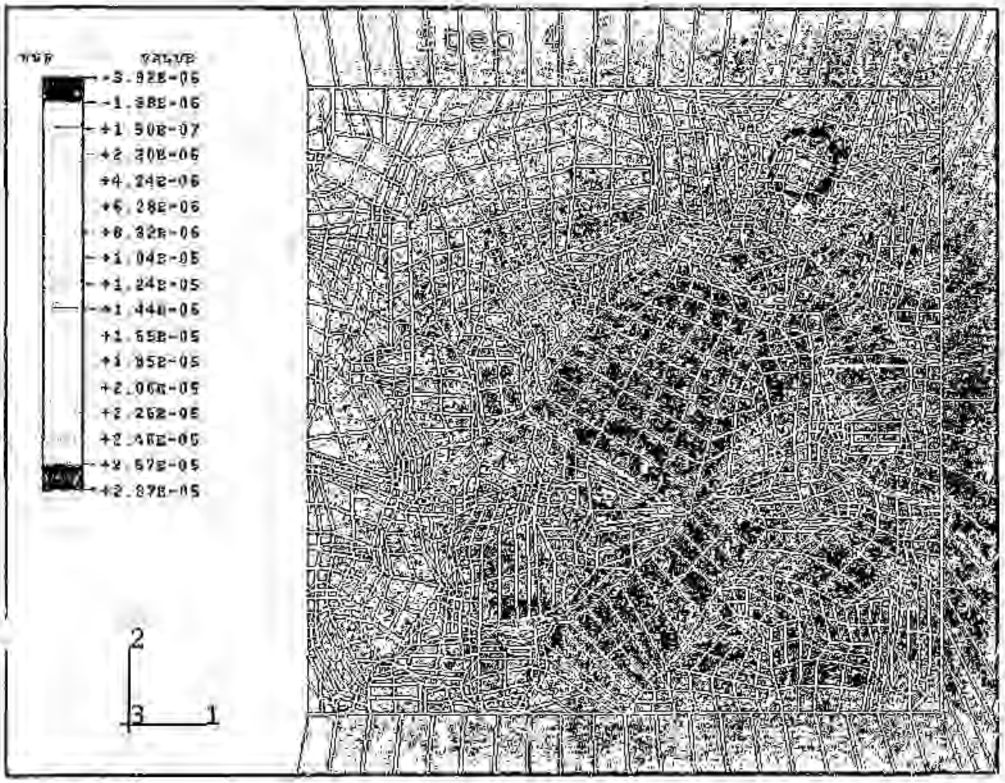

Figure 4.59
Step 4 : Unloading the specimen
The void volume fraction

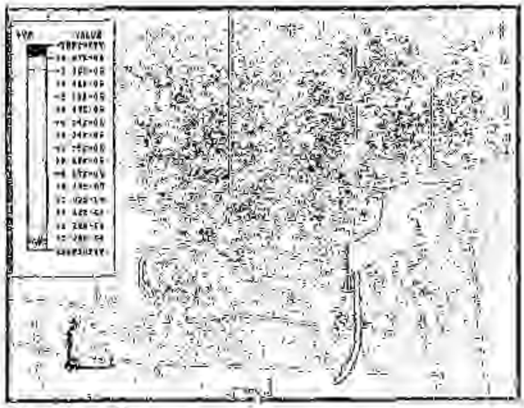

Figure 4.60
Step 4 : unloading the specimen
The void volume fraction

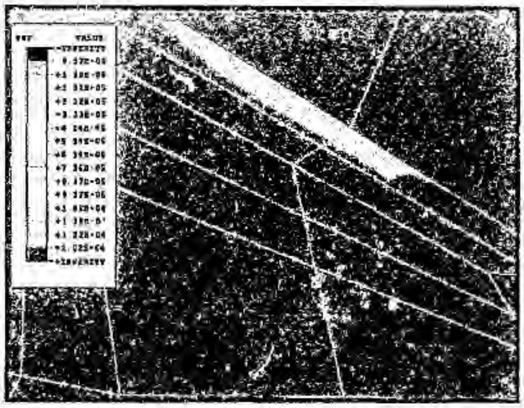

Figure 4.61
Step 4 : Unloading the specimen
The void volume fraction

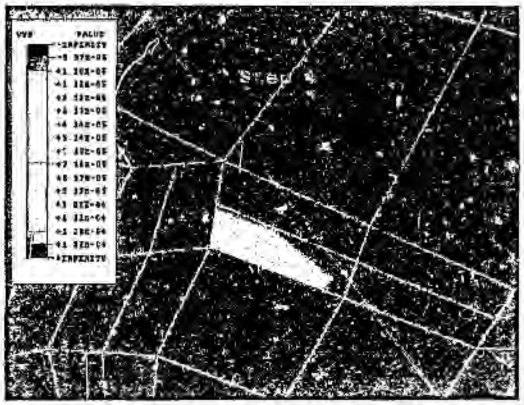

Figure 4.62
Step 4 : unloading the specimen
The void volume fraction

4.5 Verification/Discussion of Stress Analysis

4.5.1 Step 1 : Residual Thermal Stresses

The following table lists results obtained from studies into the residual thermal stresses of WC-6wt%Co. The results are specifically taken from studies on 6wt% cobalt grades, as the magnitude of the thermal stresses varies with the amount of cobalt in the WC-Co alloys (Exner, 1979).

Table 4.3
Residual thermal stresses determined experimentally

Study	Type of Study	Average stress in WC	Range Stresses in WC	Average stress in Co	Range Stresses in Co
Krawitz *et al*, 1988	Neutron diffraction WC-6Co	-280 *MPA*	-840 to 1300 *MPA*		
Exner, 1979	Review of various studies	±-100 *MPA*		±1280 *MPA*	
This study	FEM WC-6Co		< -1000 to 1860 *MPA*		-200 to 1000 *MPA*

For the most part, the residual thermal stresses generated in this model are consistent with compared with those determined in other studies. The bulk of the WC is under stresses between -300 and 70 *MPa*, which values are of the same order of magnitude as those above. But, some areas, particularly where WC grains meet, develop much higher compressive stresses than are reported in the literature.

The cobalt stresses range mostly between 70 and 1000 *MPa*. The occasional small region of compressive stresses does occur in the cobalt, but these regions are not common.

The stresses of largest magnitude, both tensile and compressive, occur along the interfaces between WC grains and cobalt regions or where WC grains meet, as the thermal mismatch is the largest along the interfaces.

4.5.2 Step 2 : Cutting the Notch

As is to be anticipated, cutting a notch in the material reduced the magnitude of residual stresses in the region of the free notch surface. The compressive stresses in the WC at the notch tip were decreased, as were the tensile stresses in the Co.

4.5.3 Steps 3 and 4 : Loading and Unloading

A T6 specimen was subjected to a single load test (once again the specimen was loaded to -65.6 *kN*) and then unloaded. The area at the base of the notch was then examined in the SEM. The only visible damage to the specimen was the cracked WC grain shown in *figure 4.63* below. This cracked WC grain was on the edge of the notch tip, as is consistent with the region of tensile stresses generated by the loading and shown in *figure 4.64*.

Figure 4.63
Damage due to single load cycle

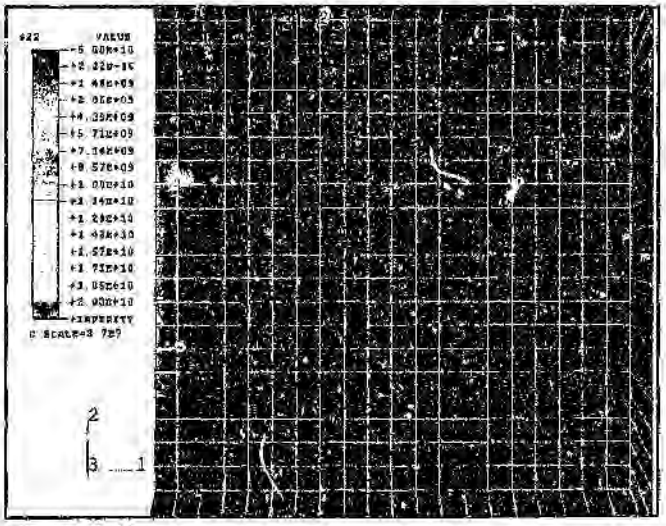

Figure 4.64
Tensile stresses at the notch tip during loading

During the step 3 loading, the cobalt phase showed large regions of deformation (*figure 4.53*) and some void nucleation, so consequently the stresses in the cobalt remain low - mostly between -500 and 500 *MPa*. In addition, the pre-existing tensile stresses in the cobalt (the thermal residual stresses) may also serve to lower the effects of the compressive loading on the cobalt. Much higher compressive stresses are built up in the carbide phases, particularly where carbide grains lie in the direction of the loading axis. Very high tensile stresses build up at right angles to the loading axis, also mostly where WC grains meet. As before, the largest stresses occur at the interfaces between WC and cobalt and where WC grains meet. So it seems that one can expect both plastic deformation in the cobalt and subcritical cracking along the interfaces (between WC and cobalt and where WC grains meet) under this loading regime. This is in agreement with the explanation provided by Suresh and Sylva (1986), who suggested that residual stresses may be introduced into WC-Co during compressive loading as a result of plastic binder flow and thermal mismatch.

When the specimen is unloaded, very high compressive stresses build up in the WC neighbouring areas of cobalt plastic deformation. This can be seen by comparing *figures 4.53* and *4.54*. This would increase the likelihood of subcritical cracking along the carbide-binder interfaces.

Although the areas in which the cobalt yields and the areas in which the high compressive stresses form on unloading coincide, these areas do not coincide with the areas of highest stresses predicted in *figure 4.51* (during loading). This is because the cobalt in these areas has yielded, thereby relieving the highest tensile stresses. Further, plastic flow, by definition, does not relax on unloading, and so although unloading causes considerable change in the stress distribution, there is no concurrent change in the distribution of plastic deformation.

Figures 4.54 and *4.55* show mostly compressive stresses in the cobalt at the notch tip on unloading. These correspond well to the cyclic plastic zone compressive stresses ahead of a crack shown in *Figure 2.5*. In addition, the tensile stresses away from the notch tip in *Figure 4.54* correspond to the monotonic plastic zone in *Figure 2.5*

Most of the plastic flow in the cobalt and the high tensile stresses that form on unloading occur away from the notch tip (see *figures 4.53, 4.54* and *4.56*), although both *figures 4.51* and *4.48* show higher tensile stresses at the notch tip. The uneven distribution of the plastic deformation is probably as a result of the heterogenous nature of the WC-Co microstructure, although further studies would be required to determine how the heterogeneity affects the stress distribution.

5 Conclusions and Recommendations

All the experimental work was carried out on WC-Co grades T6 and G6, which have 6wt% Co and average grain sizes of $1.8\mu m$ and $2.3\mu m$ respectively. The experimental work involved compression-compression fatigue precracking, followed by $\frac{da}{dn}$ vs ΔK tensile fatigue testing in the four-point bend configuration. Both the fracture surfaces resulting from the compression-compression fatigue precracking and from the four-point bend fatigue testing were subjected to fractographic examination.

The compression-compression fatigue cracks described here confirm what is reported in the literature in that the cracks grow perpendicular to the applied uniaxial load and are a means of introducing stable cracks into WC-Co.

As shown in *figures 4.10, 4.12* and *4.13*, there is always a "sharp" (or fine) crack ahead of the main crack tip. This means that the compression fatigue cracks can be used as precracks in $\frac{da}{dn}$ vs ΔK tensile fatigue testing.

Compression-compression fatigue precrack growth rate curves similar to those reported in the literature were generated (*figures 4.1* and *4.2*), but an examination of final precrack lengths against the number of cycles that the precrack is subjected to (*figure 4.9*) suggests that these curves are incomplete, since the final crack length increases with an increasing number of cycles.

Based on the precrack morphology, a new macro mechanism of fine branching crack growth resulting in material being dislodged from the precrack has been presented. Fine cracks ahead of the compression-compression fatigure precrack encircle material and result in the material being dislodged from the test specimen. Material dislodged from the base of the notch increases the notch length and results in the formation of new residual stresses on subsequent loading cycles, causing further precrack growth. This means that the crack does not arrest as previously reported in the literature.

The precracks have been shown to "grow" by a process of "chunks" falling off. It is suggested that this precrack growth macro mechanism should be documented photographically by taking micrographs of the precrack at least every 100 000 cycles. Similarly, detailed growth rate curves need to be generated for the precracking process, with tens of millions of cycles applied to the test specimen. The precracking process could perhaps be continued until the repeated dislodging of material reduces the specimen cross-sectional area to the point at which the specimen fails by fast fracture.

The precrack fracture surface was shown to consist of two different types of fracture surface. The first is what has been called the 'intermediate' fracture surface which probably results from the fine, 'sharp' cracks at the tip of the precrack. This region had some cobalt ridges, but not as many as the fast fracture surface. The second was a region totally devoid of cobalt ridges. This fracture surface corresponds to the 'chunks' of material that fall out of the specimen. The lack of cobalt ridges is attributed to the multiaxial nature of the stresses, which prevents the formation of ridges.

Further study of the compression fracture surface could examine the cobalt in the 'intermediate' region at higher magnifications and compare it with the cobalt in the fast fracture and fatigue regions, as a diagnosis of whether the precracks are 'true' fatigue cracks.

Grades T6 and G6 exhibit similar $\frac{a}{n}$ vs ΔK growth rate curves. The Paris equation exponent obtained for G6 was the same as that determined for T6 within the experimental error, which is contrary to the reports in the literature according to which the exponent for T6 should be higher since T6 has a finer grain size. It seems that the fatigue method and/or conditions used here are not sensitive enough to discriminate between grades of very close properties. The m-value of approximately 18 does, however, correspond well with the m-values for WC-Co reported in the literature.

The cobalt features on the fatigue fracture surface were shown to differ dramatically from the cobalt features on the fast fracture surface: the fast fracture surfaces had smooth, well-defined cobalt ridges, while the cobalt on the fatigue fracture surface was rugged. Other research has suggested that a phase change from f.c.c. to h.c.p. cobalt in the fatigue crack process zone and at the crack tip results in the cobalt becoming more brittle (Schleinkofer *et al*, 1996). The TEM work of Kursawe *et al* (1998) showed a 'zig-zag' fracture resulting from cleavage cracks which occur in the h.c.p. cobalt and this matches perfectly with the 'zig-zag' rugged appearance of the cobalt on the present fatigue fracture surfaces (*figure 4.36* and *4.37*).

A recommendation for further work is to is to determine the planes along which these cracks propagate by electron diffraction to determine their orientation and get a full description of the fatigue mechanism in WC-Co.

The finite element model was used to predict stress distributions in the microstructure at the base of the notch during the first cycle of compression-compression fatigue precracking. In addition to the microstructural FEM (in which separate WC and Co regions were modelled), a stress-state FEM consisting only of WC-Co was developed.

The residual thermal stresses predicted by the microstructural FEM stress analysis are consistent with experimental results of other studies, predicting tensile stresses of up to -2000 *MPa* in the cobalt and compressive stresses of up to -1000 *MPa* in the carbide.

Cutting the notch in the FEM model resulted in the higher residual stresses being relieved at the notch free surface, although more compressive stresses were generated in some parts of the microstructure when the notch was cut (*figures 4.55* and *4.56*).

A region of tensile stresses is generated at the notch tip during the loading of a stress-state only FEM (with stresses of up to 2000 *MPa*). In the microstructural FEM, some tensile stresses are generated in the cobalt (with stresses of up to 10 000 *MPa)*, leading to deformation and void nucleation and growth. The deformation in the cobalt does not occur at the notch tip, which is the region of highest tensile stresses, but rather away from the tip. Very high compressive stresses (predicted as above 30 000 *MPa)* are generated between carbide grains that meet along the loading axis. So failure is expected to initiate both in the cobalt binder and at contacts between carbide grains.

Unloading the specimen results in high tensile stresses (in excess of 30 000 *MPa)* forming in the carbide adjacent to yielded cobalt. So further failure is expected to take place at the carbide-cobalt interface. Unloading has no effect on the high compressive stresses that are generated at contacts between carbide grains. Some of the voids that nucleated on loading seem to close on unloading, but more regions of voids form when the specimen is unloaded.

The parameters for void formation had to be adjusted by an order of magnitude from those for a typical metal found in the literature. There is considerable scope for further investigation into void formation in the cobalt and into determining these parameters, perhaps by developing models at the atomic level.

Appendix 1: Error in Stress Concentration, k, at the root of the notch

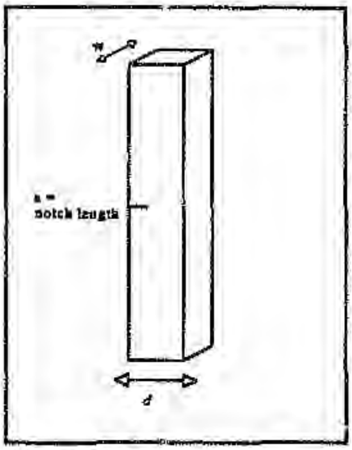

Figure A1.1
Calculation of the stress concentration factor *(k)* at the root of the notch

Using the notation in *Figure 1* :

a = notch depth = 2*mm*
r = notch radius = 0.5 * wafering blade thickness = 0.19*mm*
d = width = 13*mm*
w = depth = 6*mm*

The stress concentration, *k*, at the root of the notch, is obtained using the following equations:

$$k = k_1 + k_2(\tfrac{a}{d}) + k_3(\tfrac{a}{d})^2 + k_4(\tfrac{a}{d})^3 \qquad \text{----------- (1)}$$

where for $0.5 \le \frac{a}{r} \le 4$

$$k_1 = 0.721 + 2.394\sqrt{\tfrac{a}{r}} - 0.127\tfrac{a}{r} \qquad \text{---------- (2)}$$

$$k_2 = 1.978 - 11.489\sqrt{\tfrac{a}{r}} + 2.211\tfrac{a}{r} \qquad \text{---------- (3)}$$

$$k_3 = -4.413 + 18.751\sqrt{\tfrac{a}{r}} - 4.596\tfrac{a}{r} \qquad \text{---------- (4)}$$

$$k_4 = 2.714 - 9.655\sqrt{\tfrac{a}{r}} + 2.512\tfrac{a}{r} \qquad \text{---------- (5)}$$

For $\frac{a}{r} = \frac{2}{0.19} = 10.5$ one obtains:

$k_1 = 7.151$ from (2)
$k_2 = -12.024$ from (3)
$k_3 = 8.044$ from (4)
$k_4 = -2.169$ from (5)

And so $k = 5.484$ from (1) -- (a)

For $\frac{a}{r} = 4$ one obtains:

$k_1 = 5$ from (2)
$k_2 = -12.156$ from (3)
$k_3 = 14.705$ from (4)
$k_4 = -6.548$ from (5)

And so $k = 3.454$ from (1) -- (b)

The value in (a) is approximately 1.5 times the value in (b). As this equation is merely used to suggest a load at which a crack will initiate at the notch tip, this discrepancy is relatively unimportant. Inaccuracies will also have been introduced by the fact that these equations are derived for tensile loads, while the applied loads are compressive.

Appendix 2: Gurson's Model

(From : *ABAQUS Standard* Users Manual, 1996)

The Gurson yield condition for a material with a small volume fraction of voids is stated as follows:

$$\Phi = \left(\frac{q}{\sigma_y}\right)^2 + 2q_1 f \cosh\left(-\frac{3}{2}\frac{q_2\, p}{\sigma_y}\right) - (1 + q_3 f^2) = 0$$

Where:

$q = \sqrt{\frac{3}{2}(\boldsymbol{S} : \boldsymbol{S})}$ is the Mises stress

$\boldsymbol{S} = \boldsymbol{\sigma} + p\boldsymbol{I}$ is the deviatoric part of the Cauchy stress tensor, $\boldsymbol{\sigma}$. The Cauchy stress is defined as the force per unit area comprised of voids and material.

I is the unit matrix

: is the scalar product of two matrices

$p = \frac{1}{3}(\sigma : \boldsymbol{I})$ is the hydrostatic pressure

f is the volume fraction of the voids: $f=0$ implies that the material is fully dense and the Gurson yield condition is reduced to the Mises yield condition, $f=1$ implies that the material is fully voided and has no stress carrying capability.

σ_y is the yield stress of the fully dense material. It is a function of $\bar{\varepsilon}_m^{pl}$, the equivalent plastic strain in the matrix. So:

$$\sigma_y = \sigma_y\,(\bar{\varepsilon}_m^{pl})$$

q_1, q_2 and q_3 are parameters introduced by Tvergaard (Tvergaard,1981) with the following recommended values:

$q_1 = 1.25$

$q_2 = 1$

$q_3 = q_1$

$q_1 = q_2 = q_3 = 1$ gives the original Gurson equation.

The model gives reasonable results for material with less than 10% voids - ie for $f < 0.1$

The plastic strains are derived from the yield condition, with:

$$\dot{\varepsilon}^{pl} = \dot{\lambda}\,\frac{\partial \Phi}{\partial \sigma}$$

where λ is the non-negative plastic flow multiplier.

The change in void volume fraction is given as:

$$\dot{f} = \dot{f}_{gr} + \dot{f}_{nucl}$$

where

$\dot{f}_{gr}$ is the rate at which the void volume fraction changes due to void growth

and

$\dot{f}_{nucl}$ is the rate at which the void volume fraction changes due to void nucleation.

Growth of existing voids is based on the law of conservation of mass and is expressed as follows:

$$\dot{f}_{gr} = (1-f)\ \dot{\varepsilon}^{pl} : \boldsymbol{I}$$

where

$\dot{\varepsilon}^{pl}$ is the rate of plastic strain matrix and
f is the void volume fraction as before

The nucleation of voids is given by a strain-controlled relationship:

$$\dot{f}_{nucl} = A\ \bar{\varepsilon}^{m}_{pl}$$

where

$$A = \frac{f_N}{s_N\sqrt{2\pi}} \exp\ [\ \frac{1}{2}\ (\frac{\bar{\varepsilon}^{pl}_{m} - \varepsilon_N}{s_N})^2]$$

where

ε_N is the mean value of the normal distribution of the nucleation strain, typically 0.1 to 0.3
s_N is the standard deviation, usually 0.05 to 0.1 and
f_N is the volume fraction of nucleated voids, given as 0.04

$\frac{A}{f_N}$ is assumed to have a normal distribution.

6 References

ABAQUS Standard Users Manual; Publ : Hibbitt, Karlsson & Sorensen Inc; 1996

Almond E.A., Roebuck B.; *Fatigue-crack growth in WC-Co hardmetals*; Metals Technology; 1980; 7; 83-85

Aoki S., Moriya Y., Kishimoto K., Schmauder S.; *Finite Element Fracture Analysis of WC-Co Alloys*, Engineering Fracture Mechanics; 1996; 55; 275-287

BOART Longyear; Private Communication; 1996

Brookes, K. J. A.; *Hardmetals and other hard materials*; Publ : International Carbide Data; 3rd Ed; 1998

Christman T, Suresh S.; *Crack initiation under far-field cyclic compression and the study of short fatigue cracks*; Engineering Fracture Mechanics; 1986; 23; 953-964

Davies Y.J., Barhana S.; *Fatigue of a WC-25%Co Alloy*; Planseebericht Für Pulvermetallurgie; 1972; 20; 30-38

Evans A.G.; *Fatigue in ceramics*; International Journal of Fracture; 1980; 16; 485-498

Evans A.G., Linzer M.; *High frequency cyclic crack propagation in ceramic materials*; International Journal of Fracture; 1976; 12; 217-222

Ewalds H.L., Wanhill R.J.H.; *Fracture Mechanics*; 1989; Edward Arnold and Delftse Uiygevers Maatschappij; Delft, The Netherlands

Ewart L., Suresh S.; *Dynamic fatigue crack growth in polycrystalline alumina under cyclic compression*; Materials Science Letters; 1986; 5; 774-778

Ewart L., Suresh S.; *Crack propagation in ceramics under cyclic loads;* Materials Science; 1987; 22; 1173-1192

Fischmeister H. F., Schmauder S., Sigl L. S.; *Finite Element Modelling of Crack Propagation in WC-Co Hard Metals*; Materials Science and Engineering; 1988; A105/106; 305-311

Fry P.R., Garret G.G.; *Fatigue crack growth behavior of tungsten carbide-cobalt hardmetals*; Materials Science; 1988; 23; 2325-2338

Godse R., Gurland J., Suresh S.; *Effects of Residual Stresses in Fracture Toughness Testing of Hard Metals*; Materials Science and Engineering; 1988; A105/106; 383-387

Gurson A. L.; *Continuum Theory of Ductile Rupture by Void Nucleation and Growth : Part I - Yield Criteria and Flow Rules for Porous Ductile Media*; Journal of Engineering Materials and Technology; 1997; 99; 2-15

Hardrath H.F.; *Fracture Mechanics*; Journal of Aircraft; 1974; 11; 305-312

Hertzburg R.W.; *Deformation and Fracture Mechanics of Engineering Materials*; 1989; John Wiley & Sons; New York

Holm D. K., Blom A. F., Suresh S.; *Growth of cracks under far-field cyclic compressive loads: numerical and experimental results*; Engineering Fracture Mechanics; 1986; 23; 1097-1106

Hubbard R. P.; *Crack Growth Under Cyclic Compression*; Journal of Basic Engineering; 1969; December; 625-631

Human, A.M.; *Compression-Compression Precracking of WC-Co Toughness Specimens;* 4th Year Metallurgy Research Project University of the Witwatersrand; 1988

Iizuka H., Tanaka M.; *Fracture toughness measurement with fatigue-precracked single edge-notched beams specimens of WC-Co hard metal*; Materials Science; 1991; 26; 4394-4398

James M.N., Human A.M., Luyckx S.; *Fracture toughness testing of hardmetals using compression-compression precracking;* Journal of Materials Science; 1990; 25; 4810-4814

Johansson I., Persson G., Hiltscher R.; *Determination of Static and Fatigue Strength of Hard Metals*; Powder Metallurgy International; 1978; 2; 119-123

Jaensson, B. O., Sundström, B. O.; *Determination of Young'sModulus and Poisson's Ratio for WC-Co Alloys by the Finite Element Method*; Materials Science and Engineering; 1972; 9

Knee N., Plumbridge W.J.; *The influence of microstructure and stress ratio on fatigue crack growth in WC-Co hardmetals*; Advances in Fracture Research ICF6, New Delhi, India; 1984; Vol 4; 2685-2692

Kursawe S., Schulte R., Sockel H. G.; *Damage Mechanisms in Graded Hard Metals under Cyclic Loads*; Private communication; 1998

Lueth R.C.; *Fatigue Crack Growth in WC-Co Alloys;* Materials Technology; 1981; Spring; 27-30

Luyckx S. B.; *Some Results on High Cycle Fatigue of a WC-Co Alloy*; Electron Microscopy Society of Southern Africa; 1976; 6; 81-82

Poech M. H, Fischmeister H, Spiegler R.; *Assessment of the In Situ Properties of the Cobalt Phase in WC-Co Hard Metals*; Journal of Hard Materials; 1991; 2; 197-205

Polák J., Obrtlik K., Vrbka J.; *Cyclic plastic response and fatigue fracture of WC-9Co hardmetal*; Preprint 1990

Quinn D. F., Connolly P.J., O'Regan T. L., Howe M. A.,McHugh P. E.; *Simulation of Co Binder Failure in WC-Co Hardmetals*; IUTAM Symposium on Micromechanics of Plasticity and Damage of Multiphase Materials; 1996; 231-238

Reid C. N., Williams K., Hermann R.; *Fatigue in Compression*; Fatigue of Engineering Materials and Structures; 1979; 1; 267-270

Roarke R. J., Young W.C.; *Formulas for Stress and Strain*; 1975; McGraw-Hill; New York

Roebuck B., Almond E.A.; *Deformation and fracture processes and the physical metallurgy of WC-Co hardmetals*; International Materials Reviews; 1988; 33; 90-110

Schleinkofer U., Sockel H.G., Görting K., Heinrich W.; *Fatigue of Hard Metals and Cermets: New Results and a Better Understanding*; Preprint 1996

Schleinkofer U., Sockel H.G.., Görting K., Heinrich W.,; *Microstructural processes during subcritical crack growth in hard metals and cermets under cyclic loads*; Materials Science and Engineering; 1996; A209; 103-110

Schleinkofer U., Sockel H.G.., Görting K., Heinrich W.,; *Fatigue of hard metals and cermets*; Materials Science and Engineering; 1996; A209; 313-317

Schleinkofer U., Sockel H.G., Schlund P., Görting K., Heinrich W.; *Behavior of hard metals and cermets under cyclic mechanical loads*; Materials Science and Engineering; 1995; A194; 1-8

Schleinkofer U., Sockel H.G., Schlund P., Kindermann P., Schulte R., Werner J., Görting K., Heinrich W.; *Limited Fatigue Lives of Uncoated and Coated Hardmetals under Cyclic Loads*; Proceedings Euro PM'96; 1996; 239-246

Sigl L.S., Fischmeister H.F.; *On the fracture toughness of cemented carbides*; Acta Metallurgica; 1988; 36; 887-897

Sigl L. S., Schmauder S.; *A finite element study of crack growth in WC-Co*; International Journal of Fracture; 1988; 36; 305-317

Spiegler R., Fischmeister H. F.; *Prediction of Crack Paths in WC-Co Alloys*; Acta Metallurgica; 1992; 7; 1653-1661

Spiegler R., Schmauder S., Exner H. E., *Finite Element Modelling of the Thermal Residual Stress Distribution in a WC-10wt%Co Alloy*; Journal of Hard Materials; 1992; 3; 143-151

Sundström B. O.; *Elastic-Plastic Behaviour of WC-Co Analysed by Continuum Mechanics*; Materials Science and Technology; 1973; 12; 265-276

Suresh S.; *Crack Initiation in Cyclic Compression and its Applications*; Engineering Fracture Mechanics; 1985; 21; 354-463

Suresh S.; *The Failure of Hard Materials in Cyclic Compression: Theory, Experiments and Applications*; Materials Science and Engineering; 1988; A105/106; 323-329

Suresh S.; *Mechanics and Micromechanisms of Fatigue Crack Growth in Brittle Solids*; International Journal of Fracture; 1990; 42; 41-46

Suresh S.; *Fatigue Crack Growth in Brittle Materials*; Journal of Hard Materials; 1991; 2; 29-54

Suresh S.; *Fatigue of Materials*; 1992; Cambridge University Press; Cambridge, Great Britain

Suresh S., Brockenbrough J.R.; *Theory and experiments of fracture in cyclic compression: single phase ceramics, transforming ceramics and ceramic composites*; Acta Metallurgica; 1988; 36; 1455-1470

Suresh S., Ewart L., Maden M., Slaughter W.S., Nguyen M.; *Fracture toughness measurements in ceramics: pre-cracking in cyclic compression*; Materials Science; 1987; 22; 1271-1276

Suresh S., Sylva L.A.; *Room temperature fatigue crack growth in cemented carbides*; Materials Science and Engineering; 1986; 83; L7-L10

The Welding Institute; *Tests for Fracture Toughness and Fatigue Assessment : a compilation of stress intensity, compliance and elastic η factors*

Tvergaard, V.; *Influence of voids on shear band instablilities under plain strain conditions*; International Journal of Frature Mechanics; 1981; 17; 389-407

Tvergaard, V., Needleman A,; *Analysis of the Cup-Cone Fracture in a Round Tensile Bar*; Acta Metallica; 1984; 32; 157-169

Author: Erling, Ghita.
Name of thesis: On the initiation and propagation of fatigue cracks in WC-Co.

PUBLISHER:

University of the Witwatersrand, Johannesburg